UNIVERSITÀ
degli STUDI
di CATANIA

Dipartimento
di Fisica
e Astronomia
"Ettore Majorana"

PhD programme in physics

Alessandro Alberto Oliva

Nucleosynthesis in massive stars through the Trojan Horse Method

PhD thesis

Supervisors:
Prof. L. Lamia
Dr. M. La Cognata

---

academic year 2022/2023

To the two loves of my life:
Martina and Science

Contents

Chapter 1

Nucleosynthesis in massive stars: an introduction

All the theories regarding the nucleosynthesis of the elements in the universe have to correctly reproduce one unquestionable experimental evidence: the abundance of these elements in the universe itself that astrophysicist can reliably measure. By looking at Fig. 1.1 where the abundances of the elements in the universe, relative to that of the silicon, are plotted as a function of the mass number A, one can immediately notice several peaks. Leaving aside those of hydrogen (H) and helium (He), which are deeply linked to the primordial nucleosynthesis, it's possible to note a greater abundance of elements with a mass lower than that of iron (Fe). Moreover, also in correspondence of the iron (A = 52), a pronounced peak is obtained, after which the abundance is reduced with two different slopes between iron and xenon (Xe) and between xenon and lead (Pb).

The reason for these different abundances can be explained by observing the binding energy per nucleon as a function of the mass number, plotted in Fig. 1.2. In the proximity of iron the absolute maximum of the binding energy per nucleon is obtained: this means that all nuclear reactions that produce elements lighter than iron can take place in an ex-

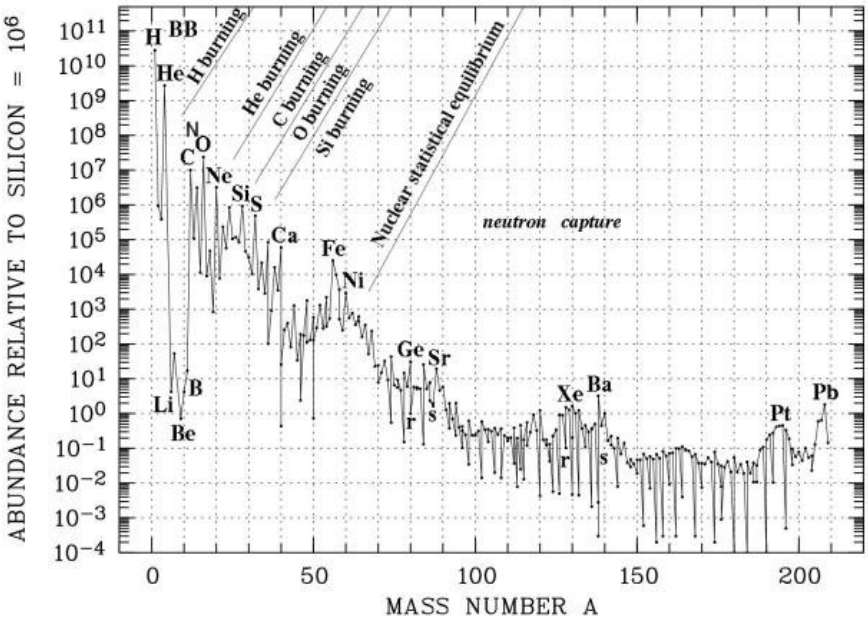

Figure 1.1: Graphical representation of the abundances, relative to those of silicon, of the elements estimated for the whole universe, as a function of the mass number A. [1]

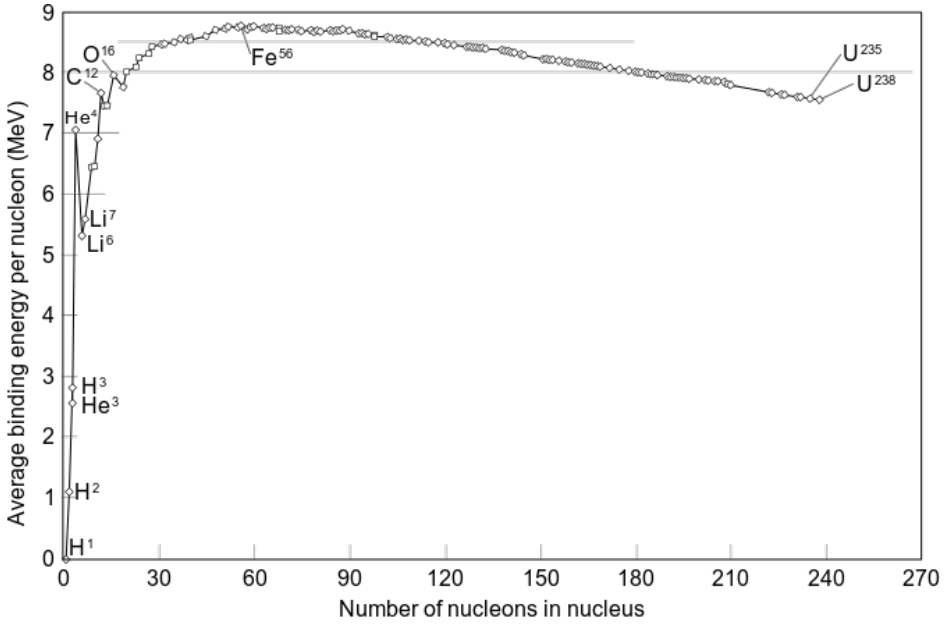

Figure 1.2: Graphical representation of the average binding energy per nucleon as a function of the mass number A.

oenergetic regime, i.e. with a positive Q-value of reaction. These elements are substantially produced [2] by thermonuclear fusion processes, i.e. radiative captures of either protons or alpha particles at energies lower than the Coulomb barrier. While all of these processes are quite similar, it is possible to discern various stages, also in relation to the evolution of the stars involved, for the various nuclei used as a fuel for the reactions.

In contrast, producing elements heavier than iron using the same thermonuclear fusion processes would mean that the reactions should now proceed through an endoenergetic regime with a negative Q-value. Moreover it should be considered that increasing the atomic number of the elements involved in the radiative capture process means also increasing the value of the Coulomb barrier between it and the other charged particle involved. It is clear that, at moderate stellar temperatures, it is very unlikely to find a particle with such energy to overcome the Coulomb

barrier, considering also the energy loss due to the negative Q-value of the reaction itself. Meanwhile at very high temperatures, charged-particle reactions at such energies will result in nuclides of the iron peak group or lighter species[3].

If reactions induced by charged particles are so heavily suppressed by the Coulomb barrier, those induced by neutrons can therefore thrive instead, since they are not affected by the Coulomb potential. Indeed, by looking at Fig. 1.1, one can easily notice that after the iron peak all the other peaks corresponds to those elements for which the neutron nuclear shell is closed. Therefore it is possible to divide the nucleosynthesis process in two macro-categories: thermonuclear reactions induced by charged particles and neutron induced reactions.

Moreover, as suggested by the title of the chapter, the astrophysical site of interest for this work of thesis are massive stars, i.e. stars with an initial mass greater than about eight times the mass of the sun ($M >\sim 8M_{\odot}$). They are key drivers for the stellar nucleosynthesis since they are the site where most of the heavy nuclei in the universe are produced. They are however also much rarer than low and intermediate mass stars and only in recent years the statistics of observations is starting to become significant enough to have precise experimental data on their structure and emission, thanks also to the so-called multi-messenger astronomy. Describing their evolution and the stellar models used to study them is beyond the scope of this thesis. In this first chapter we will instead introduce and discuss the two main families of nucleosynthesis reactions, focusing then in particular on those reactions relevant for this work.

1.1 Thermonuclear reactions

In the stellar environment the energy available to the nuclei is solely that of their thermal motion: for this reason the reactions occurring in this environment are indeed called thermonuclear reactions. It should

not come as surprise that, in most cases, the nuclear matter in stars is non-relativistic and non-degenerate. This means that the velocities of the nuclei can be simply described by a Maxwell–Boltzmann distribution[3]. Usually when talking about thermonuclear reactions, physicist refers to reaction networks rather than a single reaction process. This is due to the fact that many nuclear processes can take place simultaneously in the stellar plasma: nuclei created by some fusion reactions can be subsequently destroyed by other reactions occurring in the same environment and so on. In these reaction networks, for a given temperature and abundance of elements in the plasma, those with the lowest Coulomb barrier will ignite first. Indeed nuclear reactions involving hydrogen and helium are the main energy sources for most of the stars in the universe [3]. Then, when these light nuclei have been consumed, the nuclear energy production will decrease until it can not balance the gravitational push and subsequently the star will contract. The temperature will in turn increase until the next nuclei with the lowest Coulomb barrier can be "consumed", producing once again the necessary nuclear energy to balance the gravitational collapse. Depending on its initial mass, a star can experience only a few or several of these so-called "nuclear burning stages". In particular massive stars, depending on their mass [3], can undergo most of the stages referred to as *hydrogen burning*, *helium burning*, *carbon burning*, *neon burning*, *oxygen burning* and *silicon burning*. In this work we will focus mainly on carbon and oxygen burning.

1.1.1 Carbon burning

After hydrogen and helium are consumed in the core of the star, the elements with the highest abundance are now ^{12}C and ^{16}O, produced by the famous *3α* process and by the $^{12}C(\alpha,\gamma)^{16}O$ radiative capture. These two elements can then interact via three different process: $^{12}C + ^{12}C$, $^{12}C + ^{16}O$ and $^{16}O + ^{16}O$. However, when a new gravitational collapse increases the core temperature the first Coulomb barrier that can be overcome is the

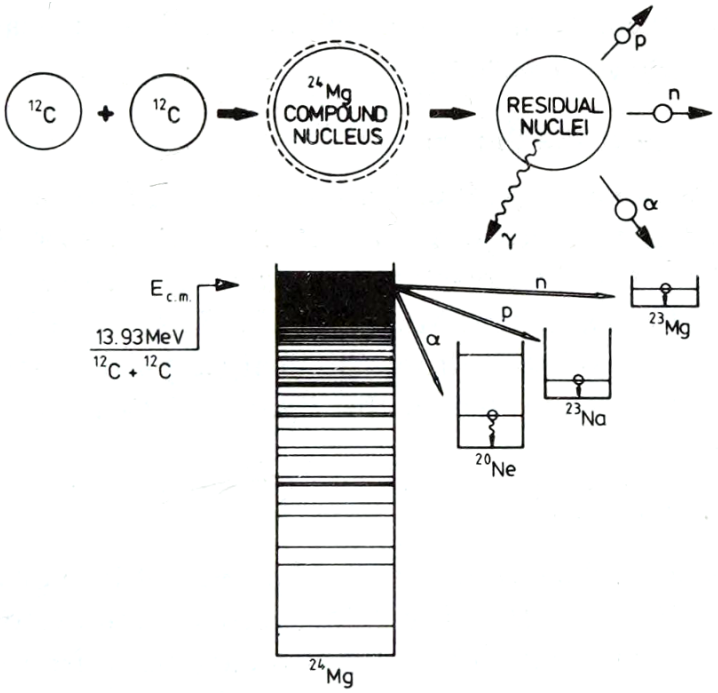

Figure 1.3: Graphical representation of the ^{12}C $+^{12}$ C fusion process (top) and the energy level scheme of the intermediate ^{24}Mg system. [1]

one between two ^{12}C nuclei ($V_C \approx 8MeV$) and therefore the ^{12}C $+^{12}$ C fusion process ignites.

This fusion produces a ^{24}Mg intermediate system with a significantly high excitation energy of about 14 MeV: at such energy the density of nuclear states is quite high and the particle decay channels are favorite over the emission of a photon, as it usually happens for radiative captures by light nuclei. A sketch of the process can be seen in Fig. 1.3. The three primary reactions involved in the process are:

- ^{12}C(^{12}C, p)^{23}Na (Q = 2.24 MeV);
- ^{12}C(^{12}C, α)^{20}Ne (Q = 4.67 MeV);
- ^{12}C(^{12}C, n)^{23}Mg (Q = -2.6 MeV).

The light particles liberated as byproduct of the reactions are then captured again, with a certain probability, by secondary reactions in the C-burning stage that involve the nuclei present in the environment. On this regard in Fig. 1.4 it is possible to see the evolution over time of the abundances of the elements during the core C-burning. The typical temperatures reached in this case are $T = 0.6 \div 1$ GK. Without going too into the details of the reactions network, it is possible to see that while the ^{12}C depletes almost completely after 10^5 s, the ^{16}O only slightly decreases indicating a partial involvement in the network. Meanwhile, all the heavy products of the primary reactions increase to significant values of mass fractions: ^{20}Ne (X=0.35), ^{23}Na (X=0.014) and ^{24}Mg (X=0.025). The abundance of ^{20}Ne nuclei is such that the subsequent burning phase is not the O-burning, as one would assume looking at the nuclei mass, but the Ne-burning ignited by the photodissociation of ^{20}Ne occurring at $T > 1$ GK after a new contractions takes place at the end of C-burning. While most of the nuclear species in the environment have a quite high ($E_s = 10 \div 20$ MeV) particle separation energy, the α separation energy of ^{20}Ne is only about 4.73 MeV [3].

1.1.2 Oxygen burning

After the neon burning comes to an end, the stellar core, which is now composed mainly of ^{16}O, ^{24}Mg and ^{28}Si, undergoes a new contraction and reaches temperatures of about 2 GK at which the energy is high enough to finally overcome the Coulomb barrier between two ^{16}O nuclei. In a way this stage resembles the carbon burning since again the main process sustaining the nucleosynthesis is a fusion of two medium mass nuclei that produce an heavy intermediate system, a ^{32}S nuclei in this case, with an high excitation energy (about 16.5 MeV) that corresponds to a region with an high density of excited states. The main decay channels are once again those involving the emission of a proton, a neutron, a deuteron or an α such as

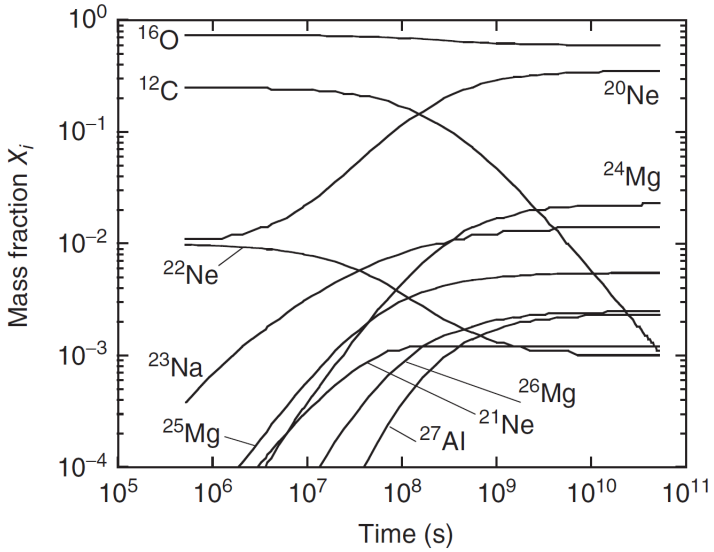

Figure 1.4: Evolution of the abundances for a constant temperature and density (T = 0.9 GK, ρ= 105 g/cm^3) typical of core C-burning in stars with an initial mass of $M \approx 25 M_\odot$. [3]

- $^{16}O(^{16}O, p)^{31}P$ (Q = 7.67 MeV);
- $^{16}O(^{16}O, n)^{31}S$ (Q = 1.5 MeV);
- $^{16}O(^{16}O, d)^{30}P$ (Q = -2.4 MeV);
- $^{16}O(^{16}O, \alpha)^{28}Si$ (Q = 9.6 MeV);

even though two particle emission decay are also possible, such as

- $^{16}O(^{16}O, 2p)^{30}S$ (Q = 381 keV);
- $^{16}O(^{16}O, 2\alpha)^{24}Mg$ (Q = -390 MeV).

In this case however, in contrast to the carbon burning, the number of open exit channels is quite higher since the ^{32}S compound nucleus achieves much higher excitation energies. Moreover, the branching ratio between the different O-burning channels is still mostly unknown and their rates are know only up to a factor of 3. Also in this case, the light particles emitted by the primary reactions are quickly captured by secondary reactions of the network, involving again the heavy nuclei produced by the primary reactions as well as the ashes of neon burning. The temperatures reached during core oxygen burning have typically a value of $T = 1.5 \div 2.7$ GK, depending on the mass of the star[3].

1.1.3 $^{12}C + ^{16}O$ fusion

Now that we have briefly introduced the carbon and oxygen burning stages, we can turn our attention on the third fusion process that could take place from the ashes of helium burning: the $^{12}C + ^{16}O$ fusion. As it can be seen in Fig. 1.5, during the last part of the He-burning, when the fuel is almost all depleted, the abundance of carbon reaches a maximum and then suddenly decreases while the abundance of oxygen rises instead. This is due to the onset of the $^{12}C(\alpha, \gamma)^{16}O$ radiative capture

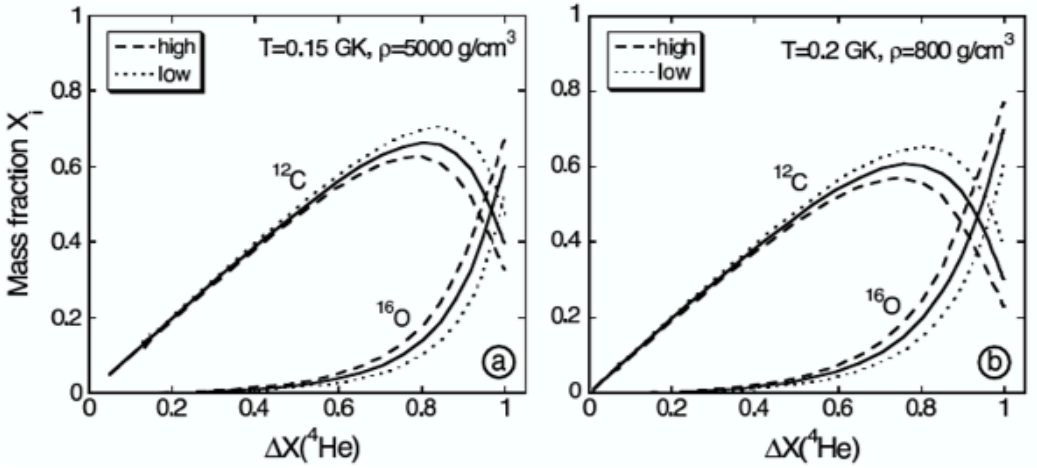

Figure 1.5: Abundance of ^{12}C and ^{16}O nuclei as a function of the residual mass fraction of ^{4}He nuclei for different values of temperature and density. [3]

that consumes the remaining of helium fuel and part of the carbon. This process however does not end with the He-burning in the core: we know indeed that even if the core is burning an heavier fuel there can be shells around the core where lighter nuclei are still consumed. This means that when the carbon burning actually ignites in the core the relative abundance of ^{12}C/^{16}O in the environment can vary in a significant way, thus altering the future development of the star.

In Fig. 1.6 it is possible to see the reaction rates for the main reactions involved in the $^{12}\mathrm{C} + ^{12}\mathrm{C}$, $^{12}\mathrm{C} + ^{16}\mathrm{O}$ and $^{16}\mathrm{O} + ^{16}\mathrm{O}$ processes normalized to the $^{12}\mathrm{C}(^{12}\mathrm{C}, \alpha)^{20}\mathrm{Ne}$ reaction rate.

While the reaction rates for the $^{12}\mathrm{C} + ^{16}\mathrm{O}$ fusion are lower than the ones for the $^{12}\mathrm{C} + ^{12}\mathrm{C}$ at any temperature up to 10 GK and indeed the latter is the main process during carbon burning, in the later phases of this stage the abundance of oxygen is significantly higher [3] than that of ^{12}C nuclei. In particular, as visible in Fig. 1.6, at temperatures higher than 1 GK the contribution of the $^{12}\mathrm{C} + ^{16}\mathrm{O}$ fusion becomes significant.

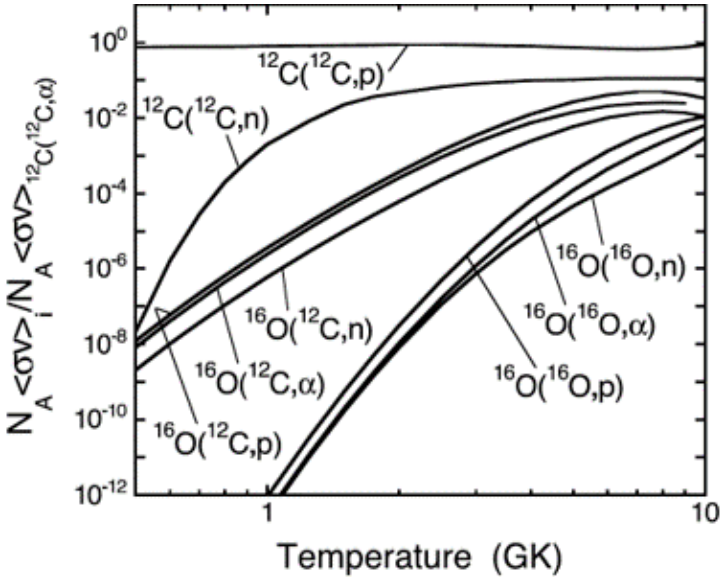

Figure 1.6: Reaction rates for various $^{12}C + ^{12}C$, $^{12}C + ^{16}O$ and $^{16}O + ^{16}O$ reaction channels [3].

Similarly, the $^{12}C + ^{16}O$ fusion can be ignited also in the subsequent oxygen burning stage. Indeed, as visible in Fig. 1.7 above a certain temperature and density, the ^{16}O photo dissociation becomes the main burning process in this stage and thus frees again ^{12}C nuclei in the stellar environment which can then interact with the oxygen present. Going back to Fig. 1.6 it is then possible to notice that the various reactions involved in the $^{12}C + ^{16}O$ fusion have actually an higher rate that any reaction of the $^{16}O + ^{16}O$ fusion. This means that as soon as a significant quantity of carbon nuclei is available during the O-burning the $^{12}C + ^{16}O$ becomes prevalent.

In summary, the $^{12}C + ^{16}O$ fusion is supposed to come into play in a significant way in a range of temperatures that span between 1 GK, in the case of hydrostatic core carbon burning, 3 GK, during the oxygen burning, and 3.6 GK for explosive burning phases. This corresponds to an energy range, in the center of mass of the system, between respectively

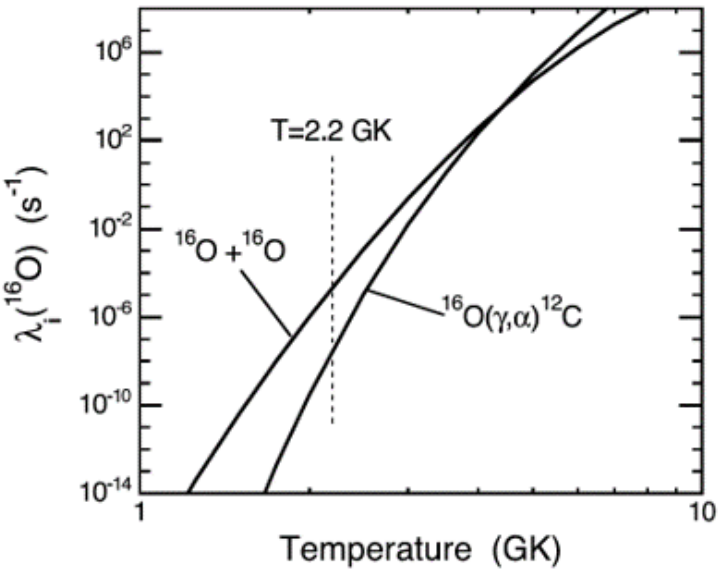

Figure 1.7: Decay constants for the $^{16}O + ^{16}O$ fusion and $^{16}O(\gamma,\alpha)^{12}C$ photo-disintegration as a function of the temperature.

3 and 7.2 MeV.

1.2 Neutron induced reaction

Neutrons, unlike protons, are unstable if not bound to a nucleus and they transform into protons by β^- decay ($n \rightarrow p^+ + e^- + \nu_e$) in the vacuum with a average lifetime of $881.5 \pm 1.5s$. Therefore the neutron abundance in the interstellar medium can not be significant: the presence of an active source of neutrons inside the star is then required. Moreover, while we already said that there are not barrier effects that can hinder neutron captures by the nuclei, there are still a series of mechanism in place that prevent an indefinite number of neutrons to be added into a nucleus: if the nucleus formed by the reaction has a particularly asymmetric density of the nucleons, it could then become unstable and decay.

Neutron induced reactions are then regulated by two time scales: the

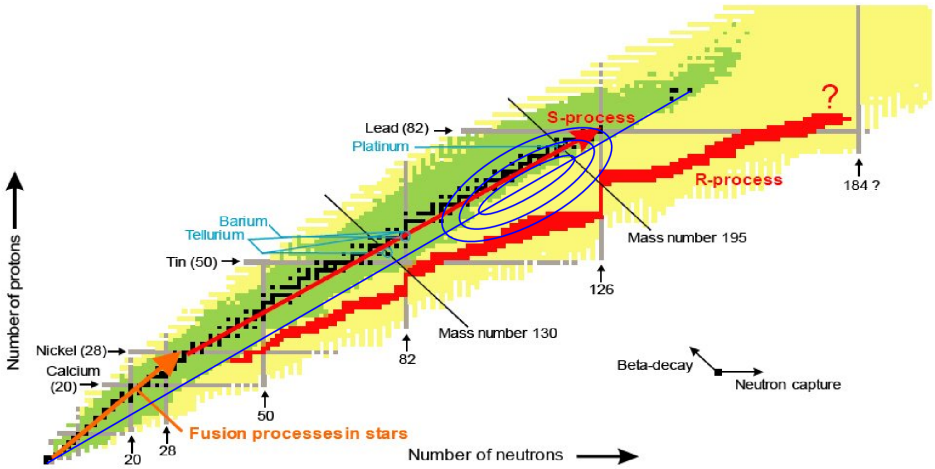

Figure 1.8: Table of nuclides and the paths followed by the s- and the r-process The vertical and horizontal lines corresponds to the closures for the protons and neutrons shell [4].

mean β decay time of the nuclei involved in the reactions and the mean time for the neutron capture to occur. If, on average, the β decay time is smaller than the neutron capture time, the nucleus will have enough time between two subsequent captures to actually decay if it is β unstable. Then the reaction chain will proceed mainly through the nuclear valley of stability. On the contrary, if the β decay time is greater than the neutron capture time, the capture process will happen so rapidly that the nucleus would not have enough time to decay, increasing the asymmetry between nucleons and moving away from the nuclear valley of stability. The first case takes the name of "s-process" due to being the slower than the two, meanwhile the other is called "r-process" being the most rapid. In figure 1.8 it is possible to see a graphic representation of the paths followed by the two processes within the chart of nuclides. In this thesis, only the slow capture process will be investigated.

1.2.1 s-process

As already said, the s-process is substantially characterized by a series of neutron capture reactions involving heavy nuclei close to the valley of stability. We can then imagine of taking a small portion of the nuclei chart and tracing the theoretical path followed by the reactions. In general we can imagine, as visible in Fig. 1.9(a), that a nucleus of mass A is produced by the neutron capture exerted by the nucleus of mass A-1. The same nucleus of mass A is then "destroyed" when it captures again a neutron, thus producing a new nucleus of mass A+1. If we now actually reproduce the proper trace in the chart of nuclides and also introduce the possibility that the nucleus produced is unstable due to β decay, Fig. 1.9(b), the nucleus A-1 now can produce a nucleus, indicated in figure by the white square, with mass number A but β unstable. Under the s-process time scale condition the β decay time is much faster than the time between one capture and the next, therefore the produced nucleus can decay into a new nucleus with the same mass number A but an atomic number Z higher than one unit, therefore converting one neutron into a proton. This means that the process now moves diagonally along the nuclei chart, as indicated by the diagonal arrow in Fig. 1.9(b). This new nucleus can either be still β unstable and undergo a new decay in a similar fashion or, as visible in figure, capture a new neutron, finally creating the nucleus of mass A+1.

The s-process therefore consists of a series of these chains that uses the nuclei already synthesized in the star by the previous reactions as *seed* nuclei for the production of heavier elements up to ^{209}Bi where the process comes to an end. This is in fact the heaviest stable nucleus and further neutron capture would lead to the production of highly unstable nuclei that will undergo α decays.

Without going much into the details of the nuclear formalism, which will be examined in the next chapter of this thesis, it is possible to say that there are two different components in the s-process, the *main* and

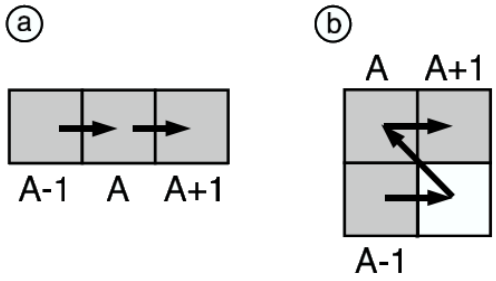

Figure 1.9: Path of the s-process among the charts of nuclides if we exclude the possibility of β decay (a) or if we include it instead (b) [3].

weak component, that can be distinguished for a series of factors. Actually, some authors have shown [5] that these two components do not fully reproduce the abundances of all the elements involved in the s-process, which has led to consider new components different from the two mentioned, however the debate is still open. What it has been assessed is that the main component is responsible for the production of nuclei of mass $A \gtrsim 90$, while the weak component produces the nuclei of mass $A \lesssim 90$ down to the iron peak around $A \sim 60$.

The two components also manifest in stellar sites that are particularly different from each other and in different moments of the evolution of the star: while the main component occurs in carbon pockets in the envelope during the AGB phase, the weak component occurs instead during the core He-burning and shell C-burning of massive stars. Since the latter are, as already pointed out, the astrophysical environment of interest for this thesis, we will now focus only on the weak component.

1.2.2 The $^{17}O(n,\alpha)^{14}C$ as a weak component s-process poison

The weak component of the s process manifests itself [6] when its main neutron source $^{22}Ne(\alpha,n)^{25}Mg$ ignites, producing the necessary neutron

flux. This source reaction occurs in massive stars both in the core, during the He-burning, and in the convective shells, during the C-burning if the neutron density is high enough to have an exposure comparable to that in the core. As mentioned in the previous section, He-burning in the core ignites when all the hydrogen has been already consumed and the gravitational collapse brings the temperature to about $T_c \sim 0.16$ GK[7] that allows the helium fusion through the famous 3α process [2]. Furthermore, at these temperatures in a massive star the CNO cycle is also active which involves, among other things, the presence of nitrogen. The latter can trigger the chain of reactions $^{14}N(\alpha,\gamma)^{18}F(\beta^+)^{18}O(\alpha,\gamma)^{22}Ne$ which produces the ^{22}Ne that can then interact with the helium nuclei in the stellar environment to ignite the needed neutron source $^{22}Ne(\alpha,n)^{25}Mg$. However not all the ^{22}Ne is consumed in the core and it can then diffuse to the stellar envelope which in turn allow a second ignition of the neutron source later in the stellar evolution, in the aforementioned C-burning shells where the $^{12}C(^{12}C,\alpha)^{20}Ne$ reaction provides the needed α particles at temperatures of about $T \sim 1.1$ GK [7]. Although the neutron source reaction is the same, the environmental conditions of these two different sites are remarkably different. This is reflected in the flux of neutrons produced: in the case of the core He-burning the source produces neutrons for about a thousand years but with a low exposure efficiency, on the contrary, for the shell C-burning, the efficiency is higher but the neutron source is active for a significantly smaller time frame.

In order to correctly determine the rate of all reactions taking part in the s-process, it is not enough to precisely define the neutron sources in the environment. Indeed there are reactions, called "neutron poisons", that can remove one or more neutrons for the environment without taking part in the s-process reaction network. Among the most important[7] neutron poisons of the weak component there is the $^{16}O(n,\gamma)^{17}O$ capture reaction. The produced ^{17}O can then undergo different process in competition with each other: $^{17}O(\alpha,n)^{20}Ne$, $^{17}O(p,\alpha)^{14}N$ and $^{17}O(n,\alpha)^{14}C$.

The first one recycle a neutron back in the stellar environment, having a null net neutron footprint, meanwhile the last one actually removes a second neutron from the environment and it is indeed another subsequent poison that can occur after the main one. To correctly define the abundance of neutrons present in the stellar environment, it is therefore necessary to evaluate the rates of each of these possible reaction channels and their branching ratio. In this thesis the $^{17}O(n,\alpha)^{14}C$ reaction will be studied at energies of astrophysical interest corresponding to the typical temperatures where the poison can occur ($T \sim 0.016 \div 1.1$ GK)[7, 8].

Chapter 2

Nuclear Physics for Astrophysics

Before discussing the theoretical and experimental methodologies used for the study of the reactions of interest for the astrophysics in the laboratory, it is necessary to provide some background on nuclear reactions, by defining the fundamental characteristic of the phenomena involved.

2.1 Reaction Cross-Section

In the case a reaction between a beam of particles accelerated on a target is considered, it is possible to give a practical definition [3] of the cross-section as as the ratio between the number of interactions actually occurred in the unit of time (N_R/t) and the product between the number of incident particles (N_{beam}) per unit area and time (tS) and the number of particles in the target (N_{target})

$$\sigma = \frac{N_R/t}{[N_b/\,(tS)]\,N_t} = \frac{N_R/t}{J_b N_t} \tag{2.1}$$

where J_b is the flux of the beam. However, it is often more useful to express the differential cross section which is the derivative of the cross section for the solid angle Ω. In fact, when carrying out an experiment it is not always possible to cover the whole solid angle around the spatial

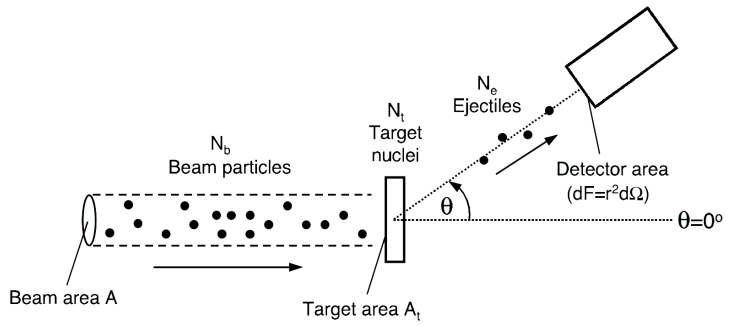

Figure 2.1: Schematic representation of a generic experimental setup with indicated the quantities related to the cross section.

region in which the reaction takes place, therefore the measurement that would be obtained from an instrument placed at a certain angle Ω and covering a certain interval $\Delta\Omega$ would only be valid locally: therefore, it must be integrated over the entire 4π range to obtain the complete information about the physical phenomena studied. Thus, we would have:

$$\sigma = \int d\Omega \left[\frac{d\sigma(\Omega)}{d\Omega} \right] \tag{2.2}$$

where $\frac{d\sigma(\Omega)}{d\Omega}$ is the differential cross-section defined as:

$$\frac{d\sigma(\Omega)}{d\Omega} = \frac{N_R/t}{\Delta\Omega J_b N_t} \tag{2.3}$$

2.2 Barrier effects

The empirical formula given for the cross-section is useful to understand the physical meaning of this observable, however when dealing with nuclear reactions, one must take into account all the relevant phenomena taking place. One important aspect to address here is the presence of two potential barriers which hinder the probability of the interaction to occur.

2.2.1 Centrifugal barrier

The centrifugal barrier is a repulsive effect that emerges from quantum mechanics when addressing the problem of three-dimensional scattering between a particle and a spherically symmetrical potential. In fact, by separating the radial part of the Schrödinger equation from the angular one, which can be easily solved thanks to the formalism of spherical harmonics, it is possible to reduce the problem from three dimensions to only one, concentrated exclusively on the radial part. In the presence of a system with spherical symmetry it is in fact possible to factor the wave function (w.f.) as follows:

$$\psi_{k,\ell,m}(r,\theta,\phi) = R_\ell(r)Y_{\ell,m}(\theta,\phi) \tag{2.4}$$

where $R_{n,\ell}(r)$ is the radial w.f. and $Y_{\ell,m}(\theta,\phi)$ are the spherical harmonics, whose explicit expressions, as a function of the quantum numbers ℓ, m are known and tabulated. The Hamiltonian operator of the system is given by the sum of the Hamiltonian of a free particle $\mathbf{P}^2/2\mu$ and the potential $V(r)$ exclusively dependent on the radius module, as mentioned above. As it is known, however, the impulse operator can be written as [9] in the representation of spherical coordinates

$$\frac{\mathbf{P}^2}{2\mu} = -\frac{\hbar^2}{2\mu}\left[\frac{1}{r^2}\frac{\partial}{\partial r}\left(r^2\frac{\partial}{\partial r}\right) - \frac{\mathbf{L}^2}{\hbar^2 r^2}\right] \tag{2.5}$$

where μ is the mass of the scattered particle and $\mathbf{L}$ is the angular momentum operator that is obtained by the means of the following identity:

$$\mathbf{L}^2 = -\frac{\hbar^2}{\sin^2\theta}\left[\frac{\partial}{\partial\theta}\left(\sin\theta\frac{\partial}{\partial\theta}\right) + \frac{\partial^2}{\partial\varphi^2}\right] \tag{2.6}$$

Replacing the equations 2.4 and 2.5 in the generic Schrödinger equation for the eigenvalues and remembering that, from the definition of spherical harmonics, it follows that

$$\mathbf{L}^2 Y_{\ell,m}(\theta,\phi) = \hbar^2\ell\left(\ell+1\right)Y_{\ell,m}(\theta,\phi) \tag{2.7}$$

we can finally obtain:

$$-\frac{\hbar^2}{2\mu}\frac{d^2}{dr^2}u_l(k,r)+\left[V(r)+\frac{\hbar^2\ell\left(\ell+1\right)}{2\mu r^2}\right]u_l(k,r)=Eu_l(k,r) \tag{2.8}$$

where $u_l(k,r) = krR_l(r)$ is the so-called reduced radial wave function. The equation 2.8 thus expresses, as anticipated, a problem with only one dimension and the solution is quite simple. In fact, it can be rewritten as the *Bessel* or *Ricatti-Bessel* equation, in the case in which the potential is zero. If we ignore electrical charge for the moment, the potential $V(r)$ will be the only attractive nuclear potential while the second term in square brackets, positive by definition and therefore repulsive, is precisely the centrifugal potential mentioned above. :

$$V_l^{centr}(r)=\frac{\hbar^2\ell\left(\ell+1\right)}{2\mu r^2} \tag{2.9}$$

The penetrability of this repulsive barrier must therefore be evaluated, as a function of the angular momentum of the neutron, by means of the penetration factor P_ℓ which is determined starting from the logarithmic derivative [3] calculated at a radius r equal to the range of the potential R, that is to the radius of the target nucleus.

$$R\left(\frac{1}{u_\ell(r)}\frac{du_\ell(r)}{dr}\right)_{r=R}=S_\ell+iP_\ell \tag{2.10}$$

where S_ℓ is the shift factor, responsible for the displacement of the energies observed in case of resonances, and P_ℓ is the factor we were searching for. Writing explicitly the logarithmic derivative we obtain the expression for this factor

$$P_\ell=R\left(\frac{k}{\widehat{j}_\ell^2(kR)+\widehat{\eta}_\ell^2(kR)}\right) \tag{2.11}$$

where $\widehat{j}_\ell$ and $\widehat{\eta}_\ell$ are the solutions to the first and second kind *Ricatti-Bessel* equation. These two functions are defined starting from the spherical

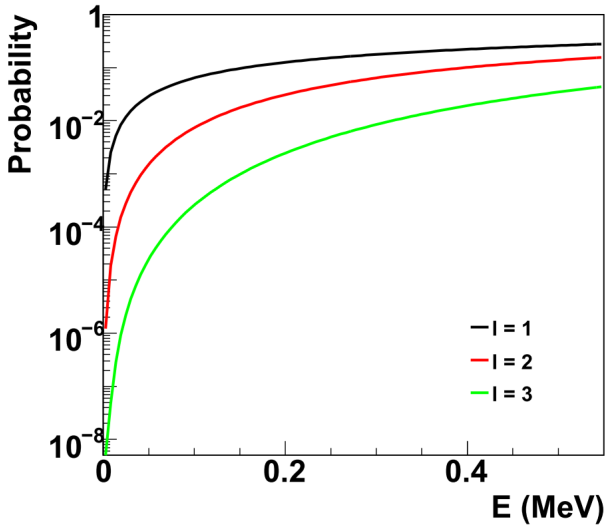

Figure 2.2: Probability of penetration of the centrifugal barrier for the reaction $^{17}O + n$ at energies of astrophysical interest for different values of the quantum number ℓ

Bessel functions, solutions of the spherically symmetrical Bessel equation, as follows:

$$\widehat{j_\ell} = (kr)j_\ell(kr) \qquad\qquad \widehat{\eta}_\ell(kr) = (kr)\eta_\ell(kr) \tag{2.12}$$

Since these functions are known and tabulated, it is possible to evaluate the value of P_ℓ as a function of the energy as the angular momentum ℓ varies, as shown in figure 2.2,

As can be easily observed, the centrifugal barrier has a significant influence only at low energies, of the order of hundreds of keV, precisely in the range of astrophysical interest and, at such energies, it is noted that the influence is already effective for angular moments greater than unity. This means that, in the calculation of the cross section, the probability of penetration must be included as a multiplying factor.

2.2.2 Coulomb barrier

If the two interacting nuclei, or particles, both possess an electrical charge then also the Coulomb barrier must be taken into account. We talk of a barrier, like the centrifugal one, since nuclei only posses a positive charge and therefore they can only repel each other. The negative charge of electrons has an effect that will be explained later. The Coulomb potential between two point-like charges is defined as the ratio between the product of the charges of the interacting nuclei Z_i and their distance r

$$V_{coul}(r) = \frac{Z_1 Z_2 e^2}{r} \tag{2.13}$$

In this case the potential $V(r)$ visible in Eq. 2.8 would be given by the sum between the nuclear potential, attractive and usually factored as a *Wood-Saxon* potential, and $V_{coul}(r)$. However, as it can be seen in Fig. 2.3, for distances larger than the sum of the two nuclear radius, i.e. outside the nucleus, the Coulomb potential prevails.

At low energies the general solution of the radial Schrödinger equation 2.8 is given by

$$u_\ell(r) = AF_\ell(r) + BG_\ell(r) \tag{2.14}$$

where $F_\ell(r)$ and $G_\ell(r)$ are the two independent solution of 2.8 in the presence of the coulomb potential and they are called, respectively, the regular and the irregular Coulomb wave functions for the angular momentum ℓ . The barrier penetrability can be evaluated as the ratio

$$P_\ell = \frac{|u_\ell(\infty)|^2}{|u_\ell(R)|^2} = \frac{1}{AF_\ell(R) + BG_\ell(R)} \tag{2.15}$$

where $u_\ell(\infty)$ is the asymptotic wave function, meanwhile $u_\ell(R)$ is the radial w.f. evaluated at the classical turning point of the barrier. For low energies the interaction between two point-like particles can be approximated in s-wave, neglecting all contribution with $\ell > 0$:

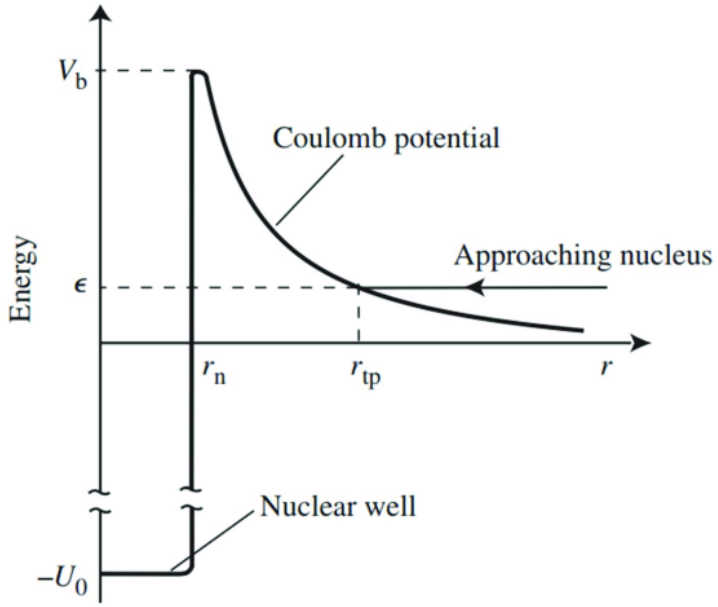

Figure 2.3: Graphical representation of the nuclear and Coulomb potential between to interacting nuclei as a function of the distance r between the pair.

$$P_0 \sim \exp(-2\pi\eta) \tag{2.16}$$

The penetrability P_0 takes the name of Gamow factor, where η is the Sommerfeld parameter and is equal to:

$$\eta = \frac{Z_1 Z_2 e^2}{\hbar v} \tag{2.17}$$

The Sommerfeld parameter is a measure of the Coulomb interaction intensity since it is directly proportional to the product of the charges of the interacting ions and to the inverse of the kinetic energy, i.e. it decreases when the kinetic energy increases, as the interaction time decreases. Remembering the results from the centrifugal barrier section, it should be clear that under the s-wave approximation we had to make the

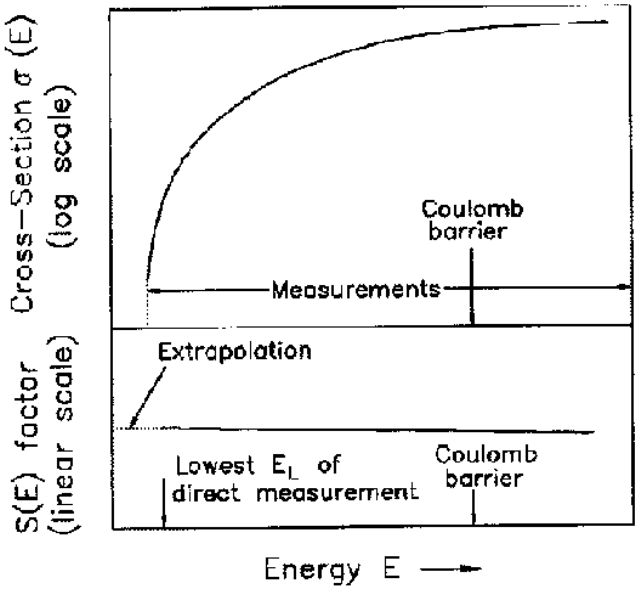

Figure 2.4: Graphic comparison between a generic direct capture cross section as a function of energy (top) and the corresponding astrophysical factor (bottom).

centrifugal barrier vanishes, therefore Eq. 2.16 represents the total barrier penetrability factor.

2.2.3 Astrophysical Factor

As it can be seen in 2.4, the presence of the Coulomb barrier causes a sudden drop of several order of magnitude in the cross-section at low energies. Therefore, as it will be explained better in Chapter 3 of this thesis, to work with a smoothly varying function, the astrophysical S-factor was introduced. It is defined as:

$$S(E) = \sigma(E)Ee^{2\pi\eta} \tag{2.18}$$

but, inverting this relation and writing it as

$$\sigma(E) = \frac{1}{E} e^{-2\pi\eta} S(E) \tag{2.19}$$

it is immediately clear that the S-factor is essentially the cross-section compensated for the gross contribution due to the Coulomb penetration. While the Gamow factor is only the s-wave approximation of such effects, it is the one with the most significant energy dependence, therefore its removal is important even if the reaction would proceed via partial waves with $\ell > 0$.

2.3 Reaction rate

In nuclear astrophysics we are interested in not only the cross-section of the process but also in the so called reaction rate of the process which is defined as the number of occurring reactions per unit of time and volume:

$$r \equiv \frac{N_R}{tV} = \frac{1}{V} \sigma J_{beam} N_{target} \tag{2.20}$$

where J_{beam} is the beam flux and N_{target} is the number of nuclei in the target. It is possible to express the flux as $J_{beam} = \nu N_{beam}/V = \nu n_b$, where n_b indicates the numerical density of particles of the beam and with ν the relative speed between beam and target. In this way N_{target}/V is precisely the numerical density of particles of the target n_t and that the cross section depends on the energy of the process or, consequently, of the speed. Finally one can write:

$$r = \sigma(\nu) \nu n_t n_b \tag{2.21}$$

In a stellar environment, however, the speed between the beam and the target is not uniquely defined but rather follows a distribution determined by the thermodynamic conditions. We can therefore generalize

the previous equation as:

$$r = n_t n_b \int \sigma(v) P(v) v dv \equiv n_t n_b \langle \sigma v \rangle \tag{2.22}$$

where $P(v)$ is the relative velocity distribution, normalized to unity in the range $[0, \infty[$, and $\langle \sigma v \rangle$ is the reaction rate per pair of interacting particles, i.e. the integral of the product between the cross section and the relative velocity between them weighted for the velocity distribution. The latter, in most cases studied by nuclear astrophysics, is precisely the *Maxwell-Boltzmann* distribution for a classic gas, therefore:

$$P(v)dv = \left(\frac{\mu}{2\pi kT}\right)^{3/2} e^{-\mu v^2/(2kT)}\, 4\pi v^2 dv \tag{2.23}$$

where μ is the system reduced mass, $k = 8.6173 \times 10^{-5} eV/K$ is the Boltzmann constant and T is the system temperature. However, it is often more convenient to express the cross section as a function of the energy of the system, therefore it is also necessary to express 2.23 as a function of energy: remembering that $E = \mu v^2/2$ e $dE = \mu v dv$ we can switch the variables and get

$$P(E)dE = \frac{2}{\sqrt{\pi}} \frac{1}{(kT)^{3/2}} \sqrt{E} e^{-E/kT} dE \tag{2.24}$$

The maximum value of the *Maxwell-Boltzmann* distribution is obtained at the value $v_T = \sqrt{2kT/\mu}$ which corresponds, if you decide to use the expression as a function of energy, to an energy equal to $E = kT/2$. In a stellar site where the temperature remains almost constant, the reaction rate therefore depends mostly on the cross section. The latter is usually expressed as a function of the energy of the system, rather than the speed, therefore it is usually preferred to also express the reaction rate as a function of energy, starting from the distribution 2.24, this form is valid for all processes induced by charged and non-charged particles:

$$\langle \sigma v \rangle = \int \sigma(v) P(v) v dv = \left(\frac{8}{\pi\mu}\right)^{1/2} \frac{1}{(kT)^{3/2}} \int_0^\infty \sigma(E)\, E\, e^{-E/kT} dE \tag{2.25}$$

If the reaction is induced by neutrons, it is possible to apply a further simplification by considering, instead of the reaction rate per pair $\langle \sigma\nu \rangle$ the product between the most probable speed and the average of the cross section weighted on the Maxwell-Boltzmann distribution (MACS) $\langle \sigma \rangle_T \nu_T$. This average is precisely the integral

$$\langle \sigma \rangle_T = \frac{\langle \sigma\nu \rangle}{\nu_T} = \frac{4}{\nu_T^2 \sqrt{\pi}} \int_0^\infty \nu \sigma_n(\nu) \left(\frac{\nu}{\nu_T} \right)^2 e^{-(\nu/\nu_T)} d\nu \tag{2.26}$$

Having thus obtained the various expressions for the reaction rate, it is necessary to distinguishing the cases in which the cross section of the process presents a continuous "smooth" variation as a function of energy from the cases in which the variation it is very fast at a certain energy values, which are known as resonances. The latter, in nuclear physics, can be formally treated in different ways but they are essentially the result of the population of a collective state of the intermediate system given by the interaction between the beam and target nuclei. Thus, it can be said that the cross section of a process has a continuous background due to different contributions among which different discrete peaks, corresponding to the resonant processes, may stand out.

2.3.1 Resonant Reactions

Quite often the cross-sections studied are significantly dominated by resonances arising from the excitation of a nuclear level of the compound nucleus. If the resonance is narrow, i.e. its width at half height is negligible with respect to the value of its centroid, and isolated, i.e. it is possible to resolve this resonance with respect to any other resonances of the system close to it, it is possible to use the known Breit-Wigner formula for a single-level resonance:

$$\sigma_{BW}(E) = \frac{\pi}{k^2} \frac{(2J+1)}{(2j_b+1)(2j_t+1)} \frac{\Gamma_{in}\Gamma_{out}}{(E-E_R)^2 + \Gamma^2/4} \tag{2.27}$$

where $\lambda = 2\pi/k$ is the De Broglie wave length while δ_{bt} is a Kronecker delta which is equal to unity only if the beam and target nuclei are the same. Moreover Γ_{in} is the partial width of the entrance channel, given by the product between twice the barrier penetrability ($2P_\ell$) and the square of the *reduced width* $\left(\gamma^2\right)$, which incorporates within it all the effects and properties of the nuclear structure, meanwhile Γ_{out} is the one of the exit channel and Γ is the total width of the resonance. Finally j_b and j_t are the total spin of, respectively, a particle of the beam and one of the target, while J is the resonance total angular momentum and E_r is the resonance energy value.

The formula therefore shows that the cross section is directly proportional to the partial widths of the input channels but inversely proportional to its width. It also depends on a statistical factor linked to the number of states accessible by the resonant reaction. Substituting the 2.27 in the 2.25, we obtain the reaction rate for a narrow and isolated resonance, valid for both charged and neutral particles:

$$\langle \sigma\nu \rangle = \frac{\sqrt{2\pi}\hbar^2}{(\mu kT)^{3/2}}\,\omega \int_0^\infty \frac{\Gamma_{in}\Gamma_{out}}{(E_r - E)^2 + \Gamma^2/4}\, e^{-E/kT} dE \tag{2.28}$$

where, to simplify the presentation, we indicated with ω the statistical factor $(2J+1)\,(1+\delta_{bt})\,/\,(2j_b+1)\,(2j_t+1)$ which does not depend on energy and therefore can be taken out of the integral argument. Assuming the partial widths Γ_{in} and Γ_{out} constant along the whole energetic range of the resonance, it is possible to analytically solve the integral obtaining

$$\langle \sigma\nu \rangle = \left(\frac{2\pi}{\mu kT}\right)^{3/2} \hbar^2 e^{-E/kT} \omega\gamma \tag{2.29}$$

With γ we have indicated the relationship $\Gamma_{in}\Gamma_{out}/\Gamma$ and the product $\omega\gamma$ is called *strength* of the resonance and is proportional to the area subtended by it. The reaction rate therefore depends only on the energy and on the strength of the resonance, the exact form of the resonance does not come into play. Therefore, it is evident that this treatment, obtained

in the case of narrow and isolated resonances, is not applicable in the case of a broad resonances, or resonances in which the FWHM begins to be significant compared to the value of the centroid, as for the latter the exact dependence on the energy of the cross section is also significant. In this case the cross-section should be defined as:

$$\sigma(E) = \sigma(E_r)\frac{E_r}{E}\frac{\Gamma_1(E)}{\Gamma_1(E_r)}\frac{\Gamma_2(E)}{\Gamma_2(E_r)}\frac{\left[\Gamma(E_r)/2\right]^2}{(E-E_r)^2+\left[\Gamma(E)/2\right]^2} \tag{2.30}$$

2.3.2 Neutron induced non-resonant Reactions

In stars, neutrons are thermalized very quickly therefore nuclear reactions induced by neutrons occurs substantially at the speed given by the peak of the *Maxwell-Boltzmann* distribution. For neutrons in s-wave and low energy it has been seen that the trend of the cross section can be approximated to

$$\sigma \sim \frac{1}{\nu} \sim \frac{1}{\sqrt{E}} \tag{2.31}$$

This law, known as Wigner's law, is also valid in those cases where multiple resonant contribution combine together resulting in a smooth cross section. It is also valid when the reaction proceeds through a long tail of a broad resonance, which is something that often happens when dealing with *sub-threshold* resonances thanks to their long tail that extends above the threshold. If we consider in particular the tail at lower energy of a very large resonance ($E << E_r$) we can easily analytically verify the Wigner's law. We can take the Breit-Wigner formula 2.27 and consider the following approximations: $E << E_r$, $\Gamma_{out} \sim cost.$. If we also consider the energy dependence of Γ_{in} for low energy neutrons [3] and the partial wave factorization:

$$\sigma_{\ell=0} \sim \frac{1}{\nu^2}\Gamma_{\ell=0} \sim \frac{1}{\nu^2}\nu \sim \frac{1}{\nu} \tag{2.32}$$

The reaction rate for a cross section following this law is therefore, as seen also in the previous chapter, a constant and can also be expressed in

terms of Maxwellian averaged cross-section. For low-energy neutrons in the s wave it also follows that

$$\langle\sigma\rangle_T \nu_T = \sigma(\nu_T)\nu_T \tag{2.33}$$

therefore it would be possible, in principle, to obtain the reaction rate by simply measuring the cross section for the value ν_T, although in reality the measurement of the cross section is usually repeated at different energies, included in the range of greatest probability, to improve the experimental error. However, non-resonant reactions do not always strictly follow this law which, as said, is an approximation. Therefore it is not valid for all those cases excluded by the conditions we applied, that is when the neutron energy is not small or the contribution of the partial waves with $\ell > 0$ is not negligible. For the latter case it is sufficient to consider the approximation $\Gamma_\ell(\nu) \sim (\nu R)^{(2\ell+1)}$ to obtain approximate cross section values for each partial wave: $\sigma_{\ell=1} \sim \nu$ or $\sigma_{\ell=2} \sim \nu^3$. The reaction rate can be obtained with equal simplicity considering that $(\nu R)^{(2\ell+1)} \sim E^{(\ell+1/2)}$:

$$\langle\sigma\nu\rangle \sim \int_0^\infty E^{(\ell+1/2)} e^{-E/kT} dE \tag{2.34}$$

The presence of ℓ as a power of the energy involves a shift in the statistical factor $Ee^{-E/kT}$ of the generic formula 2.25, this corresponds, as shown in the figure 2.5, to a shift in the range of greater probability of the cross section, i.e. the window within which, in a stellar environment, the reaction usually takes place.

2.3.3 Charged particle induced non-resonant Reactions

In case of reactions between charged particles that proceed without resonances, it is possible to substitute in Eq. 2.25 the definition of the S-factor in Eq. 2.18 and write:

$$\langle\sigma\nu\rangle = \left(\frac{8}{\pi\mu}\right)^{1/2} \frac{1}{(kT)^{3/2}} \int_0^\infty e^{-2\pi\eta}\, S(E)\, e^{-E/kT} dE \tag{2.35}$$

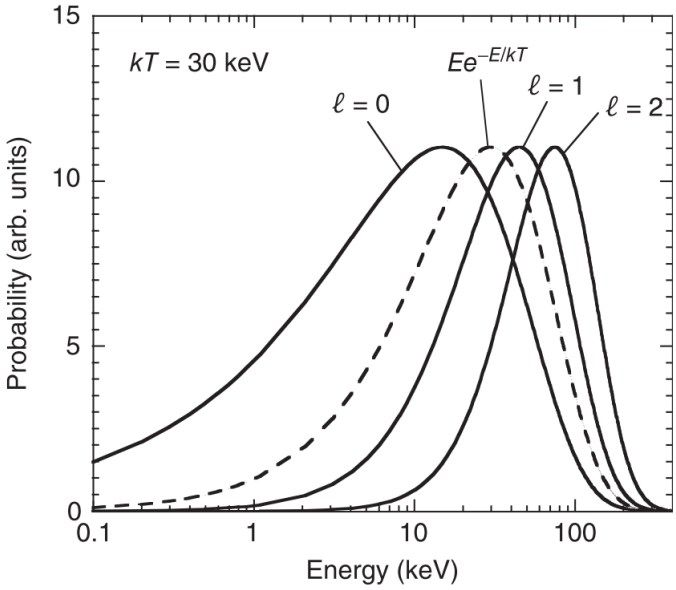

Figure 2.5: Graphical representation of the statistical factor $Ee^{-E/kT}$ as a function of energy as the value of the quantum number ℓ varies.

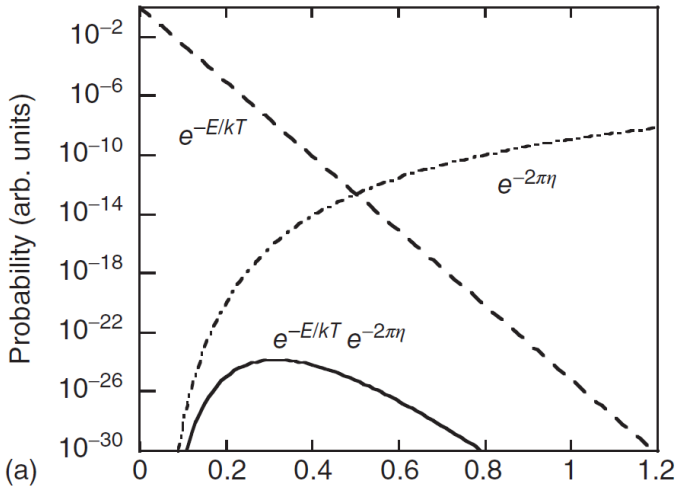

Figure 2.6: Representation of the *Maxwell-Boltzmann* distribution (dashed line), Gamow factor (dashed dotted line) and their convolution (solid line) [3].

When studying the energy dependence of the integrand, as it can be easily seen in Fig. 2.6, one can notice that the factor $e^{-E/kT}$ coming from the Maxwell-Boltzmann distribution, decreases to zero for high energies meanwhile the Gamow factor, as already explained, decreases to zero at low energies. The latter can be rewritten as an explicit function of the energy considering that:

$$2\pi\eta = 0.989 Z_1 Z_2 \sqrt{\mu \frac{1}{E}} \tag{2.36}$$

The Gamow factor therefore shifts the peak of the *Maxwell-Boltzmann* distribution to higher energies, which are usually part of the tail of the distribution. For this reason the convolution between the two distributions is usually referred as the "Gamow peak" and its energy range is the one at which the nuclear reactions of astrophysical interest occurs in stars. Finally, if we consider the S-factor, which is a smooth varying function, as a constant for the integral it is then possible to rewrite Eq. 2.35 as:

$$\langle \sigma\nu \rangle = \left(\frac{8}{\pi\mu}\right)^{1/2} \frac{S_0}{(kT)^{3/2}} \int_0^\infty \exp\left(-\frac{E}{kT} - \sqrt{\frac{E_G}{E}}\right) dE \tag{2.37}$$

where E_G is the "Gamow energy" and is merely a parameterization of the Gamow factor. Going back to the Gamow peak one can notice that it can be reasonably approximated to a Gaussian distribution having its maximum at an energy E_0 which would the centroid of the distribution. It is possible to approximate the argument of the exponential in order to obtain a Gaussian distribution, as it follows [3]:

$$\exp\left(-\frac{E}{kT} - \sqrt{\frac{E_G}{E}}\right) \sim \exp\left(-\frac{3E_0}{kT}\right) \exp\left[-\left(\frac{E-E_0}{\Delta/2}\right)^2\right] \tag{2.38}$$

where Δ is the width of the Gamow peak and it can be evaluated to be [3] equal to:

$$\Delta = \frac{4}{\sqrt{3}} \sqrt{E_0 kTa} = 0.24 (Z_1^2 Z_2^2 \mu T_9^5)^{1/6} \tag{2.39}$$

Finally we can rewrite Eq. 2.37 inserting the Gaussian approximation

$$\langle \sigma\nu \rangle \simeq \left(\frac{8}{\pi\mu}\right)^{1/2} \frac{S_0}{(kT)^{3/2}} e^{-3E_0/kT} \int_0^\infty \exp\left[-\left(\frac{E-E_0}{\Delta/2}\right)^2\right] dE \tag{2.40}$$

and by changing, without introducing a significant , the lower limit of the integral from 0 to $-\infty$ it is finally possible to solve the integral:

$$\langle \sigma\nu \rangle \simeq \sqrt{\frac{2}{\mu}} \frac{\Delta}{(kT)^{3/2}} S_0 e^{-3E_0/kT} \tag{2.41}$$

Chapter 3

Theoretical and Experimental Methods for Nuclear Astrophysics

3.1 Experimental challenges in nuclear astrophysics

Nuclear reactions are the engine that makes nucleosynthesis in the universe possible, however, their direct study in the laboratory under the same astrophysical conditions is quite challenging due to the many differences between the stellar environment and terrestrial laboratories. First and foremost one has to consider that stellar matter is a plasma meanwhile reactions studied in the laboratory occur between partially ionized beam and neutral targets. Moreover, the abundance of elements in astrophysical sites is multiple scales of magnitude greater than the one in the laboratory. Those differences have a profound impact on the experimental activity of nuclear astrophysics: thermonuclear fusion reactions occur in stars at energies below the Coulomb barrier thanks to quantum tunneling, as we saw in the previous chapter of this thesis. Thus such reactions are mainly induced in the so-called Gamow energy region which, as it can be seen in 3.1 is defined as the convolution between the probability of tunneling through the Coulomb barrier and the energy distributions

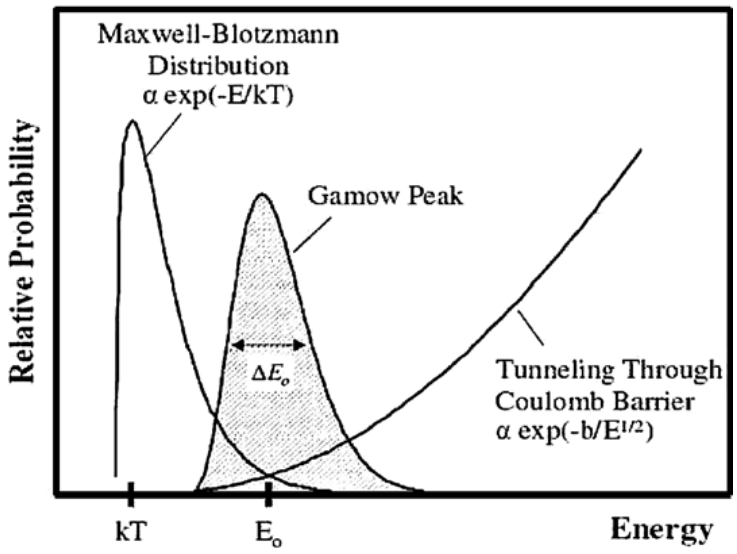

Figure 3.1: Graphical representation of the Maxwell-Boltzmann probability distribution, the Coulomb barrier penetration probability by tunnel effect and their convolution, colored in gray, all as a function of energy.

of the interacting nuclei and/or particles. While for neutron induced reactions only the centrifugal barrier is present the barrier effect is however still relevant, especially at highers values of the angular momentum between the interacting nuclei.

When considering the typical temperatures at which reactions occur in the astrophysical sites, the related Gamow window usually sits at ranges of the order of hundreds of keV down to substantially zero energy, which is significantly lower than those usually studied in nuclear physics laboratories. These low energy values are quite problematic to study in the laboratory, even with accelerators working at low energies, since the reaction cross-section are very small ($10^{-9} \div 10^{-12} barn$) due to both the centrifugal (charged and neutral particles) barrier and Coulomb (charged particles) barrier. In a typical stellar environment this low value is largely compensated by the large number of particles that could interact but in the laboratory we are limited by the density of targets and by the beam intensity.

Studying events with such low rates inevitably results in a signal-to-noise ratio in the detectors that is vanishingly small. Usually therefore, in order to carry out direct measurements in the laboratory, two alternative ways are followed: reduce noise to the minimum possible by performing measurements in a highly shielded laboratory or at energies greater than the Gamow window and then extrapolate the cross-section or the S-factor to lower energies. This is also relevant when working with neutron induced reactions, due to the centrifugal barrier. Moreover one must take into account also the experimental difficulties that arise when working with neutrons. The obtained result is however inevitably affected by the actual mathematical operation: extrapolating the value of a function beyond its known domain it is feasible only for functions that vary very slowly with a predictable trend. Unfortunately this is not true when considering the cross-section as a function of energy both for a non-resonant reaction but even more when considering the presence of resonances since they are, by definition, *sudden* variations of the cross section.

Indeed in the case of a non-resonant reaction, as visible in top portion of Fig. 2.4, at very low energies right in the range of astrophysical interest, the cross section varies so rapidly that any extrapolation in this region is indeed impossible. To reduce systematic errors, as anticipated in the previous chapter, it was decided to extrapolate not the value of the cross-section but rather the so-called S-factor which was defined in Eq. 2.18. In this way, as visible in the bottom part of Fig. 2.4, the steep variation of the cross-section at low energies, due to the barrier penetration, is transformed into the slowly variable S-factor. This of course cannot help much in the resonant case due to the aforementioned sudden variations: for known resonant states this can be mitigated by using for example the R-Matrix theory, more on that will be described in the dedicated section. Unfortunately, despite all these precautions, direct measurements of reactions between charged particles face a further problem which is presently unavoidable: the electron screening. When we defined

the cross-section in Chapter 2 we assumed that the interacting nuclei were completely stripped of the electron cloud which surrounds them in ordinary matter. Usually we refer to this by saying that we have considered the "bare nuclei" cross-section. However this hypothesis is not completely true either in the stellar environment or in the laboratories on Earth: in the first case matter is in a plasma state, so nuclei are mostly stripped of electrons but still immersed in a electron sea, meanwhile on Earth the situation is different since nuclei are surrounded by a cloud of electrons in the atom. In both cases the cloud or sea of electrons, having a charge opposite to the positive charge of the protons in the nucleus, lowers the value of the Coulomb barrier actually experienced by the nuclei during their interaction, subsequently causing an increase in the barrier penetration likelihood. Since the charge distribution is substantially different in those two cases, the electron screening effect and the relative enhancement factor of the barrier penetrability is markedly different. To trace the measurement of the cross section conducted in the laboratory to the one actually valid in a stellar environment it would be necessary to measure the electronic screening in both conditions.

3.2 Indirect methods

To help solving the issues listed so far, in the last few decades various indirect methods have been developed and used to successfully evaluate the cross section of the reaction of interest by studying a complementary reaction properly chosen. Among all the indirect methods the one used in this thesis is the Trojan Horse Method (THM) which will be extensively explained in the following paragraph. In addition to THM, the most used methods are undoubtedly the asymptotic normalization coefficient (ANC) and coulomb dissociation (CD) techniques.

The ANC method exploits the evidence that the direct capture of a particle by nuclei usually occurs on the tail of the nuclear overlap func-

tion in the corresponding two body channel. The shape of this overlap function is given by the Coulomb barrier meanwhile the absolute scale can be changed by a normalization factor, the so-called ANC, which is related to the cross section of the direct capture process. This method was successfully applied to study the S-factor of the $^8Be \rightarrow^7 Be + p$ reaction by studying the $^{10}B(^7Be,^8 B)^9Be$ and $^{14}N(^7Be,^8 b)^{13}C$ transfer reactions [10].

The CD method uses a virtual photon, generated by the Coulomb interaction between the beam and heavy nuclei thick target, to induce a photo-dissociation process in the nuclei of the beam itself. If the nucleus a of the beam has a cluster configuration $b + c$, it is possible to study the break-up reaction $a + T \rightarrow b + c + T$, where T is the target. By studying this process it is possible to evaluate the cross section of the photo-disintegration $a + \gamma \rightarrow b + c$ and subsequently, by the means of the detailed balance method, it is possible to study the inverse radiative capture process $b + c \rightarrow a + \gamma$. This method was applied to the three-body $^{208}Pb(^{16}O, \alpha^{12}C)^{208}Pb)$ study the $^{12}C(\alpha, \gamma)^{16}O$ reaction and to the $^{208}Pb(^8B, p^7Be)^{208}Pb)$ to study the $^7Be(p, \gamma)^8B$ [11] .

3.2.1 The Trojan Horse Method

The Trojan Horse method (THM), first proposed by Baur[12] in the 1986, in order to study a two body reaction of interest uses a properly chosen three-body reaction in which one of the interacting nuclei has a well known clustered state and acts as a "Trojan Horse" in a way that it will be clear once the basic features and theoretical foundations of the method will be explained in this section. The THM lays its foundations on the well established direct reactions theory, in particular on the so-called "quasi-free" (QF) break-up reactions, which will be explained in the following paragraph. Assuming we want to obtain the cross section of the binary process $x + A \rightarrow b + B$ at astrophysical energies, the THM would be applied to a ternary reaction, called Trojan Horse (TH) reaction, $a + A \rightarrow b + B + s$ where $a = x + s$ is a nucleus with a high probability of

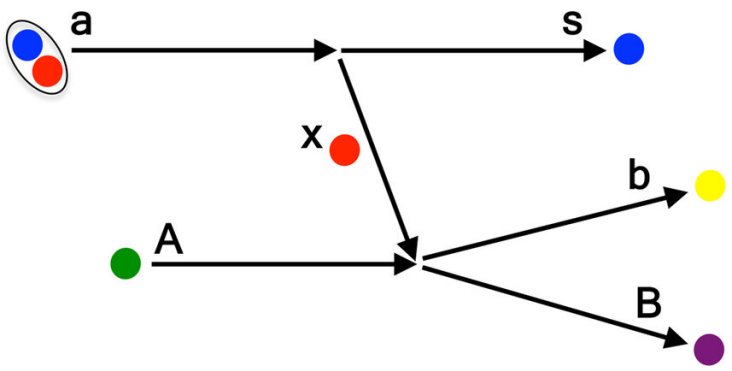

Figure 3.2: Diagram of the TH reaction: the top vertex refers to the quasi-free break-up, while the bottom vertex refers to the two-body reaction of interest. The colors are used to facilitate observation [13].

having a cluster structure. A diagram of the process can be seen in Fig. 3.2.

The cluster x is called "participant" as it will actively take part in the interaction, meanwhile the cluster s is called "spectator". This nomenclature is not by chance and it derives from the formalism of quasi-free reactions in which only a part of the nucleus, usually a single nucleon, takes part in the reaction while the remaining part is practically unperturbed by the interaction.

Quasi-Free break-up

To better understand the THM it is helpful to describe how the reaction evolves: one of the two nucleus, either a or A, is accelerated to such energies as to overcome the potential barriers between it and the other nucleus in the entrance channel, so as to maximize the cross section for the three-body reaction and suppress the any barrier effect. Once the barrier is overcome, the TH nucleus a undergoes a break-up splitting into its two constituent clusters, x and s. Then, if the reaction takes place under the quasi-free regime, only cluster x interacts with the nucleus while the

cluster s continues undisturbed, preserving the momentum it had inside the TH nucleus. To achieve this the relative momentum, in the entrance channel, between the TH nucleus and the nucleus A must be such as to resolve distances lower than those between the two clusters inside the TH nucleus. Thus, the QF break-up gives the greatest contribution to the cross section of the three-body reaction in the phase space region where the relative momentum between the two clusters x and s is zero or very small compared to the momentum of the TH nucleus in the entrance channel [14]. This QF kinematics condition is the best[14] condition for treating cluster s as a spectator since it minimizes the interaction between it and participating cluster x, which corresponds to stating that the distance between them is maximized.

The reaction represented in figure 3.2 is invariant to rotations around the beam axis, therefore, considering the energy-momentum conservation laws, it is regulated only by four Galilean invariant variables which by themselves completely determine the kinematics of the reaction. Thus, during the experiments the emission angles and the energy of only two of the three particles in the final state are measured meanwhile the variables of the third particle are analytically reconstructed. It can be shown [14] that the cross section of the QF process has a maximum for certain pairs of angles of the two measured particles, which usually take the name of *quasi-free angles*: it is therefore ideal to place the detectors at these angles to maximize the expected yield of the desired mechanism as much as possible.

Then by applying the conservation of the energy-momentum to both vertices of the diagram in figure 3.2 we obtain one of the fundamental equations of the THM formalism which defines [14] the relative energy between the cluster x and the nucleus A in the system of reference of the center-of-mass between these two particles:

$$E_{xA}^{c.m.} = \frac{p_{xA}^2}{2\mu_{xA}} - \frac{p_{sx}^2}{2\mu_{sx}} - \epsilon_{sx}^a \tag{3.1}$$

where μ_{xA} and μ_{sx} are the reduced masses, meanwhile p^2_{xA} and p^2_{sx} are the *off-energy-shell* momenta, respectively between the x cluster and the nucleus A and between the clusters x and s. ϵ^a_{sx} is the binding energy between these two cluster inside the TH nucleus a. By applying the quasi-free kinematics condition which means considering the value of p^2_{sx} as negligible, Equation 3.1 can be simplified as follows:

$$E^{c.m.}_{xA} = \frac{\left(p^{QF}_{xA}\right)^2}{2\mu_{xA}} - \epsilon^a_{sx} \tag{3.2}$$

where with p^{QF}_{xA} we have indicated the same variable seen in Equation 3.1 above but calculated under the QF kinematics condition. With this equation another of the advantages of THM is easily shown: the presence of the binding energy in Eq. 3.2 with negative sign allows to lower the energy in the center of mass between the x cluster and the nucleus A, which makes it possible to reach, as will be seen in the analysis of the experimental data, even energies lower than the threshold of the two-body reaction, thus being able to study sub-threshold resonances that may be present in the two-body channel of interest.

Plane Wave Impulse Approximation

The Plane Wave Impulse Approximation (PWIA) considers the interaction so rapid that it can be approximated as occurring only between the incident wave, which in the case of the PWIA is precisely a plane wave not distorted by any field effects, and only a few nucleons of the nucleus. It is usually stated that the PWIA is valid only at high energies [15] but in reality, as also demonstrated by the works of the Nuclear Astrophysics groups of Catania and Zagreb [16, 17], it is rather necessary to evaluate the impulse transferred in the interaction: therefore the condition on the energy must also include the Q-value of the reaction, which makes it possible to apply the approximation also in reactions where the beam energy is generally not considered to be high. Indeed, the validity condition of

the approximation is not so much on the energy transferred as on the *time* needed for the transfer: in fact, to consider an interaction as "impulsive" it is necessary that the transit time inside the nuclear matter is much shorter than the characteristic time of the nucleus. This is equivalent to saying that the nuclear system does not have time to *notice* and *respond* to the presence of the incident wave as a collective nucleon system. Therefore the interaction takes place between the wave and just a single nucleon or, as in the THM case, a cluster of the nucleus. In general, we can define the transit time as:

$$\tau_{tr} = \frac{2R_N}{v_{beam}} \tag{3.3}$$

where R_N is the nuclear radius, meanwhile v_{beam} is the speed of the beam's particles accelerated on the nucleus. The characteristic time of the nucleus is defined instead as:

$$\tau_{nucl.} = \frac{2\pi}{\omega_{nucl.}} = \frac{2\pi\hbar}{BE} \tag{3.4}$$

where $\omega_{nucl.}$ is the characteristic frequency of the nucleus meanwhile BE is the binding energy of the nucleus. The PWIA condition is thus written as follow:

$$\tau_{trans.} \ll \tau_{nucl.} \rightarrow \frac{2R_N}{v/c}\frac{BE}{2\pi\hbar c} \ll 1 \tag{3.5}$$

Using in the Eq. 3.5 approximated values such as $2R_N \sim 2fm$, $v/c \sim 0,103$ which corresponds to a beam energy of about 5 MeV/nucleon, $BE \sim 6MeV$, $\hbar c = 200MeV\,fm$ one obtains the condition $1/50 \ll 1$ which is satisfied. It is clear, however, that the shorter the transit time, compared to nuclear time, the better the accuracy of the approximation. Therefore, using the PWIA, whose validity has just been underlined for the purposes of this thesis, it is possible to link [18] the differential cross section of the three-body TH reaction with that of the two-body reaction of interest:

$$\frac{d^3\sigma_{TH}}{d\Omega_b d\Omega_B dE_b} \propto K.F.\ |\Phi(p_s)|^2 \left(\frac{d\sigma_{xA}^{b.n.}}{d\Omega}\right)_{HOES} \tag{3.6}$$

K.F. is the so-called *kinematic factor* derived, together with the 3.6, in the appendix of Ref. [18] and which includes various factors linked, as the name suggests, exclusively to the kinematics of the reaction:

$$K.F. = \frac{k_b k_B^2 E_s E_{c.m.}^2}{k_A E_a \left\{k_b E_s + E_b \left[k_b - k_A \cos\theta_b + k_A(\cos\theta_B - \cos\theta_b)\right]\right\}} \tag{3.7}$$

where k_i is the momentum of the i-th particle. In Eq. 3.6 also appears the square of the absolute value of the spectator's wave function (w.f.) inside the nucleus a expressed in the momentum space, which is linked to the w.f. in the coordinate space by the Fourier transformation:

$$\Phi(\mathbf{p}_s) = (2\pi)^{(-3/2)} \int_{-\infty}^{+\infty} d^3\mathbf{r}\ \psi(\mathbf{r}_s)\ e^{(-i\mathbf{p}_s\mathbf{r}_s)} \tag{3.8}$$

Finally $\left(d\sigma_{xA}^{b.n.}/d\Omega\right)_{HOES}$ is the differential cross section, evaluated half-off energy-shell, of the two-body reaction in the case of *bare nuclei*, which means that the interaction between the nucleus is evaluated without any electron in their surrounding. To obtain the valid value in the stellar environment it is therefore necessary to incorporate electronic screening for the plasma state, evaluated in other ways. It should also be emphasized that Eq. 3.6 is not an exact equation but a proportionality relation: this means that the values obtained will be determined up to a constant of proportionality, that is, they will be expressed in *arbitrary units*. It is therefore necessary to normalize the values obtained by a THM experiment with datasets in absolute units: this is often achieved by using data from direct measurements.

Results of the method

For several decades now, the application of the Trojan Horse Method to Nuclear Astrophysics has made it possible to obtain significant results, providing information on the trend of the astrophysical factor, on the electronic screening potential and on the astrophysical reaction rates. Numerous reactions induced by charged particles have been studied during

the last 20 years, as reported in Ref.[19, 20] and references therein, and in the last 10 years it has also been successfully applied to neutron-induced reactions [21, 22].

3.3 R-matrix formalism

3.3.1 Theoretical framework

When studying the cross section of reactions usually there is not a sharp separation between the resonant and non-resonant contribution, as we saw in the previous chapter. In reality quite the contrary is actually true: in most cases a series of resonances are dominant over a non-resonant background contribution. As we saw, the study of reactions of astrophysical interest requires often to extrapolate the value of the cross section at energies lower than the one measured in the laboratory. To do so, in the past, a phenomenological approach was used: for example when dealing with reactions at low energy forming a low level density compound nucleus, usually a single Breit-Wigner formula was used. This approach is however not precise enough when dealing with more complex systems since it neglects certain contributions from low energy mechanisms. It is clear therefore that there is a desperate need of a theory capable of taking into account all the possible contributions to the cross section with mathematical rigor. To this aim the R-matrix theory was applied to the study of nuclear astrophysics experimental data. The first assumption of the R-matrix method is that configuration space of the system ca be sharply divided in two distinct region: the internal one, where the system is represented by the eigenstates base and interactions are regulated by the many-body nuclear physics, and an external one where only the Coulomb interaction remains and therefore the system is represented by an exact analytical solution. The R-matrix approach then makes a second assumption: the wave functions and their derivatives in the two regions

must match at the connection point between the two. Usually this is called "boundary surface" and is thought to be approximated by the sum of the radius of the two interacting nuclei. In order to match the w.f. at the boundary radius R, one can write the radial part of the w.f. in the external region, calculated for $r = R$ [23, 24]:

$$\phi_c = \left(\frac{1}{v_c}\right)^{1/2} (y_c I_c + x_c O_c) \tag{3.9}$$

where I_c and O_c are the incoming and outgoing wave functions, which as we have seen in Eq. 2.15 depend on the Coulomb wave functions F_c and G_c, while y_c and x_c are the incoming and outgoing amplitudes and v_c is the relative velocity. In all of these variables we can see the index c: this is a compact representation of what the R-matrix theory calls a *channel*, which is defined by a specific particle pair, among all the possible combination in which the compound nucleus can be formed or decay, with a specific angular momentum and spin coupling. Therefore $c = \alpha sl$ where α represent the particle pair, s the channel spin and l is the relative angular momentum between the nuclei of the pair. Now, introducing the collision matrix **U** defined by the relation

$$x_c = -\sum_{c'} U_{cc'} y_{c'} \tag{3.10}$$

and inserting it into Eq. 3.9 we can write the external w.f. just in term of the incoming wave amplitudes:

$$\phi_c = \left(\frac{1}{v_c}\right)^{1/2} \left(y_c I_c - \sum_{c'} U_{cc'} y_{c'} O_c\right) \tag{3.11}$$

Similarly we can evaluate, again at the boundary radius, the radial part of the w.f. in the internal region which is given by the expression [23, 24]:

$$\varphi_c = \left(\frac{\mu_c a_c}{\hbar^2}\right)^{1/2} \sum_{c'} \left[R_{cc'} \left(\frac{\hbar^2}{\mu_{c'} a_{c'}}\right)^{1/2} \left(\rho_{c'} \varphi'_{c'} - B_{c'} \varphi_{c'}\right) \right] \tag{3.12}$$

where μ is the reduced mass, a the channel radius, $\rho = ka$ is the product between the wave number k and the channel radius, B is the boundary condition, which is just the logarithmic derivative of an eigenstate w.f. evaluated at the boundary radius, and finally R is the so-called R-matrix which is defined as

$$R_{cc'} = \sum_{\lambda} \frac{\gamma_{\lambda c} \gamma_{\lambda c'}}{E_\lambda - E} \tag{3.13}$$

where γ is the reduced width amplitude of the channel, i.e. the measure of the strength of the contribution from the resonant level λ to the w.f. of the channel c, given by the formula

$$\gamma_{\lambda c} = \left(\frac{\hbar^2}{2\mu_c a_c}\right)^{1/2} \int X^*_\lambda \psi_c dS \tag{3.14}$$

in which X is the eigenstate w.f. meanwhile ψ_c is the surface channel w.f. . In the R-matrix approach therefore the reduced width amplitude and the eigenenergy E_λ are treated as free parameters that need to be determined by the experimental data fit. Finally matching the solutions in the two regions it is possible to relate the collision matrix to the R-matrix by the following matrix relation:

$$\boldsymbol{U = \rho^{1/2} O^{-1} (1 - RL_0)^{-1} (1 - RL_0^*) I \rho^{-1/2}} \tag{3.15}$$

The matrices $\boldsymbol{\rho, O, I, B}$ are defined with only the diagonal elements ρ_c, I_c, O_c and B_c, respectively, meanwhile $\boldsymbol{L_0 = \rho O' O^{-1} - B}$. In order to solve this relation it is necessary to invert the channel matrix $\boldsymbol{(1 - RL_0)}$, this is a trivial calculation if the are many levels but only a few channels, however in the opposite case, when there are few levels and many

channels to calculate, the time for the inversion exponentially increases. In order to more easily perform the calculation there is another relation used:

$$U_{cc'} = \Omega_c \Omega_{c'} \left\{ \delta_{cc'} + i \sum_{cc'} \Gamma^{1/2}_{\lambda c} \Gamma^{1/2}_{\lambda' c'} A_{\lambda\lambda'} \right\} \tag{3.16}$$

where $A_{\lambda\lambda'}$ is the level matrix and it is defined as

$$(A^{-1})_{\lambda\lambda'} = (E_\lambda - E)\delta_{\lambda\lambda'} + \Delta_{\lambda\lambda'} - \frac{i\Gamma_{\lambda\lambda'}}{2} \tag{3.17}$$

in which we introduced the resonance partial width $\Gamma_{\lambda c} = 2P_c\gamma^2_{\lambda c}$ and the level shift $\Delta_{\lambda\lambda'} = -\sum_c \gamma_{\lambda c}\gamma_{\lambda' c}(S_c - B_c)$. From this formula it also clear the relation between the R-matrix parameters and the one actually measured when studying a nuclear reaction. However, the simple definition for the partial width Γ is in truth complicated by the dependence of the reduced width amplitudes γ and of the eigenenergies E_λ on the boundary condition, which is defined for each group of levels with the same J^π. Therefore, to convert the *formal* R-matrix parameters to the *experimental* resonance parameters a set of mathematical transformations were developed[25]. Once the collision matrix $U_{cc'}$ is calculated, it is possible to obtain the angle-integrated total cross section of the reaction going from $\alpha \to \alpha'$ which is given by

$$\sigma_{\alpha\alpha'} = \frac{\pi}{k^2_\alpha} \sum_{Jll'ss'} \left[\frac{2J+1}{(2I_{\alpha 1}+1)(2I_{\alpha 2}+1)} \left| T^J_{cc'} \right|^2 \right] \tag{3.18}$$

where we used the transition matrix in place of the collision matrix since they are related via the following formula:

$$T_{cc'} = e^{2i\omega_c}\delta_{cc'} - U_{cc'} \tag{3.19}$$

in which ω_c is the Coulomb phase shift. It is possible also to find an expression of the differential cross-section which depends on the transition

matrix, however, in that case a more complicated and rigorous calculation is needed.

3.3.2 The AZURE2 code for R-matrix calculations

There are various code available to the community to perform the R-matrix analysis, among which we decided to use AZURE2, a multi-level multi-channel R-matrix code publicly available and developed by a collaboration supported by the JINA[26] network and under the leadership of R.E.Azuma, hence the name of the code. It is designed to analyze reactions induced by charge particles, neutrons and γ rays in the resolved resonance region of astrophysical interest. Therefore, if was developed from the start to study reactions occurring at low energies with the main focus being extracting, from the experimental data regarding the cross section and angular distribution, the level partial widths or bound state normalization parameters, such as the ANC, other than the level energy itself. Being a multi-level and multi-channel code, it is possible to include, obviously as long as they are allowed by conservation laws, all the channels, i.e. all the various reactions that can populate the compound state or to which the latter can decay, and all the desired resonant levels of the compound state taken into exam. This means that we can have a best-fit of the cross-section using at the same time all the various datasets for all the possible reaction channels, which is exactly what we were looking for. Moreover the code automatically takes into account all possible interference between levels which can have a significant impact on the cross-section, thus better evaluating the fitted parameters. This means that since the datasets included in the calculation come from different experiments, for each one a precise evaluation of target thickness effects and energy calibration must be performed. For this reason the code has an entire section devoted to the experimental effects evaluation. The code also allow to extrapolate the behavior of the cross section or the S factor at energies which are not covered by experimental data, this, however,

should be taken as what it is: a prediction based on the experimental data and R-matrix theory, but still a prediction. Moreover, as we will se in the dedicated section, the code can also calculate the reaction rate for a list of temperatures given by the user, therefore by using a proper sampling it is possible to properly calculate the reaction rate.

It should be clear by now that AZURE2 was developed with the nuclear astrophysics community in mind and indeed it quickly became one of the most used R-matrix codes both within the JINA[26] and international nuclear astrophysics networks such as IReNA[27]. Thanks to its versatility and being relatively easy to use, i.e. the code integrates Brune [28] and Barker[25] transformations for R-matrix parameters thus allowing to input and output directly the R-matrix "observable" parameters, the code has been widely used by also the nuclear structure and applied nuclear physics communities. One downside of using such codes to perform the analysis is that they usually only uses routines such MINUIT2 for χ^2 minimization, when performing the fit, but then they leave to the end user, which should know exactly what are the errors involved in each of the measurements used for the fit, the burden of evaluating the actual errors on each parameter. It is immediately clear that this approach can easily get out of hand when the number of datasets and parameters used starts to grow. An alternative solution, that has been developed in the last years, could be to shift away from "classical" frequentist approach that researchers have employed to apply phenomenological R-matrix models to data. In recent years, Bayesian methods have gained a lot of interest across the astrophysics and nuclear physics community: this led the way for the application of Bayesian methods also to R-matrix analysis [29].

3.3.3 Bayesian statistic and the Markov Chain Monte Carlo

Bayesian analysis treats the parameters of the chosen model as true random variables and then evaluates their probability distribution function (PDF) using the well-known Bayes theorem which states that the *posterior*

PDF of the parameters Θ, given the data $\boldsymbol{D}$, is equal to the ratio between the product of the *likelihood* PDF of $\boldsymbol{D}$, given the parameters Θ, for the *prior* PDF of Θ and the *model evidence* PDF of $\boldsymbol{D}$. In formula:

$$p(\Theta|D) = \frac{p(D|\Theta)p(\Theta)}{p(D)} \tag{3.20}$$

Bayesian approach therefore uses probability functions to describe what is known about the parameters, however applying the theorem on its own in real situations where probabilistic inference is used is quite complicated: we need to compute the three PDFs in Eq. 3.20 however, while $p(D|\Theta)$ and $p(\Theta)$ can be easily expressed, since they are part of the model and in most cases are actually explicitly known, the model evidence requires to compute the following integral:

$$p(D) = \int_{\Theta} p(D|\Theta)p(\Theta)d\Theta. \tag{3.21}$$

While this calculation could be easily achieved when dealing with a low dimension parameter vector Θ, when the number of parameters starts to increase the operation can become intractable: the exact evaluation of the posterior PDF is practically impossible. For this reason a series of approximation techniques have been developed to compute the solutions to problems that require to know this posterior without dealing with the model evidence PDF calculation. This can be done because we are not changing the experimental data during the R-matrix analysis, thus in our case $p(D)$ is therefore just a normalization factor that we can rightly ignore. Among the various method that have been developed to overcome this issue, in recent years Markov Chain Monte Carlo (MCMC) methods are becoming the status of art for sampling the posterior PDFs. Indeed, MCMC methods can be used even without a full analytic description of the posterior PDF since they assume no model for this PDF. As a consequence they do not require to compute any process-intensive task, such as calculating derivatives or integrals of the function, they have a low

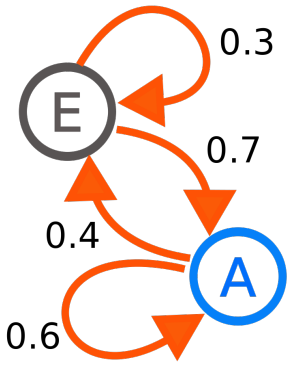

Figure 3.3: Schematic drawing of a simple Markov chain[30]

bias and high variance, which means that they are more computational expensive than competing methods but the final result is more accurate. A Markov chain is a model that describe a stochastic system which can transit through a series of states according to certain probabilistic rules.

The base idea of MCMC is then to use Monte Carlo techniques to sample these probabilistic rules instead of trying to exactly calculate the chain by simulating a random sequence of states long enough to almost reach the equilibrium, which will correspond to the chain system we actually want to study. This means that the desired posterior PDF is the *equilibrium distribution* of the Markov chain, which is uniquely defined for the the chain. Many of the practical MCMC applications uses a Metropolis-Hasting algorithm [31, 32] to generate the chain which takes advantage of the reversibility property of the Markov chain: this means that every transition between two states of the chain is reversible, i.e. the probability to go from the state A to B is equal to the probability of going from state B to A. The so-called *"walker"* of the algorithm generates a candidate for the next move in the chain based on the current state, then the candidate is either accepted and stored as the new value, or rejected and the generation of the candidate restart from current value. This choice is taken by

comparing the values of probability function for the current and for the candidate state with respect to the desired distribution.

However, in this way two subsequent samples are correlated with each other and they do not correctly represent the equilibrium distribution, even though over the long run they actually do. This could be a serious issue leading to large errors in the calculation, especially when the sample size is not significantly higher than the number of samples required to loose the correlation. Usually therefore only the states that are separated by a number of steps higher than the so-called *auto-correlation time"* are saved on disk. This *autocorrelation time* is the time, expressed in number of iterations, that the system requires lose any correlation between the current state and a previous one. Moreover, although the Markov chain will eventually converge to the equilibrium distribution, at the beginning of the sampling procedure the walkers may diverge from the equilibrium and the chain will follow a very different distribution: for this reason usually a "burn-in" phase is defined during which the computed samples are thrown away. Finally, when dealing with a parameter space with an high number of dimension, finding the next candidate in the chain start to become computational intensive since the parameter in each dimensions there may behave in a very different way than the others. It can be seen [31, 32] that his method heavily depends on $N(N+1)/2$ "tuning parameters", where N is the dimension of the parameter space, which, in a multivariate calculation, will quickly scale out of hands. For this reason in the last decades several heuristic methods have been developed in order to solve the problem of generating the next move in the chain in a data-driven fashion. In 2010 Goodman and Weare [33] proposed a new and powerful approach: rather than just creating one walker that goes through the chain generating the moves in the parameter space, they thought to follow many walkers simultaneously. In this way, the proposals for new candidate state for each walker now depends on the relative locations of the other walkers. In a sense the group of walkers

now evolves like one ensemble of walkers, moving through the parameter space like a single entity. Therefore each walker evolution depends on its starting point, the definition of which is left to the end user. The most common way is to have a point in the parameters space that it is thought to be close to the equilibrium and then generate the rest of the initial walkers by perturbing the parameter values only slightly. Another, totally different, approach is generate the start of the walkers in random points in the parameter space: however this would easily lead to a series of problem. Indeed, considering the possibility of multiple local maxima for the posterior distribution of the parameters, the walkers can end up to those totally different maxima, which means that the next candidate move will now end up on multiple valleys. In this way only a very small fraction of generated proposals could be accepted wasting precious computational resources.

Once the initial value is set the algorithm has to generate each move of the multiple walkers spawned. Now, instead of proposing and evaluating only one update per step as in Metropolis-Hasting algorithm, the candidate generation and evaluation is done for each of the spawned walkers in a single step. In literature one can find various approaches to do so but the one that Goodman and Weare [33] recommend is what they call a *stretch move*, where the next point in the parameter space is generated as

$$X_k(t) \rightarrow X_j(t) + Z\left[X_k(t) - X_j(t)\right] \tag{3.22}$$

where j and k are different walkers and Z is a scaling variable. In summary, MCMC is an extremely powerful method for sampling a multidimensional space and these recent improvements have significantly improved both the speed and accuracy of the method.

3.3.4 The *emcee* and BRICK Python packages

Multiple MCMC codes are available nowadays but four our analysis we used the *emcee* [34] Python package that is based on the Goodman and Weare algorithm [33] described above. This package has been thoroughly used in astrophysics, so it is already well established in the physics community, has a well documented API and uses the HDF5 file format [35] to store all the steps taken by the chain, which is of fundamental importance for our application since it gives us the ability to read each step of the evolution also after the calculation. To use this package the end user needs to declare the model it wants to use for the calculation: the function to calculate the likelihood must be defined, the initial values of all the parameters and their prior distributions must be explicitly declared. The package will then take care to generate the *walkers* of the MCMC chain, calculate the posterior probability and store everything on disk. In our case, however, we do not need to redefine the likelihood function since it can be easily obtained by invoking the AZURE2 code and perform a simple calculation using the current values of the parameters vector Θ as the input. Therefore we need just a way to let *emcee* and AZURE2 communicate with each other: to this aim, the BRICK (Bayesian R-Matrix Inference Code Kit) python package was developed [29]. By initializing an instance of an *"AZR"* object in BRICK, by simply indicating the path of the AZURE2 input file we want to compute, the packages takes care of initializing the whole workspace, reading the input file parameters and pass them to the *emcee* package for the initialization. Moreover, when calculating the likelihood probability the code will take care of calling back AZURE2 to let it perform the R-matrix calculation in the current point of the parameters space. This means creating a new, temporary workspace for AZURE2, which needs to be thoroughly cleaned after the calculation is performed: indeed having multiple walkers that concurrently runs means that actually multiple instances of AZURE2 needs to be created without generating any conflict. Using an algorithm implemented in emcee that

evaluates the auto-correlation time is then possible to stop the calculation when this variable does not change, which means that the chain should be indeed stable and therefore should have reached the equilibrium state we are interested in. Another approach is to directly input in the code the number of steps that each walker has to take before killing the calculation. The output file can then be used to extract various information such has the evolution of each parameter for each of the walkers used and the posterior distributions which we need for our analysis.

3.4 Modified R-matrix

The THM formalism, originally developed using the surface approximation for non-resonant reactions, has been further expanded to study the case of resonant reactions and deduce the resonance parameters of interest. The parametrization of the model, treated in details in Ref. [36, 37, 38, 39], takes a form similar to the one of the R-matrix formalism: for this reason it is usually referred to as *Modified R-matrix*. In this section we will report a summary of the theoretical model alongside the equations relevant to our analysis.

If we consider the TH reaction as transfer into the continuum, i.e. a transfer to an unbound nucleus intermediate state which will then decay, and we disregard the spin and any other internal degree of freedom of the particles involved in the reaction, we can write the TH reaction amplitude in the post form as [36]:

$$\tilde{M}(\boldsymbol{P}, \boldsymbol{k_{aA}}) = \left\langle \chi^{(-)}_{k_{sF}} \Phi^{(-)}_{F} \middle| \, \Delta V_{sF} \, \middle| \Psi^{(+)}_{i} \right\rangle \tag{3.23}$$

where:

- $F = x + A = b + B$ is the intermediate system;
- $P = \{\boldsymbol{k}_{sF}, \boldsymbol{k}_{bB}\}$ the 6D momentum matrix describing the three body $(s + b + B)$ system in the exit channel;

- $\chi^{(-)}_{k_{sF}}$ is the distorted wave of the system $s + F$;
- $\Phi^{(-)}_F$ is the w.f. of the system F;
- $\Delta V_{sF} = V_{sF} - U_{sF}$ is the difference between the interaction potential V_{sF}, between s and F, and their optical potential U_{sF};
- $\Psi^{(+)}_i$ is the exact $a + A$ scattering w.f..

Then, using the spectral decomposition of $\Phi^{(-)}_F$ given in Eq. (3.8.1) of Ref. [40] it is possible to write $\Phi^{(-)}_F$ using a shell-model-based resonant R-matrix representation which is similar to the level decomposition formula for the internal w.f. in the R-matrix approach we saw in this chapter. In formula:

$$\Phi^{(-)}_F \approx \sum_{\nu,\tau=1}^{N} \tilde{V}^{bB}_{\nu}(E_{bB})[\boldsymbol{D}^{-1}]_{\nu\tau}\Phi_{\tau} \tag{3.24}$$

where N is the number of levels, ν and τ are excited states of the intermediate system, $\tilde{V}^{bB}_{\nu}(E_{bB}) = \left\langle \chi^{(-)}_{bB}\varphi_b \left| \Delta V_{bB} \right| \Phi_{\nu} \right\rangle$ is the resonant form factor for the decay of the compound state F_{ν}, represented by the Φ_{ν} w.f. , into the final state $b + B$, χ_{bB} is the distorted w.f. of the two body final state. Finally $\boldsymbol{D}$ is a matrix similar to the level matrix we saw in the R-matrix formalism, a in depth treatment can be found in Ref. [40]. By substituting Eq. 3.24 into Eq. 3.23 we obtain the N-level, two channels generalization of the R-matrix for the TH reaction:

$$\tilde{M}^{(TH)}(\boldsymbol{P}, \boldsymbol{k_{aA}}) \approx \sum_{\nu,\tau=1}^{N} \tilde{V}^{bB}_{\nu}(E_{bB})[\boldsymbol{D}^{-1}]_{\nu\tau}\tilde{M}_{\tau}(\boldsymbol{k}_{sF}, \boldsymbol{k}_{aA}) \tag{3.25}$$

where $\tilde{M}_{\tau}(\boldsymbol{k}_{sF}, \boldsymbol{k}_{aA}) = \left\langle \chi^{(-)}_{sF}\Phi_{\tau} \right| \Delta V_{sF} \left| \Psi^{(+)}_i \right\rangle$ is the amplitude of the transfer reaction $a + A \rightarrow s + F_{\tau}$ that populates the τ excited state of the intermediate system F. This amplitude is intended as the exact form

which can be well approximated by the DWBA amplitude, where the exact solution of the $\Psi_i^{(+)}$ w.f. is substituted with the approximation $\varphi_a \varphi_A \chi_{aA}^{(+)}$. However, when we talked about the THM in this chapter we used the PWIA where any distortion of the entrance channel is disregarded. This further approximation is still valid in this formalism since, for values of $\boldsymbol{k}_{xA}$ sufficiently high the interaction will take place only between the participant cluster x and the A particle, without any contribution from the interaction with the spectator such as rescattering effects. Under the PWIA the transfer amplitude is simply the Fourier transform of the inter-cluster $s-x$ w.f. and, subsequently, its square is the momentum distribution of the intercluster $s-x$ motion that we already described in the section dedicated to the THM. In formula:

$$\tilde{M}_\tau^{PWIA}(\boldsymbol{k}_{sF}, \boldsymbol{k}_{aA}) = \left\langle e^{i\boldsymbol{k}_{sF}\cdot\boldsymbol{r}_{sF}} \varphi_s \Psi_\tau \right| V_{sA} + V_{xA} \left| \varphi_a \varphi_A e^{i\boldsymbol{k}_{aA}\cdot\boldsymbol{r}_{aA}} \right\rangle \approx \tag{3.26}$$

$$\approx \left\langle e^{i\boldsymbol{k}_{sF}\cdot\boldsymbol{r}_{sF}} I_{xA}^{F_\tau} \right| < V_{xA} >_{Ax} \left| I_{sx}^a e^{i\boldsymbol{k}_{aA}\cdot\boldsymbol{r}_{aA}} \right\rangle$$

where $I_{xA}^{F_\tau} = \langle \varphi_A \varphi_x | \Phi_\tau \rangle$ and $I_{sx}^a = \langle \varphi_s \varphi_x | \varphi_a \rangle$ are the overlap function, respectively, between the w.f. of F_τ and the bound-state w.f. of x and A and between the bound-state w.f. of a and the bound-state w.f. of s and x. Finally, $< V_{xA} >_{Ax}$ is just is the expectation value of V_{xA} for the $\varphi_A \varphi_x$ state. Under the hypothesis that the reaction proceeds via isolated non-interfering resonances and by applying further simplifications [41] it is possible to define the double-differential TH cross section as:

$$\frac{d^2\sigma}{dE_{xa} d\Omega_s} = K \sum_i (2J+1) \cdot \left| \sqrt{\frac{k_f \, E_{xa}}{\mu_{cd}}} \frac{\sqrt{2P_{l_i}(k_{cd}R_{cd})} M_i(p_{xa}R_{xa}) \gamma_{cd}^i \gamma_{xa}^i}{D_i(E_{xa})} \right|^2 \tag{3.27}$$

where K is a normalization factor, introduced due to the fact that the HOES cross section is obtained in arbitrary units, P_{l_i} is the penetration function for the l_i wave, R_{bB} and R_{xA} are the channel radii, γ are the

reduced widths for each channel, $D_i(E_{xA})$ is the standard R-matrix denominator in the case of one-level, two-channel R-matrix formula [23]. $M_i(\boldsymbol{k}_{xA}R_{xA})$ is the TH reaction amplitude defined now as [41]:

$$M_i(p_{xa}R_{xa}) = \left[((B_{xa})_i - 1)j_{l_i}(\rho) - \rho\frac{\partial j_{l_i}(\rho)}{\partial\rho}\right]. \tag{3.28}$$

where $j_{l_i}(\rho)$ are the spherical Bessel functions and B_{xa} is an arbitrary boundary condition chosen as described in Ref. [41]. It is worth noticing that, similarly to what we have seen for the R-matrix formalism, the differential cross section is proportional to the inverse of the level matrix but, unlike the typical R-matrix formalism, here we have only the transfer amplitude in the entrance instead of the channel width $\Gamma = 2P_l\gamma^2$ which is present only for the exit channel. This is in line with what it has been already said regarding the absence of any barrier effect in the entrance channel of the TH reaction.

Chapter 4

Study of the $^{17}O(n,\alpha)^{14}C$ reaction

4.1 Status of Art

As already mentioned in the previous chapters, the $^{17}O(n,\alpha)^{14}C$ reaction can be a possible poison reaction for the weak-component of the s-processes in a temperature window ranging from 0.16 to 1.3 GK. For such a reason, cross section data have to be measured at energies between 0 and 300 keV. At such energies, the $^{17}O(n,\alpha)^{14}C$ ($Q_{value} = 1.82MeV$) cross section has been already measured in the past both via direct [42, 8, 43] and indirect [44, 22] measurements.

In the work of Guardo et al.[22] the authors displays the experimental cross section data, which we report in Fig. 4.1. There it is shown the cross section as a function of the energy in the center-of-mass (c.m.) for three direct measurements [42, 8, 43] of the $^{17}O(n,\alpha)^{14}C$ reaction and a study [45] of the inverse reaction $^{14}C(\alpha,n)^{17}O$.

One can immediately notices that in the data by Wagemans et al. [43], indicated by the empty triangles in figure 4.1, two resonances are populated, namely the one at about 170 keV due to the intermediate ^{18}O $E^* = 8.213MeV$, $J^\pi = 2^+$ excited level and the one at 240 keV due to the population of the $E^* = 8.282MeV$, $J^\pi = 3^-$ excited level. The same

$E^*_{^{18}O}$ (MeV)	J^π	$E^{theo.}_{c.m.}$ (keV)	$\Gamma_c.m.$ (keV)
8.039	1^-	-5.74	<2.5
8.125	5^-	80	n.a.
8.213	2^+	168	1.0 ± 0.8
8.282	3^-	237	8 ± 1

Table 4.1: Excited states of ^{18}O in the range of astrophysical interest: in the first column the excitation energy of the level in MeV is expressed, in the second the value of J^π for the respective level is indicated, in the third energy value in the c.m. of the $\alpha - ^{14}C$ pair and in the last the natural width of the state. [46]

resonances are also populated by the measurement of Sanders et al. [45] although their experimental resolution is worse than the natural width of the explored levels. The remaining cross section data sets do not clearly allow us to disentangle the contribution of these two resonances and, further, at energies lower than 150 keV all the available datasets do not agree well with one another. Below 1 keV, it is also possible to observe in the data of Wagemans et al. a slow growth in the cross-section that could be linked, as suggested by the authors, to either Wigner's law (Eq. 2.31) or to the presence of a sub-threshold resonance with a long tail.

The table 4.1 shows the the spectroscopic properties of the four excited states of the ^{18}O intermediate system that come into play in the range of astrophysical interest $(0 < E_{c.m.} < 300keV)$ with their respective values of J^π. It is evident that the last two levels are at energies similar to the resonant structures observed by Wagemans et al. [43] while there is no trace of the first two levels in any of the datasets: the first is located at -5 keV below the threshold and, based on its width, could contribute to the rise below 1 keV also observed by Wagemans et al. [43]; the second, on the other hand, is absent from any direct measurements because of its $J^\pi = 5^-$ high value. Indeed, by applying the selection rules for the spin and the angular momentum, it is possible to see that the level is

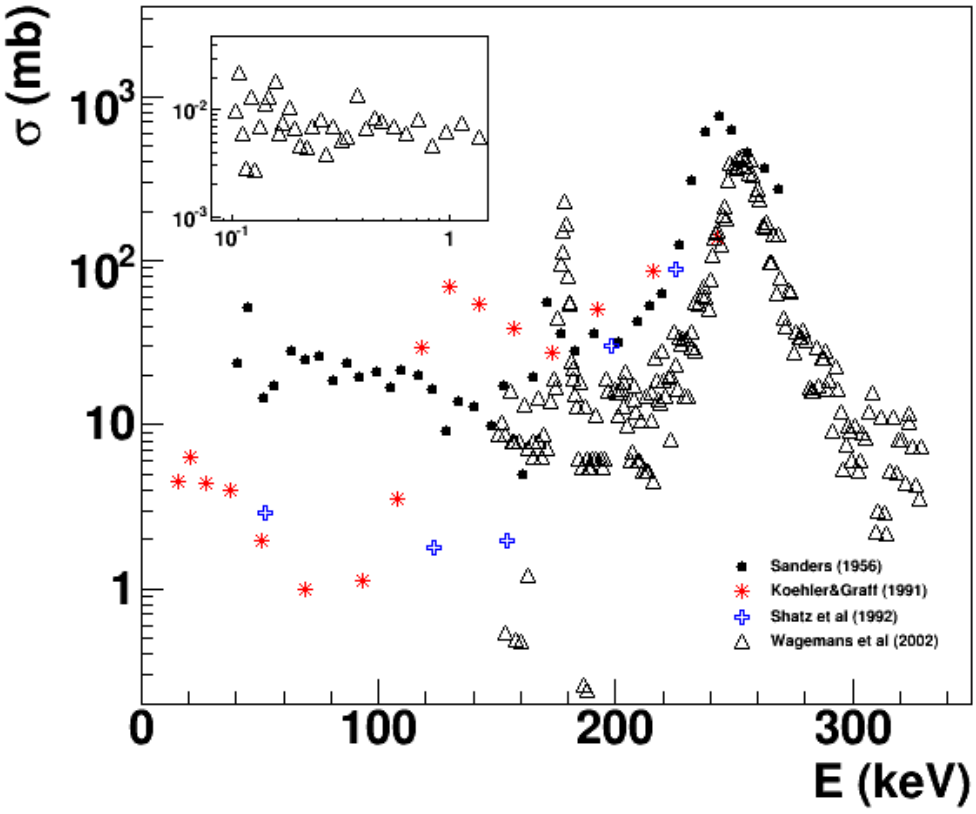

Figure 4.1: Cross section as a function of energy for the reaction $^{17}O(n,\alpha)^{14}C$ for the only four direct measurements available to date.[22]

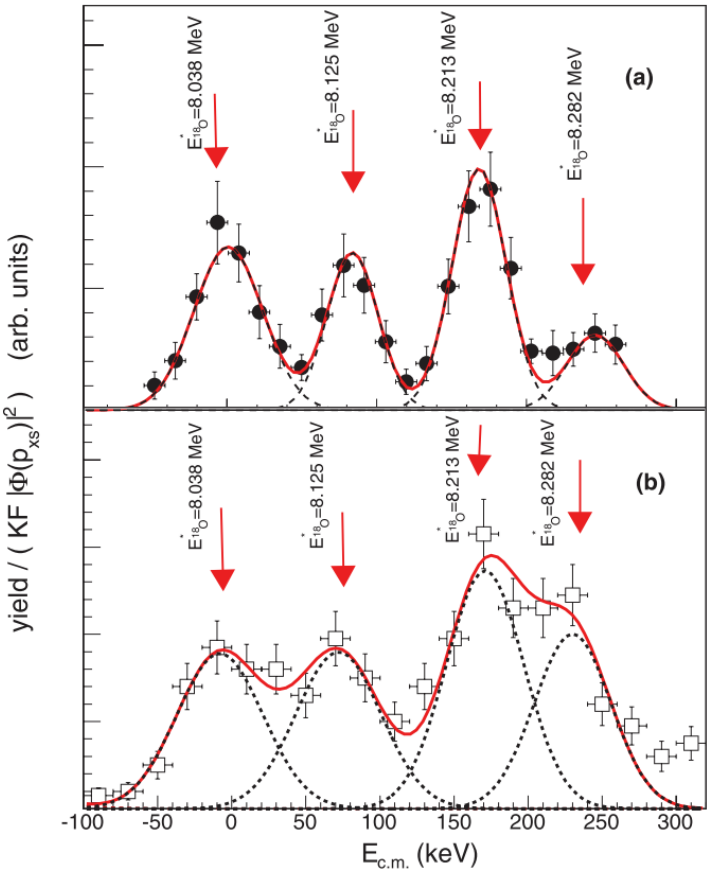

Figure 4.2: THM data of the $^{17}O(n,\alpha)^{14}C$ reaction as obtained by (a) Gulino et. al[44] and (b) Guardo et al. [22]

populated only via $\ell = 3$, thus it strongly suppressed in direct cross section measurements because of the centrifugal barrier.

To shed light on the discrepancies between the already existing set, the $^{17}O(n,\alpha)^{14}C$ has been studied in the energy range of interest by using the THM [44, 22]. Figure 4.2 shows the THM data as discussed in Gulino et al. [44] (top) and Guardo et al. [22] (bottom).

These two aforementioned indirect measurements confirm the presence of the resonant levels already assessed in the direct measurement of

Wagemans et al. and Sanders et al., however THM data also shows the two other resonant structures not present in direct data. The first one is located around 75 keV of energy in the c.m. frame, which corresponds to the population of the 8.121 MeV ^{18}O excited state. Due to the high angular momentum $\ell = 3$, it is suppressed in direct measurements while it is clearly populated in THM data because of the ability of the application to overcome both Coulomb and centrifugal barrier penetration effects. The second one is centered at -7 keV in the c.m., which corresponds to the 8.039 MeV level of ^{18}O, and it is indeed a sub-threshold resonance influencing the $^{17}O(n,\alpha)^{14}C$ cross-section at very low energy values.

These indirect measurements however would need further improvements: in the work of Gulino et al. the resonance at the highest energy was only partially populated by the experiment. For this reason the work Guardo et al. was carried out using a different facility and a slightly modified [22] experimental setup, covering a smaller region in $\theta_{c.m.}$, i.e. the angle between the particles in the exit channel evaluated in their c.m. frame. In this case the energy resolution was lower, as it can be seen from Fig. 4.2, than the one of Gulino et al. work and the detected resonances cannot be completely resolved. Therefore, to better resolve the resonances, evaluate the contribution of the sub-threshold one, cover a wider range in $\theta_{c.m.}$, obtain a lower statistical uncertainty and, finally, evaluate the overall reaction rate a new THM measurement with an improved experimental setup was carried out. In this chapter we will present the results obtained by the new THM experiment alongside a complete review of the direct data using the R-matrix formalism.

4.2 Applying the THM to the $^{17}O(n,\alpha)^{14}C$

4.2.1 TH Nucleus choice and kinematics

The first step in applying the THM is to choose the 3-body TH reaction appropriately, thus reflecting in a proper choice of the TH-nucleus which is indeed a fundamental one: even thought for the same participant cluster there may be various possible combinations with different spectator clusters, which leads to the formation of different TH nucleus, however, it is necessary to choose the combination that best approximates the requirements expressed in the theoretical works [15, 47] which are linked to [14]:

- the binding energy, the momentum distribution and the angular momenta between the two clusters of the TH nucleus;
- the momentum transferred by the participant cluster;
- the possibility of populating the kinematical region where the direct transfer contribution is maximized over sequential decays.

For the study of the $^{17}O(n,\alpha)^{14}C$ reaction we decided to use the deuteron as a TH nucleus to transfer the neutron. This means that the three-body reaction used to apply the THM is $^{2}H(^{17}O,\alpha^{14}C)p$. The choice of deuteron as a TH-nucleus is supported by a number of reasons:

- it has a very simple structure, being composed only of a proton and a neutron, and its wave function is well known [48];
- it has a relatively low binding energy, of only about 2.2 MeV;
- p-n relative motion mostly occurs in s-wave [48];

Since the p-n clusters motion in deuterium occurs in s-wave the momentum distribution has its maximum at 0 MeV/c, which corresponds

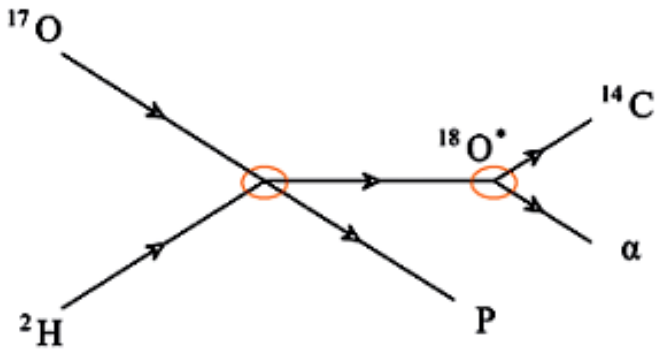

Figure 4.3: Pole diagram of the three body TH reaction of interest.

to large proton-neutron distances inside deuteron. This, as we discussed, is relevant for the QF mechanism we are interested in. The momentum distribution between the clusters can be described as the Fourier transformation of the Hultén [49] wave function:

$$\Phi(p_s) = \frac{1}{2\pi}\sqrt{\frac{ab(a+b)}{(a-b)^2}}\left(\frac{1}{a^2+|\mathbf{p}_s|^2} - \frac{1}{b^2+|\mathbf{p}_s|^2}\right) \tag{4.1}$$

where $a = 0.2317 fm^{-1}$ e $b = 1.202 fm^{-1}$ are two parameters with fixed values for deuterium [48].

The next step to apply the method is to choose the beam energy to reach in the c.m. of the two-body reaction the energy range of astrophysical interest. By inverting relation 3.2, it follows:

$$\frac{\left(p_{xA}^{QF}\right)^2}{2\mu_{xA}} = E_{xA}^{c.m.} + \epsilon_{sx}^{a} \tag{4.2}$$

Then, remembering the energy range of interest for the astrophysical application, we can choose the value $E_{xA} = 200 keV$ as the central value for the energy range. Remembering that the binding energy of the deuteron is equal to about 2.2 MeV, we get a value of $\left(p_{xA}^{QF}\right)^2/2\mu_{xA}$ equal to 2.4

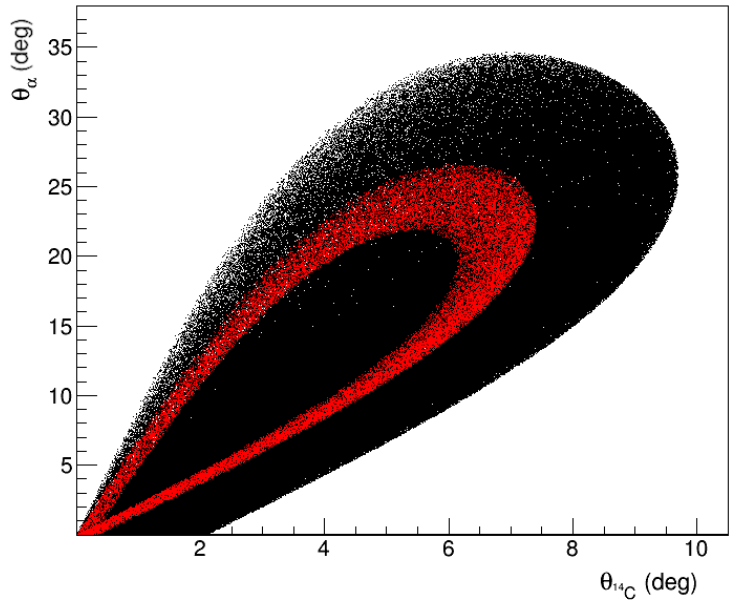

Figure 4.4: Two-dimensional plot of the emission angles of the α and ^{14}C nuclei as obtained from MC simulation: in black the pairs of angles that satisfy the condition $|p_s| < 30\,MeV/c$ while in red only those that satisfy the more strict condition $|p_s| < 5\,MeV/c$.

MeV: this is the kinetic energy transferred, under the QF conditions, to the participant cluster x. In this way it is possible to calculate the needed energy for the beam in the laboratory frame as:

$$E_{beam}^{lab} = 2.4MeV\frac{m_n + m_{^{17}O}}{m_n} \tag{4.3}$$

Substituting the values of the masses in 4.3, we obtain a beam energy of about 43.5 MeV in the laboratory frame. If we convert it in the c.m. system we would get an energy of about 4 MeV which is above the Coulomb barrier between the ^{17}O and deuterium, at about 2.8 MeV. As explained in the previous chapter, since the energy available in the reaction is much higher than the barrier we can rightly neglect its penetrability effects.

After the selection of the 3-body process, a devoted Monte Carlo (MC)

simulation was performed to single out the phase space regions we populate and, therefore, choose the angular range to explore for properly selecting the QF contribution of the $^2H +^{17} O$ interaction. Figure 4.4 shows the simulated emission angles for ^{14}C and α particles. As said, we need only to detect two of the three particles in the exit channel to completely define the kinematics of the process. The black points have been produced by imposing values to the momentum of the proton spectator of $|p_s| < 30 MeV/C$ while the red ones have a narrower selection of $|p_s| < 5 MeV/C$. Such a strict selection mimic the occurrence of the QF mechanism, i.e. the proton maintains in the exit channel the same momentum distribution it had inside deuteron before its break-up, thus allowing us to clearly see the phase space region we should cover with our detectors. In a sense the red points indicate us where the maximum of the spectator momentum distribution is located in the phase-space of the final particles, while the black points give us a more broad selection that will be used to select the QF events during the analysis of the data to cover an energy range in the c.m. frame rather than a single value of energy. In addition, Figure 4.5 shows the simulated 2D plot of the energy of the emitted ^{14}C and α particles in the $^2H + 17O$ interaction at 43.5 MeV: once again black points refer to the $|p_s| < 30\, MeV/c$ selection while the red ones refer to $|p_s| < 5\, MeV/c$. From the the inspection of the simulation results, we can conclude that the QF reaction channel should populate an angular region defined by the values $0 \leq \theta_\alpha \leq 35$ and $0 \leq \theta_{^{14}C} \leq 10$, while the energies of the emitted particles should range from 2 to 20 MeV for α particles and from 24 to 40 MeV for ^{14}C nuclei.

4.2.2 Experimental Setup

In the light of these results, the experimental setup was chosen to cover the selected angular regions.

In figure 4.6 a schematic drawing of the experimental setup used is shown. To detect in coincidence the α particles and the ^{14}C nuclei in

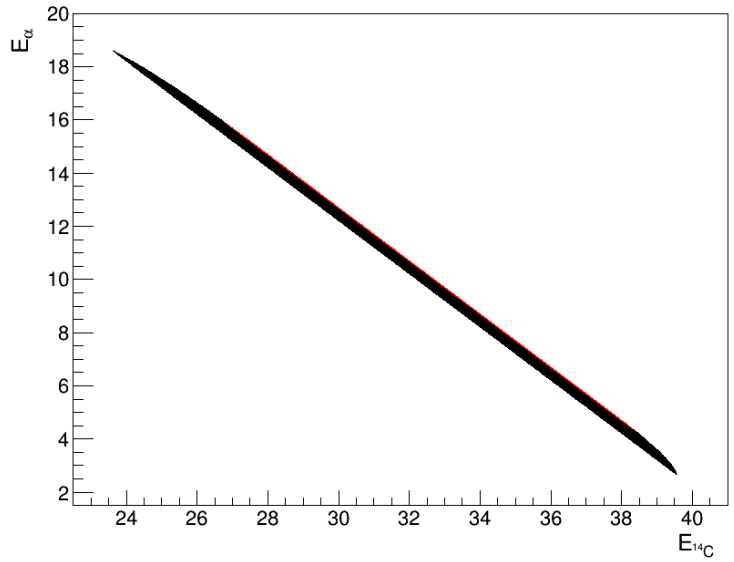

Figure 4.5: Kinematic locus obtained by MC simulation for the three-body reaction $^2H(^{17}O,\alpha^{14}C)p$ at the energy of 43.5 MeV by imposing a cut on the emission angles equal to $0 \leq \theta_\alpha \leq 35$ and $0 \leq \theta_{^{14}C} \leq 10$ and a cut on the spectator's momentum equal to $|p_s| < 30\,MeV/c$ (in black) and $|p_s| < 5\,MeV/c$ (in red).

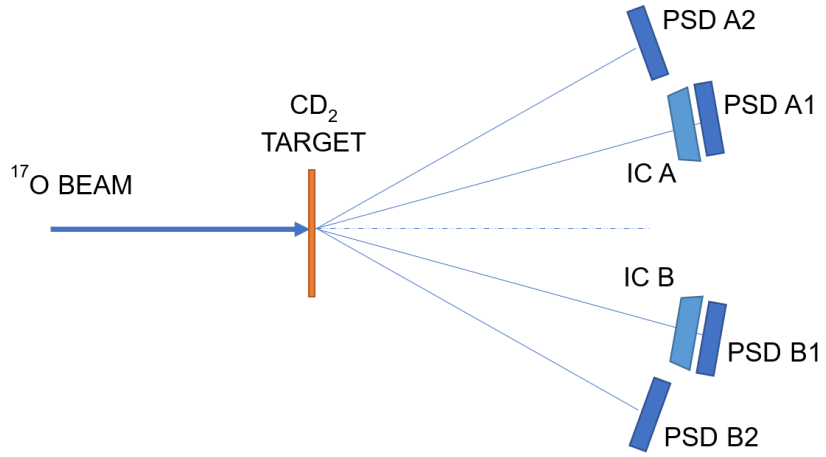

Figure 4.6: Sketch (not in scale) of the used experimental setup.

	θ (deg)	d (cm)
A1	7.5 ± 2.5	50
B1	7.5 ± 2.5	50
A2	22.5 ± 5	25
B2	22.5 ± 5	25

Table 4.2: Position of the detectors in the experimental setup: the first column refers to the angle with respect to the beam axis, while the second column refers to the distance between the detector and the target

the exit channel, two pairs (A1-B2, B1-A2) of silicon Position Sensitive Detector (PSD) were used, placed symmetrically with respect to the beam in order to double the statistics.

The A1 and B1 detectors were placed according to the MC simulation in order to cover the QF angular region of the ^{14}C nuclei while the detectors A2 and B2 were dedicated to the QF region populated by α particles. A1 and B1 detectors were also coupled to an ionization chamber (IC), placed in front of the PSD, to be used as a $\Delta E - E$ telescope for the identification in charge of the detected particles [50].

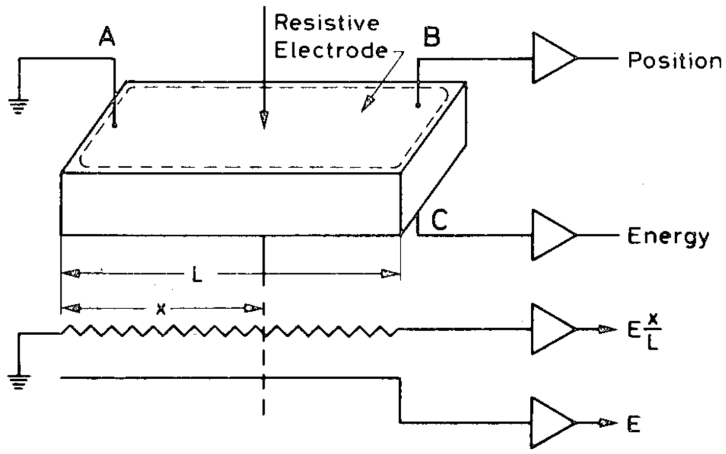

Figure 4.7: Schematic representation of a PSD and the relative functioning principles.

These A1 and B1 PSDs had a thickness of $1000\mu m$ while A2 and B2 were $500\mu m$ thick: these values were chosen to completely stop all the particles of interest inside the sensitive volume of the detector, as calculated via the LISE++ tool [51].

As shown in figure 4.7, a PSD is essentially a junction diode, consisting of a silicon crystal with different doping on each side, covered by a resistive electrode: when a particle hits the detector it generates a signal on the contact labeled "B" which is proportional to $E\frac{x}{L}$ where E is the energy released in the layer, x is the distance between the interaction point and the grounding connected to A and L is the overall length of the electrode. After crossing this resistive layer the particle proceed to interact with the depletion region of the diode, i.e. the diode region where no charge carriers are present, where it produces a number of charge pairs which will generate an electrical signal proportional to the energy [52].

For this type of detectors the measurement sensitivity on the position is $\pm 250\mu m$ while the final angular resolution obviously depends on the distance at which the detector is placed with respect to the target. In the present experiment, because of the target-detector distances, an intrin-

sic angular resolution of $0.03^\circ - 0.06^\circ$ was found. However, the overall spatial resolution is mainly affected by the beam spread. Indeed, with a diameter of about 1 mm, the spot of the beam on the target introduces a significant angular spread and consequently an uncertainty regarding the actual interaction point in the target which is higher to the intrinsic resolution of the detector. On the other hand, the overall energy resolution for this type of detector is usually estimated to be about 1 % [52].

The ionization chambers (IC) have a length of about 5 cm and are equipped with two windows, one at the entrance and one at the exit, of Mylar with a thickness of $1.5\mu m$: this value was chosen to withstand the difference between the internal and external pressure while, at the same time, minimize the energy loss of the detected particles. The chambers were filled during the entire duration of the experiment with isobutane gas, maintained at a constant pressure of 100 mbar. The energy resolution of the chambers was estimated to be about 10% [52] which is more than sufficient to discriminate the particles in charge, as required for this experiment.

4.2.3 Detector calibrations

To correctly calibrate the detectors it is better to use particles of charge and mass equal to those that we actually want to reveal during the experiment. Using different particles would entail, as is known from the Bethe-Bloch formula [52] , a different energy loss curve in the detector thus requiring a subsequent correction on the obtained calibration factors.

For this purpose, a series of experimental runs devoted to the calibrations were performed using different sources. For the PSDs dedicated to alpha particles both a radioactive source made of ^{228}Th, which emits alpha particles with 8 different energies, was used alongside different nuclear reactions which, unlike a radioactive source, have also the advantage of presenting a kinematic structure, i.e. the energy of the incident

particle varies with the angle of detection allowing us to perform also a better calibration of the position signal, as it will be discussed below. In particular, a beam of ^6Li was accelerated at energies of 15 and 18 MeV on a polyethylene target (CH_2) of 119 $\mu g/cm^2$ in order to exploit the nuclear reactions $^6Li + p \rightarrow \alpha +^3 He$ and $^6Li +^{12} C \rightarrow \alpha +^{14} N$. For these runs the detectors were momentarily moved to a suitable angle to span a region in which the α particles possess the desired energy for calibration. For the PSDs in the telescopes dedicated to the detection of carbon nuclei, elastic scattering reactions of a beam of ^{12}C on a gold target 146 $\mu g/cm^2$-thick were used. To populate different energy regions of the detector and have a fair number of experimental points for calibration, the beam was accelerated to five different energies: 40, 30, 25, 20, 15 MeV. For each of them, the measurements were carried out with the ionization chamber both empty and filled with isobutane gas at about 100 mbar. Although it is not necessary to fill the chambers, as their calibration is not necessary, they have been used in this way to degrade the energy of the beam, thus doubling the number of energies actually used. However, this choice also has negative sides: using a volume of gas to reduce the beam energy causes a significant energy spread linked to the variability with which the carbon nuclei lose energy as they pass through the gas.

Calibration of the energy signal

The dependence of the amplitude of the signal produced by the PSD on the energy released in its active volume is linear: this means that, by collecting a series of points with known energy, it is possible to construct a calibration line such as

$$E_{ch} = e_1 E_{th} + e_0 \tag{4.4}$$

where E_{ch} is the energy expressed in ADC channels,E_{th} is the known value of the energy, e_1 and e_0 are the coefficients to be obtained through the best-fit procedure of the experimental points of known energy col-

lected during the calibration runs.In the case of the ^{228}Th source, the energies of the emitted particles are tabulated while for the particles produced by nuclear reactions their energy was theoretically reconstructed by means of two-body kinematics calculations. Moreover, the energy loss in the different dead regions of the detectors, in half of the target, since it is assumed that on average the reaction takes place in the middle of it, and in the IC Mylar windows were also taken into account in the reconstruction of the energy of the particles after the reaction occurred in the target. In the case of the PSD used for the detection of carbon, it was also necessary to take into account, as mentioned, the energy loss in the gas of the ionization chamber, for those runs when it was used. It follows that the energy observed in the detector will be a "residual" energy linked to that actually energy possessed by the particle after the reaction through the relation:

$$E_{eff} = E_{res} + E_{loss} \tag{4.5}$$

The energy loss E_{loss} in each dead layer was estimated using the well-known LISE++ software[51].

Calibration of the position signal

As described above, the PSDs are devoid of any segmentation and provide a continuous signal in position, thus, to obtain reference values that can be used for calibration, a metal grid with vertical slits was placed in front of each of the detectors. As already mentioned, the amplitude of the signal in position is proportional both to the energy released by the particle in the active region of the PSD and to the ratio x/L as shown in figure 4.7. By plotting the position signals as a function of the energy signal also coming from the detector, it can be observed that this dependence described involves, as shown in figure 4.8, the formation, for each of the slits, of a locus of points that roughly follows a straight line, with a certain spread given by the width of the slits.

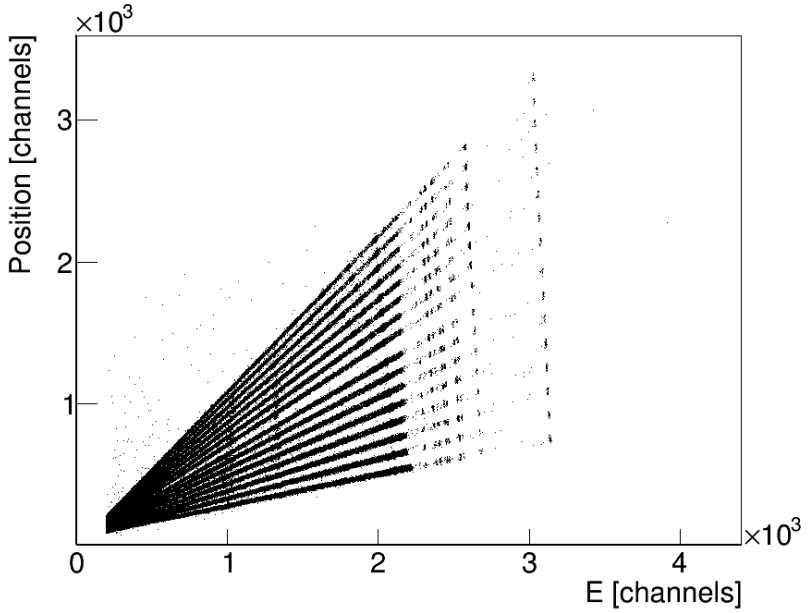

Figure 4.8: Raw position-energy two-dimensional plot (expressed in ADC channel number) for detector A2 from the calibration run with the ^6Li beam accelerated to the energy of 18 MeV on a polyethylene target.

A calibration function for this signal can be obtained with simple mathematical reasoning. Considering the amplitude of the position signal as a linear function (given the previous relationship) of both the energy and the angle, we can write:

$$P_{ch} = e_{1,1}\theta_{slit}E_{ch} + e_{0,1}E_{ch} + e_{1,0}\theta_{slit} + e_{0,0} \tag{4.6}$$

where $e_{1,1}$, $e_{0,1}$, $e_{1,0}$ and $e_{0,0}$ are again the parameters to be obtained through the best-fit procedure of the experimental points of known energy and angle.

Calibration parameters

After having determined all the coefficients of the relations 4.4 and 4.6 by means of the calibration procedure, it is possible, by inverting the

aforementioned relations, to obtain the two calibration functions, which can be then applied to the data obtained by the detectors during the proper measurement phase:

$$\begin{cases} E(MeV) & = \frac{E_{chan}-e_0}{e_1} \\ \theta(deg) & = \frac{P_{chan}-e_{0,1}E_{chan}-e_{0,0}}{e_{1,1}E_{chan}+e_{1,0}} \end{cases} \tag{4.7}$$

As a final test, the successful outcome of the calibrations was evaluated by plotting the calibrated angle values as a function of energy for the data acquired in the various calibration runs, alongside the known energy and position values used for the calibration itself.

In figure 4.9 it is possible to observe the two-dimensional plot $\theta(deg)$ - $E(MeV)$ referred to detector A2 for the events given by the reactions, induced by a beam of ^6Li accelerated to 18 MeV on the CH_2 target, where and alpha particle was present in the exit channel: namely the $^6Li +^{12} C \rightarrow^4 He +^{14} N$ and $^6Li + p \rightarrow^4 He +^3 He$ reactions. It should be noted that, being in this case the events linked to a two-body reaction, it is possible to observe how the points are arranged along a vertical curve given by the kinematics of the reaction. Moreover, it is possible to notice that for the $^6Li +^{12} C \rightarrow^4 He +^{14} N$ reactions there are multiple vertical loci of points: this is due to the fact that not only the ground state but also multiple excited states of the compound ^{18}F intermediate system are populated in the reaction. The seemingly missing points in the plot are absent because they were not used for the calibration due to either a low statistic in the experimental data. The good correspondence between theoretical and experimental points ensures the success of the calibration operation.

4.2.4 Selection of the $^2H(^{17}O,\alpha^{14}C)p$ reaction channel

Next it is necessary to correctly select the three body reaction of interest among the others that could arise from the interaction of the ^{17}O beam

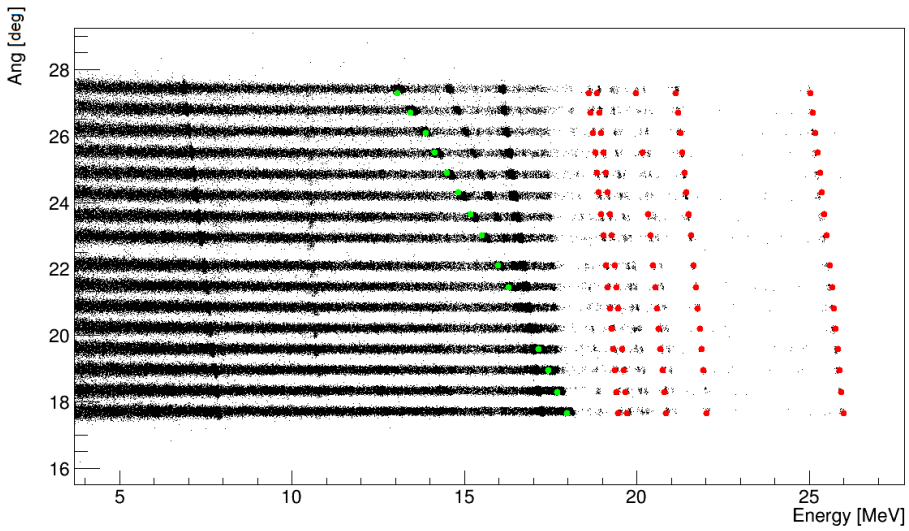

Figure 4.9: Angle versus energy calibrated 2D plot for the B1 detector. The theoretical points for the two reactions actually used for the calibrations are highlighted in red ($^6Li + ^{12}C \rightarrow ^4He + ^{14}N$) and green ($^6Li + p \rightarrow ^4He + ^3He$). For the $^6Li + ^{12}C \rightarrow ^4He + ^{14}N$ reaction were used the point regarding the ground state and the first of the compound ^{18}F

and the various nuclides that can be found in the target. Indeed, other than the needed deuterium nuclei in the target there is a quite significant portion of carbons, being a CD_2 polymer, other than various impurities that can be trapped inside the target during the production process.

It is therefore necessary to identify at least one of the two detected particles. For this reason, the ΔE-E telescopes were used to identify in charge one of the two detected particles and subsequently select only those events in which a carbon nuclei hit one of the two available telescopes in coincidence with a detection of a particle from the PSD completing the symmetrical pair. Indeed it is known [52] from the Bethe-Bloch formula that the loss of energy per unit of space traveled by a particle in a material is proportional, for non-relativistic particles, to the mass of the particle, to the square of its charge and to the inverse of its energy, in formula:

$$\frac{dE}{dx} \propto \frac{mz^2}{E} \tag{4.8}$$

Therefore, by plotting the energy loss in the IC as a function of the total energy of the detected particles, obtained by completely stopping them in the detector, we will obtain a series of hyperbolas with the same curvature but separated along the ΔE axis of a value proportional to the charge and mass of the detected particle. However, as mentioned, the resolution of the ICs is not high enough to distinguish the particles by their mass.

In Figure 4.10 it is possible to see the aforementioned $\Delta E - E$ 2D spectrum. With a careful observation it is possible to identify two loci with an higher statistic of events, indicated in the figure by a red and a green arrow. We can identify the source of those events as it follows: first we select only one of these loci and plot, for the corresponding events, the angle of emission against the energy as measured by the PSD of the telescope. Then it is possible to compare this plot to various two body kinematical calculations involving the scattering of the beam and identify the correspondences. Fig. 4.11 shows the superimposition of these plots for the various loci into one picture.

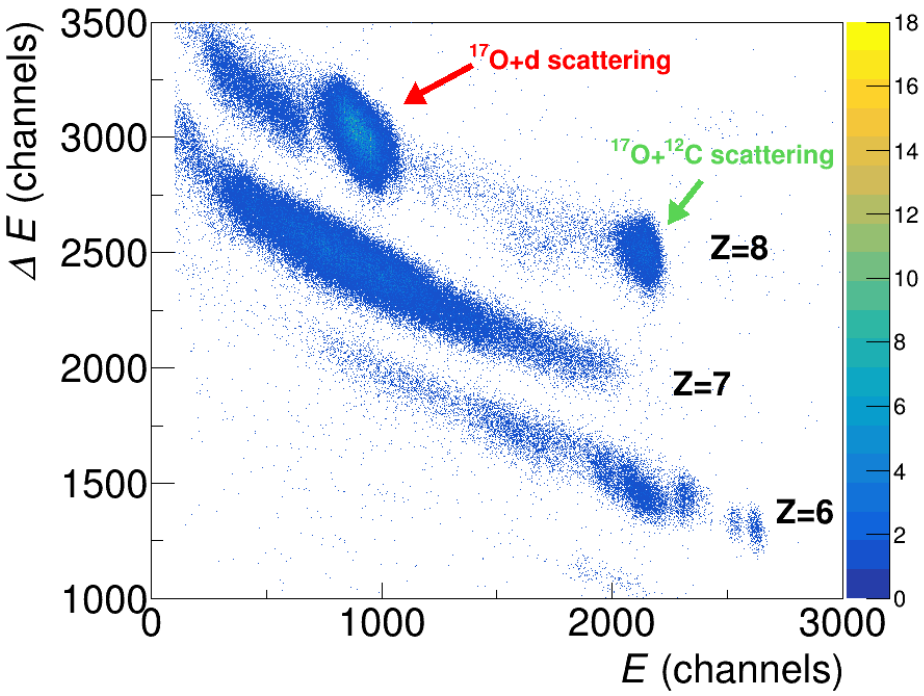

Figure 4.10: Scatter plot of the ΔE energy loss (in ADC channels) as a function of the total energy of the E particle (in ADC channels) as obtained by the telescope formed by the IC-B chamber and the PSD B1. The red arrow indicates the scattering of the beam off deuterium of the target, while the green one the scattering off carbon. The black labels indicate the inferred atomic number for each locus.

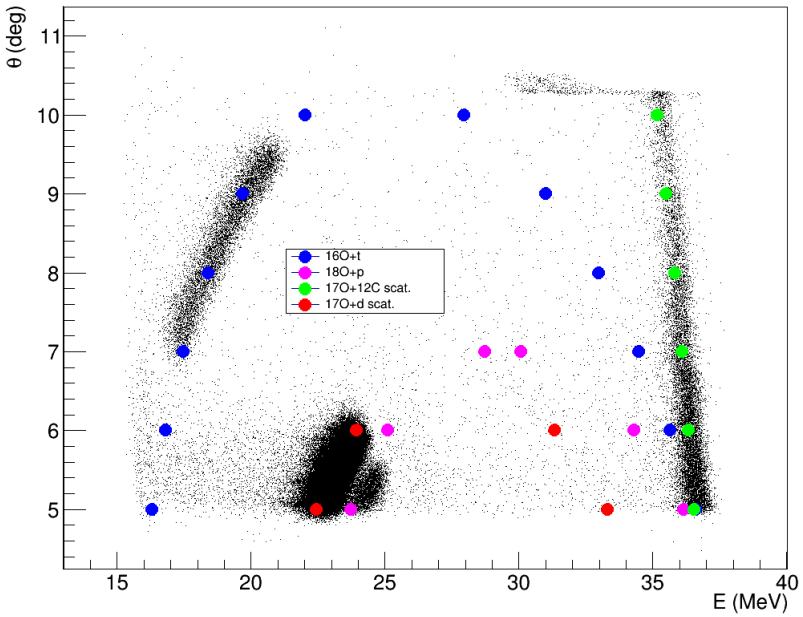

Figure 4.11: Angle of emission versus the energy of the particles detected in the PSD of the telescope for only the events selected as explained in the text.

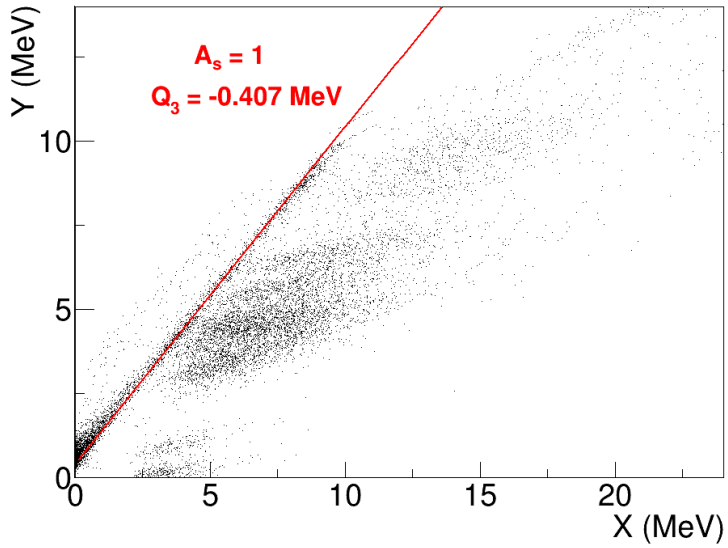

Figure 4.12: Scatter plot of the variables Y and X as defined in Ref. [53]. The red line is calculated for the expected values $A_s \sim 1$ and $Q_3 = -0.407 MeV$.

Therefore in Fig. 4.10 were also added two arrows to indicate these events: the red one refers to the scattering of the beam from the deuterium, while the green one refers to the scattering from the carbon nuclei. Consequently, it is possible to label each locus according to the atomic number Z, as indicated in the figure. In this way we are able to select only the events originating from the arrival of a carbon nucleus in the detectors A1 and B1. Then, assuming that the events measured in coincidence in the detectors A2 and B2 come from α particles and that the third particle is indeed a proton, using the energy and angle values measured by each pair of PSDs it is possible, as explained in the chapter on THM, to reconstruct all the kinematical quantities of the undetected proton.

It is possible to verify this assumption on the mass of the spectator by applying the method described in Ref. [53] which will be briefly reported in the following. By defining the variables

$$\begin{cases} Y = E_{beam} - E_{^{14}C} - E_{\alpha} \\ X = \frac{p_s^2}{2m} \end{cases} \tag{4.9}$$

where m is atomic mass unit, one can obtain the relation

$$Y = \frac{1}{A_s} X - Q_{val} \tag{4.10}$$

It should also be emphasized that the momentum of the spectator is defined regardless of its mass which appears only in the formulation of the kinetic energy as $p_s^2/2m_s$, which makes the use of the formula 4.10 valid to independently evaluate the mass of the spectator. In fact, drawing a scatter plot of the Y-X variables, the points should line up along a line whose angular coefficient depends exclusively on the mass number A_s of the spectator. As it can be seen in Fig. 4.12, the experimental values, indicated by the black dots, are distributed correctly around the value of the line calculated for the theoretical values $A_s \sim 1$ and $Q_{value} = -0.407 MeV$.

Subsequently the Q-value of the three-body reaction can be reconstructed from the energy conservation law as:

$$Q_3 = E_{^{14}C} + E_{\alpha} + E_p - E_{^{17}O} \tag{4.11}$$

and compared with the theoretical one for the reaction $^2H(^{17}O,\alpha^{14}C)p$, as it can be seen in Fig. 4.13, where the presence of a clear peak in correspondence to the theoretical value confirms that the events have been correctly selected and that the kinematical variables of the third particle have been adequately reconstructed.

Once only the events coming from the three-body reaction $^2H(^{17}O,\alpha^{14}C)p$ are selected, it is possible to verify the goodness of such selection using a series of tests developed alongside the THM. Indeed, in figure 4.14 a comparison has been made between the experimental kinematic loci, in red, and those obtained from the MC simulation, in black.

The four scatter plots refer to different cuts on the detection angle of the two particles, the first in the upper left includes the entire angular

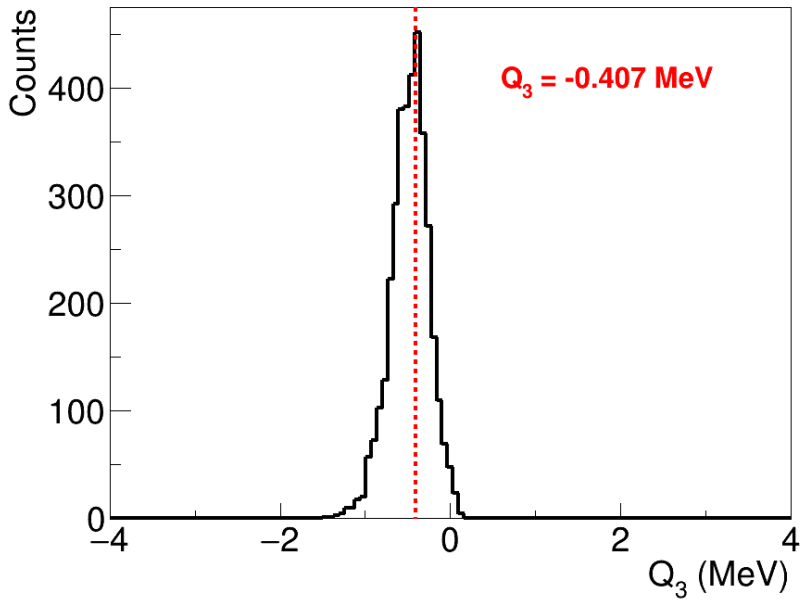

Figure 4.13: Reconstructed Q-value of the selected events. The red dashed line indicates the theoretical value for the Q-value of the three-body reaction $^2H(^{17}O,\alpha^{14}C)p$.

range covered by the detectors, while the other three refer to 2 degree cuts on each of the detectors repeated in various sections of the covered range. From the figure it can be seen how the experimental events correctly populate the region of the space $E_{^{14}C} - E_{\ alpha}$ indicated by the MC simulation. It must be noted that, since the simulation does not contain any experimental effects, the local density of these loci can be different, as visible in Fig. 4.14

What has been done so far is limited only to selecting the exit channel of the reaction, however the same channel can be populated via different reaction mechanisms, as it can be seen in Fig. 4.15.

For the application of the THM, however, as explained in the dedicated section we are interested only in the QF break-up events in which the deuteron, having passed the Coulomb field between ^{17}O nuclei and

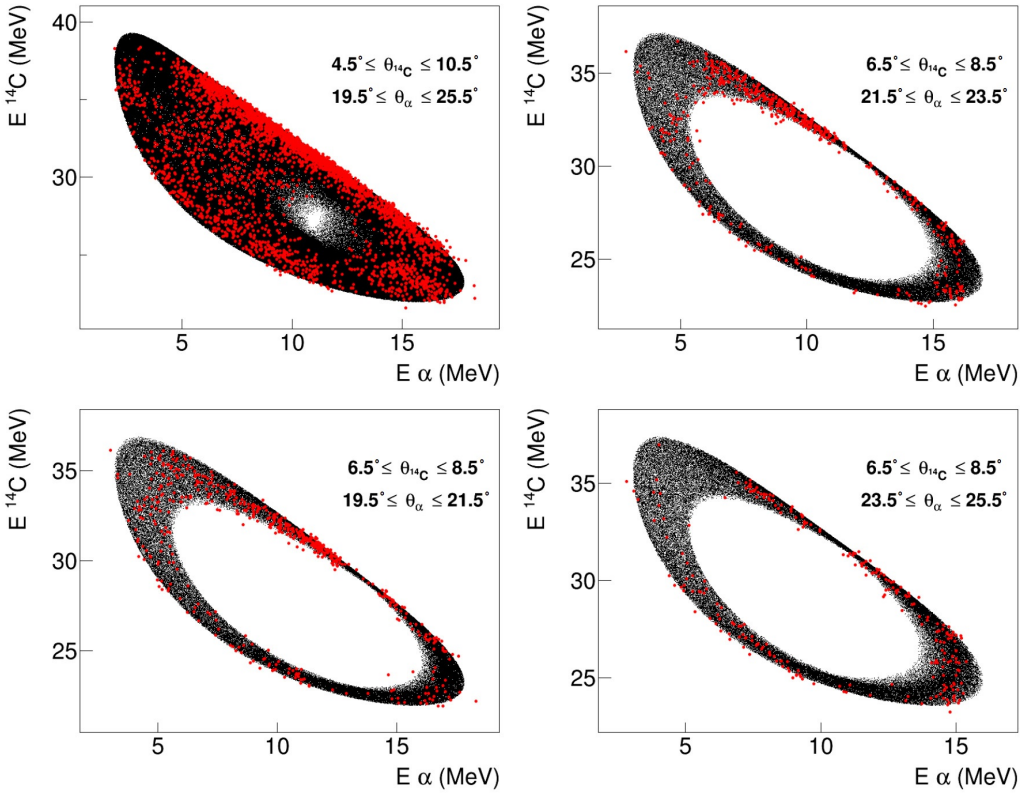

Figure 4.14: Kinematic locus for the $E_{^{14}C}$ and E_{α} variables. The dots in black represent the events obtained from MC simulation while the experimental data in red. The locus is defined with several cuts on the detection angles, shown in the labels.

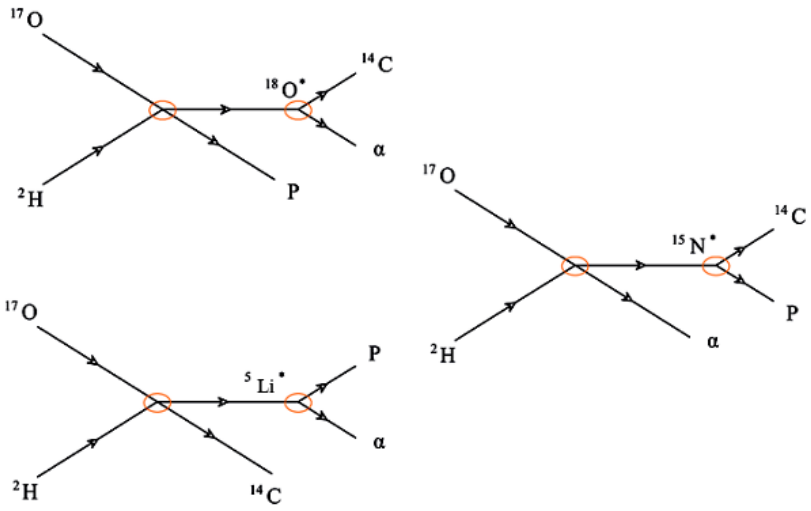

Figure 4.15: Pole diagrams of the possible reaction channels for the three body $^2H(^{17}O,\alpha^{14}C)p$ reaction.

itself, breaks under the effects of the nuclear field. After the QF break-up a virtual neutron is transferred to the oxygen with which it forms an excited intermediate $^{18}O^*$ system, which then decays into a ^{14}C nucleus and an α particle. Meanwhile, the residual proton from the break-up continues its motion undisturbed with the same momentum that it had inside the deuterium. To be sure to select only the events coming from this particular mechanism and therefore to discard all the events coming from other possible sequential reaction mechanisms, as seen in Fig. 4.15, it is necessary to check if there are correlations between the particles in the exit channel, i.e. if they come from the decay of an intermediate system. To this aim, the energies for the pairs $E_{^{14}C-\alpha}$, $E_{^{14}C-p}$ and $E_{\alpha-p}$ have been reconstructed. The presence or the absence of resonances in this plots would testify the formation or not of a excited state of an intermediate system of, respectively, ^{18}O, ^{15}N and ^{5}Li. Those three variables were plotted against each other in Fig. 4.16 and 4.17. There it is possible to see the presence of resonant structures only in relation to the $E_{^{14}C-\alpha}$

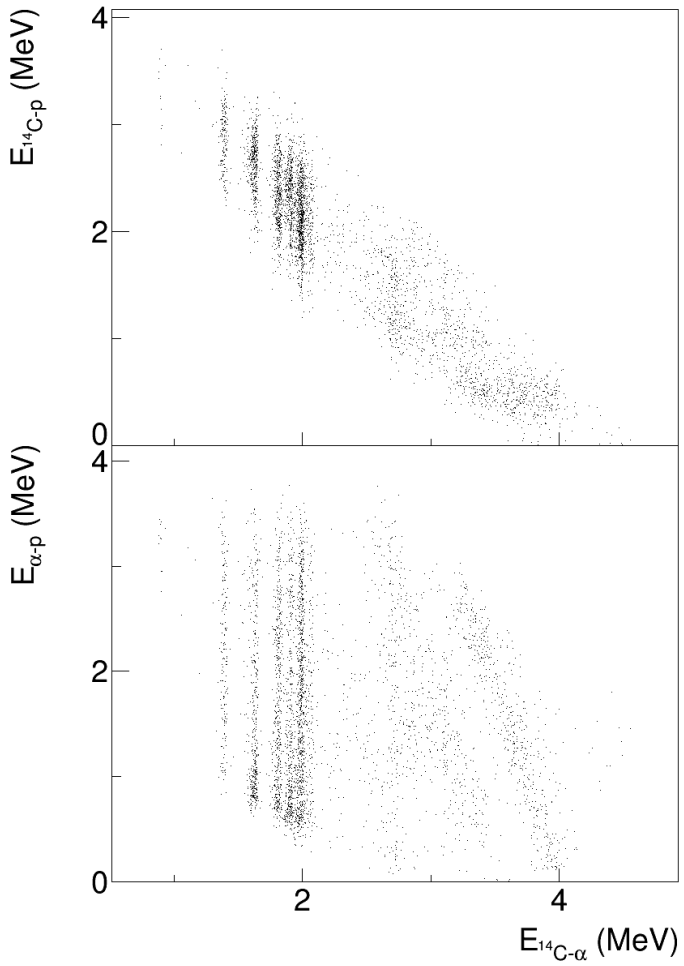

Figure 4.16: Scatter plot of the $E_{^{14}C-p}$ and $E_{\alpha-p}$ energy pairs versus the $E_{^{14}C-\alpha}$ energy.

energy and nothing for the other two energy pairs: this is a confirmation of the population of the desired reaction channel and, at the same time, of the absence of the other undesired sequential mechanisms. Moreover no correlation between the three energy pairs are present in the two plots.

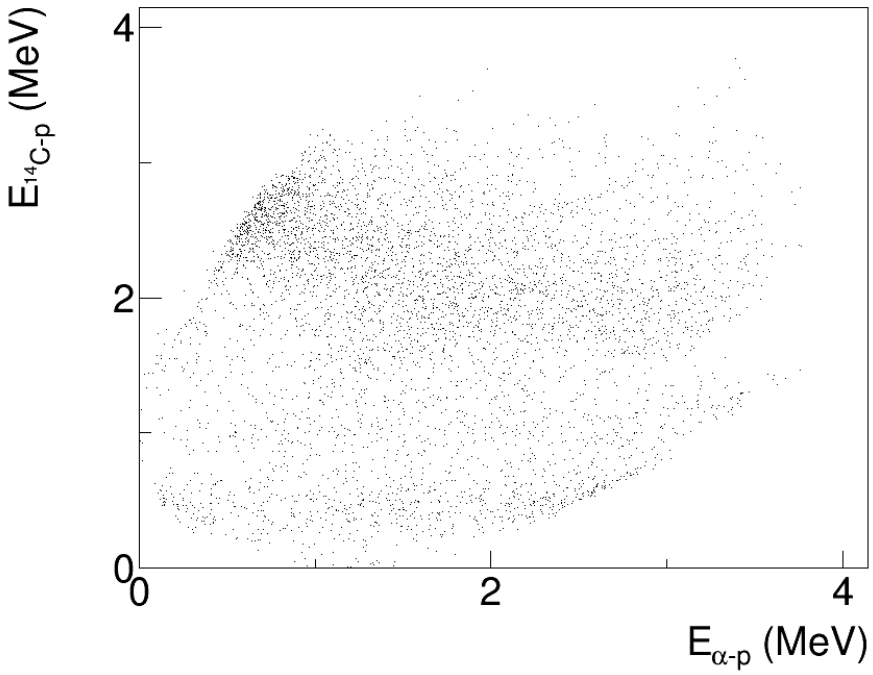

Figure 4.17: Scatter plot of the $E_{^{14}C-p}$ versus the $E_{\alpha-p}$. Vertical loci of experimental points are due to the population of an excited stated of the intermediate ^{18}O system.

4.2.5 Selection of the QF reaction mechanism

The QF break-up events can be then filtered out by analyzing the momentum distribution of the spectator. Indeed, by inverting the relation 3.6 it is possible to conclude that the momentum distribution is proportional to the ratio between the triple differential TH cross section, the kinematical factor and the two body cross-section. In formula:

$$|\Phi(p_s)|^2 \propto \frac{1}{K.F.} \frac{1}{d\sigma_{xA}^{b.n.}/d\Omega} \frac{d^3\sigma_{TH}}{d\Omega_b d\Omega_B dE_b} \tag{4.12}$$

From this last relation it is understood that it is possible to extract the momentum distribution, in arbitrary units, by simply dividing the experimental yield by the kinematic factor, taking care, however, to select

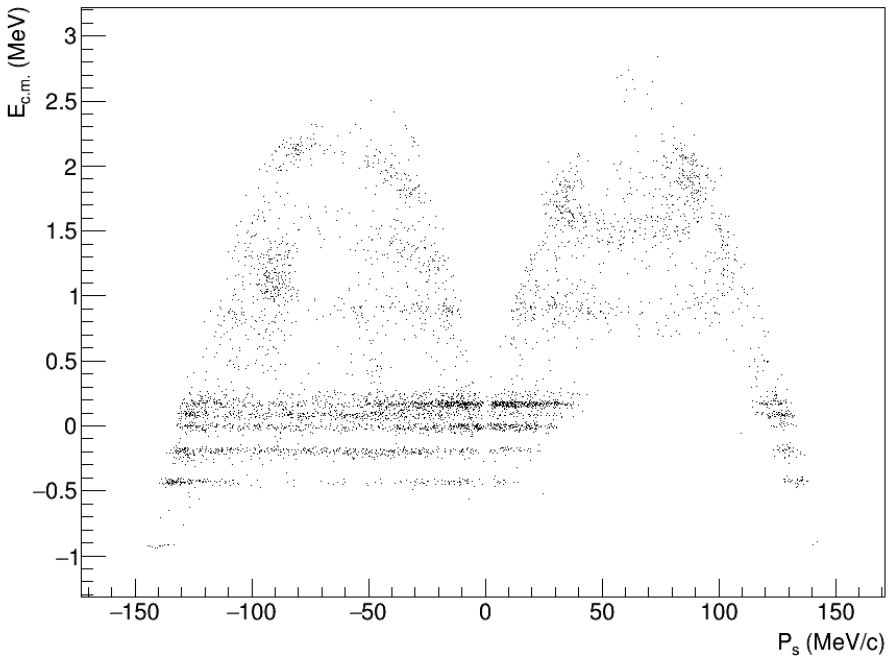

Figure 4.18: Scatter plot of the $E_{c.m.}$ versus the momentum of the spectator p_s .

a region in which the 2-body cross-section $d\sigma^N_{xA}/d\Omega$ can be considered constant. This can be achieved by limiting the selected data to a small energy region of the c.m. of the pair $^{14}C - p$, defined as :

$$E_{c.m.} = E_{^{14}C-\alpha} - Q_2 \tag{4.13}$$

where $Q_2 = 1.817$ MeV is the theoretical Q-value for the $^{17}O(n,\alpha)^{14}C$ two body reaction. By looking at Fig. 4.18, where the $E_{c.m.}$ is plotted against the momentum of the spectator p_s, it is possible to notice that the resonances detected do indeed populate the QF region around zero for the spectator momentum distribution. To study how these levels are populated with respect to the momentum of the spectator, the triple differential cross section $d^3\sigma_{TH}/d\Omega_b d\Omega_B dE_b$, which is proportional to the experimental coincidence yield, was divided for the *K.F.* and plotted in Fig. 4.19 as a function of $E_{c.m.}$, for different ranges of $|p_s|$: 0-20, 20-40, 40-60 MeV/c. If Eq. 4.12 is true we should see a decrease in the population of those resonances when the absolute value of the momentum of the spectator increase. This is precisely what is shown in Fig. 4.19 which then confirms that those resonances are indeed populated under the QF mechanism.

Therefore it is possible to go back on Eq. 4.12 and evaluate $|\Phi(p_s)|^2$ by taking only the events in a small energy region around the center of each one of the four resonances. The result of such calculation, when selecting only the events around the most populated resonance at $E_{c.m.} =$ 170.41 keV, is visible (black dots) in figure 4.20 where it is compared to the theoretical distribution (red line) given by Eq. 4.1.The good agreement between the experimental and theoretical distribution is an indication of the presence of the QF break-up reaction mechanism. Moreover, the full width at half maximum (FWHM) of the momentum distribution plotted in Fig. 4.20 was measured to be $FWHM = 57.34 \pm 4.05 MeV/c$: this value is in agreement with $FWHM \sim 60 MeV/c$ obtained [54, 48], under the PWIA hypothesis, for the wave function in asymptotic form. Moreover,

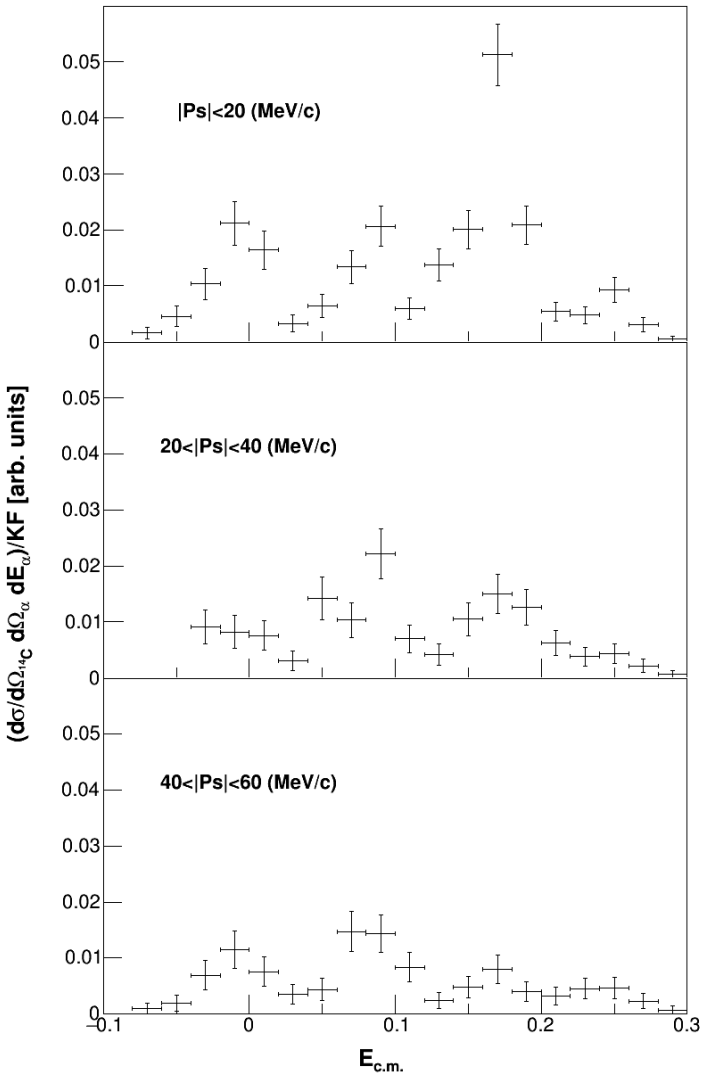

Figure 4.19: Triple differential cross section of the three-body reaction divided the kinematic factor as a function of $E_{c.m.}$, calculated for different ranges of the momentum of the spectator: 0-20 (top frame), 20-40 (middle frame), 40-60 (bottom frame) MeV/c.

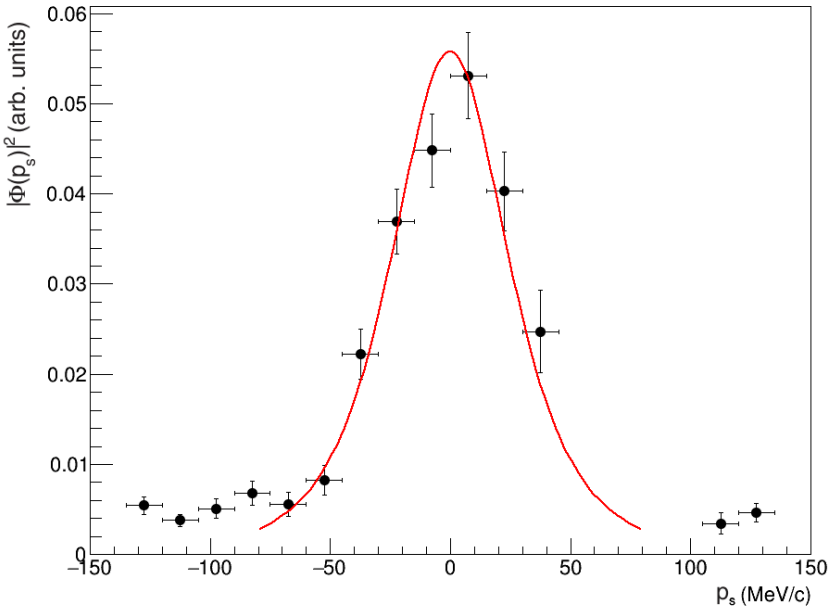

Figure 4.20: Momentum distribution of the spectator proton normalized on the kinematic factor with a narrow cut on the energy of the c.m. to select the third resonant peak. The theoretical momentum distribution is drawn in red.

by following the procedure described in Ref. [54], this value, as a function of the transferred momentum in the TH reaction q_t, was compared with the others obtained in past THM experiment also using the deuteron as TH nucleus. As it can be seen in figure 4.21 there is a good agreement between the value obtained here and the established data, confirming once more the goodness of the events selected.

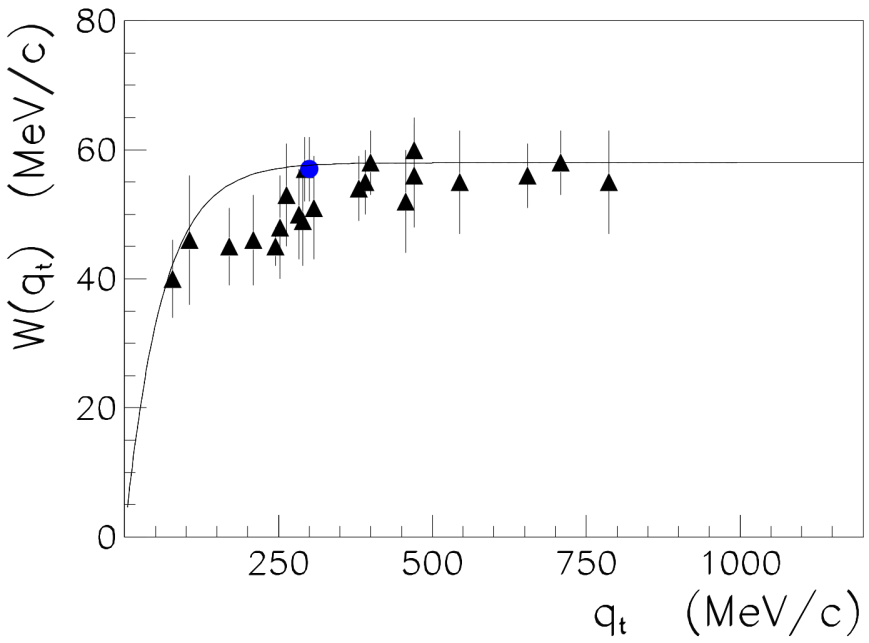

Figure 4.21: FWHM of the p-n inter-clusters momentum distribution inside the deuteron as function of the corresponding transferred momentum, as defined in Ref. [54]. Black triangles are referred to past THM experiments using the deuteron as TH nucleus, meanwhile the blue full circle refers to the present experiment.

4.2.6 Extraction of the two-body cross-section

Considering what was discussed in the previous section, to perform the analysis with only the QF events, a cut on the data given by the $|p_s| < 40$ MeV condition will be used.

Under the PWIA assumptions, it is possible to rearrange the formula in Eq. 3.6 as it follows:

$$\left(\frac{d^2\sigma^N_{xA}}{d\Omega dE_{c.m.}}\right)_{HOES} \propto \frac{1}{K.F.}\,\frac{1}{|\Phi(p_s)|^2}\,\frac{d^3\sigma_{TH}}{d\Omega_b d\Omega_B dE_b} \tag{4.14}$$

This means that we can extract the bare-nucleus cross-section for the $^{17}O(n,\alpha)^{14}C$ reaction by dividing the triple differential cross section, proportional to the experimental yield, by the product of the kinematical factor and the square of the momentum distribution $K.F. \times |\Phi(p_s)|^2$, obtained by the means of the devoted MC simulation.

In Fig. 4.22 it is possible to see the result of such analysis: the black dots represent the value of the experimental yield, divided by $K.F. \times |\Phi(p_s)|^2$, as a function of $E_{c.m.}$ meanwhile the red line represents the result of a fit performed using the sum of four Gaussian functions without taking into account any interference effect, since the resonance widths is much lower than their energy separation as discussed in Ref.[38]. The fit was executed to deconvoluted the weight of each resonance over the total reaction yield and to better identify the ^{18}O levels corresponding to the resonances. As found in previous experiments[44, 22], the excited states populating the experimental yield are the ones at $8.039MeV$ ($J^\pi = 1^-$), $8.125MeV$ ($J^\pi = 5^-$), $8.213MeV$ ($J^\pi = 2^+$) and at $8.282MeV$ ($J^\pi = 3^-$) which produce four resonances in the $^{17}O(n,\alpha)^{14}C$ cross section respectively at $-8.49keV$, $96.38keV$, $170.41keV$ and $241.24keV$ in $E_{c.m.}$. It must be noted that, thanks to the THM, it is possible to populate a sub-threshold resonance with quite good statistic and to properly detect the resonance at $96.38keV$, which is usually heavily hindered in direct experiments by the presence of the centrifugal barrier, due to the level being populated in

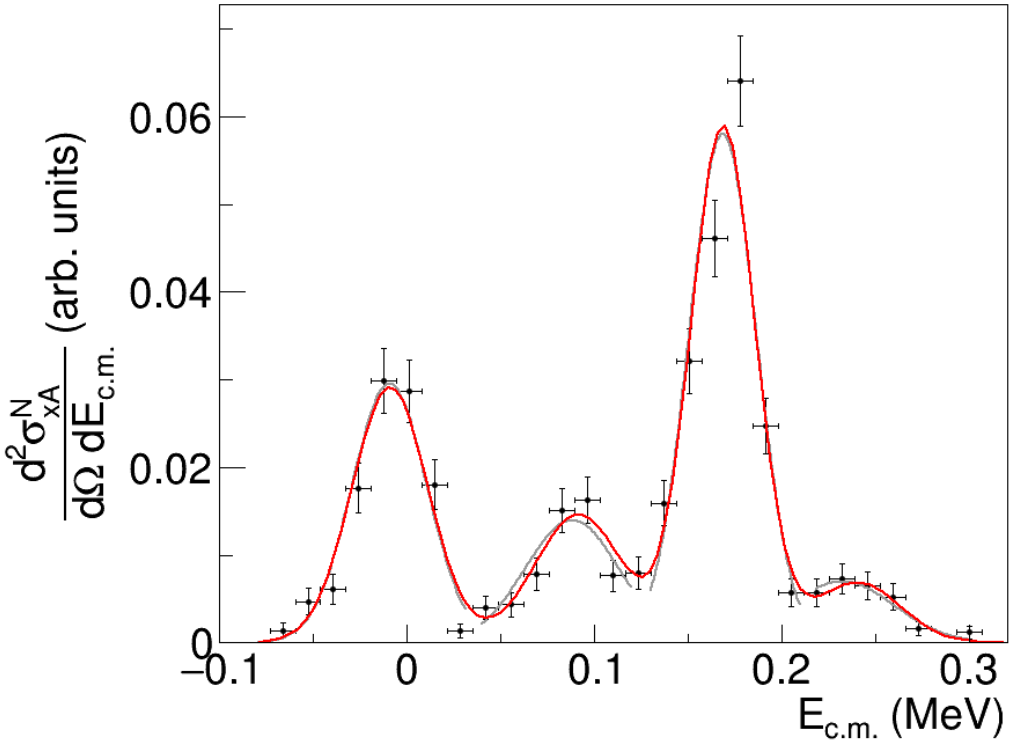

Figure 4.22: Bare nuclei cross-section for the 2-body reaction $^{17}O(n,\alpha)^{14}C$ as a function of $E_{c.m.}$. The red line is the result of a best-fit performed using the sum of four Gaussian functions, without taking into account any interference effect, meanwhile the gray lines are the results for the Gaussian fit of each resonance.

$E_{c.m.}$ (keV)	^{18}O (MeV)	J^{π}	ℓ_{in}
-8.49	8.039	1^-	1
96.38	8.125	5^-	3
170.41	8.213	2^+	0,2
241.24	8.282	3^-	1

Table 4.3: Spectroscopic parameters of the four detected resonances

d-wave, between the neutron and the ^{17}O nucleus in the entrance channel. A summary of each detected resonance is reported in table 4.2.6.

The data shown in Fig. 4.22 is limited to only a certain region of the full possible angular range of the $\theta_{c.m.}$ reaction angle, expressed in the c.m. of the $\alpha - ^{14}C$ system, which is defined as [55]:

$$\theta_{c.m.} = \cos^{-1} \frac{(\vec{v}_{^{17}O} - \vec{v}_n) \cdot (\vec{v}_{^{14}C} - \vec{v}_\alpha)}{|\vec{v}_{^{17}O} - \vec{v}_n| \, |\vec{v}_{^{14}C} - \vec{v}_\alpha|} \tag{4.15}$$

where $\vec{v}_i$ is the velocity for the particle i in the laboratory frame. The $\theta_{c.m.}$ range for the present experiment spans the interval between 60° and 120°, significantly increasing the range covered in comparison to the previous experiments. However, it is still necessary to integrate the angular distribution to obtain the total cross-section, thus taking into account the full angular range, between 0° and 180°. To do so it's necessary to first reconstruct the angular distribution $d\sigma/d\Omega$ as a function of $\cos\theta_{c.m.}$ for each one of the four resonance, isolated from the others by the means of the aforementioned Gaussian fit procedure. Then we must fit each angular distribution with the theoretical on-energy-shell angular distribution, calculated as explained in Ref. [44], leaving a scaling factor as the sole free parameter in the procedure, in order to correctly scale the already published distributions to the present experiment yield. The results obtained with this procedure are plotted in Fig. 4.23 where the red stars represent the present experiment data, the black dots the data by Gulino et al. [44] and the hollow squares the data by Guardo et al. [22], while the

black lines are the theoretical angular distributions calculated for each resonance with the given value of ℓ_{in} also reported in Table 4.2.6. The present experiment provided a higher statistics of the events collected, significantly lowering the statistical error in comparison to the two past experiments as it can be seen in Fig. 4.23, while still maintaining a broad coverage of the $\theta_{c.m.}$ range.

To take into account the $\theta_{c.m.}$ region not covered by the experimental data, a correction factor usually defined as [22]

$$\Xi = \frac{\int_{60^\circ}^{120^\circ} \frac{d\sigma}{d\Omega}(\cos\theta_{c.m.})d\theta}{\int_{0^\circ}^{180^\circ} \frac{d\sigma}{d\Omega}(\cos\theta_{c.m.})d\theta} \tag{4.16}$$

was calculated for each resonance and then used to properly scale the events related to that particular resonance, which were already deconvoluted with the procedure described before. Then all the data was summed over again finally obtaining the correct THM differential cross section as it can be seen in Fig. 4.24.

The data is still expressed in arbitrary unit since, as discussed in the third chapter of this thesis, the HOES nature of the cross section does not allow to measure it in an absolute scale and we need a trustworthy direct measurement to properly scale it. To do so, as it will be explained in the dedicated section, we need the partial widths of the resonances obtained by direct measurements. But, as we clearly saw, the data in literature do not agree well with each other: for this reason we decided to perform an independent and complete R-matrix analysis.

A review, using the R-matrix approach, does not add new information that is not already present in the data itself, it is only a way to better understand strengths and flaws of each datasets in order to obtain in the end a common "best fit" of the parameters we need and of the cross-section itself. Any issue in the data would be still there, only mitigated thanks to the information obtained from other sources and this is indeed one of the

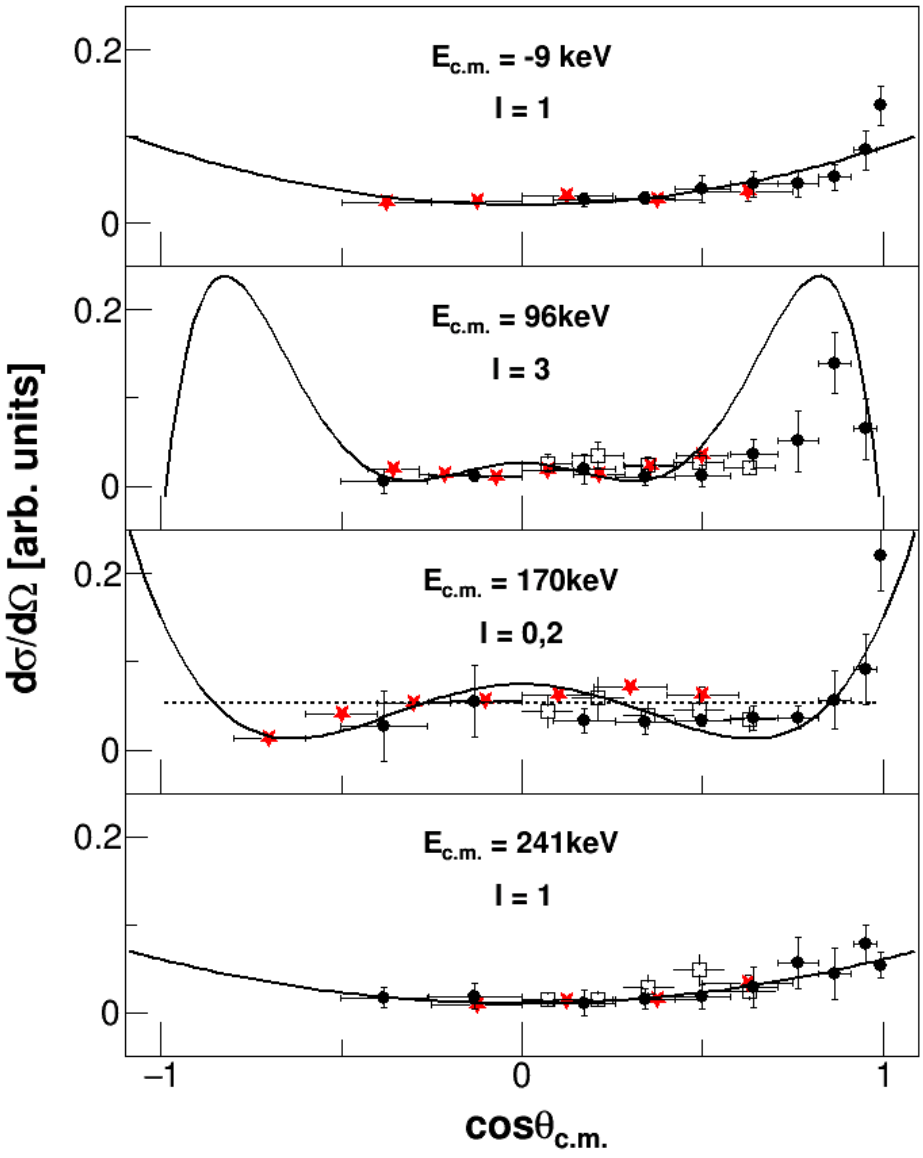

Figure 4.23: Differential cross section as a function of the $\cos\theta_{c.m.}$ for each of the detected resonances as obtained in the present work (red triangles), by Gulino et al. [44] (black dots) and Guardo et al. [22] (hollow squares).

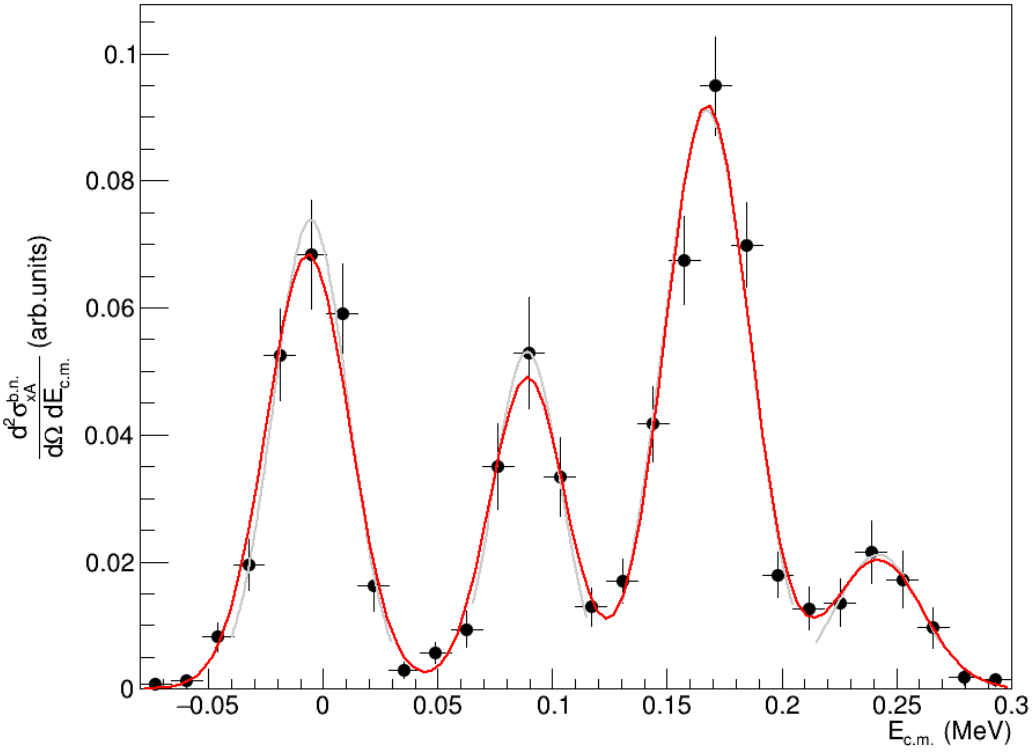

Figure 4.24: Bare-nucleus cross-section for the $^{17}O(n,\alpha)^{14}C$ reaction as a function of $E_{c.m.}$, after taking into account the correction for the $\theta_{c.m.}$ region not covered by the data, as explained in the text. The red line is the result of a best-fit performed using the sum of four Gaussian functions, without taking into account any interference effect, while the gray lines are the results for the Gaussian fit of each resonance.

most important aspect of the R-matrix approach: being able to use various independent measurement of different reactions that populate the same intermediate state in order to constrain the R-matrix with multiple sources of information. Moreover, even if there was a way to precisely know the exact value for the resonances detected in direct measurements we should remember that the THM allow us to also measure resonant states that are hindered or totally absent in direct data which are of fundamental importance to estimate the real value of the cross-section and the reaction rate in the stellar environment.

Therefore, it is clear that those two approaches are complementary and only by using the strengths of each one we would be actually able to study in the best way possible the reaction we are interested in.

4.3 R-matrix analysis of direct data in literature

4.3.1 Experimental data used

For a comprehensive R-matrix analysis of the $^{17}O(n,\alpha)^{14}C$ reaction ideally all available data at the energy range of interest, for all the reactions that populate an intermediate ^{18}O system, should be included. However, there are only a few datasets in literature for the astrophysical region, thus allowing us to include only data for the $^{17}O(n,\alpha)^{14}C$ and $^{14}C(\alpha,n)^{17}O$ reactions and the $^{14}C(\alpha,\alpha)^{14}C$ scattering: only these three channels were therefore activated in AZURE2. We already showed most of the data for the first two reactions in the direct data compilation from Guardo et al. [22] in Fig. 4.1 and we already know about their ambiguities. We decided therefore to use the data coming from the $^{14}C(\alpha,\alpha)^{14}C$ scattering measurement as a significant constraint to the Γ_α of the levels. However, we still need a reference to which normalize all the data: to this aim we used the value of the thermal neutron absorption cross-section for the $^{17}O(n,\alpha)^{14}C$ that was measured by Sears et al. [56] as 0.236 barns

at 0.025 eV of energy.

In order to perform the analysis, AZURE2 needs as an input also all the properties of the resonant levels of the intermediate ^{18}O system that are included in the energy region of interest. All the four resonant states already found in the THM analysis were included, using the tabulated values for their energy, J^π and partial widths as initialization values for the fit. As usual for an R-matrix analysis with AZURE2, a "background pole" was also added for each J^π of the levels included. A background pole is a fictitious level added to approximate the effects of all the other levels of the intermediate system that are not included in the analysis: for this reason these poles must be initialized in the code with a fixed energy significantly higher than the range we are studying. Moreover, a sub-threshold level was also included to reproduce the behavior of the cross-section at low energies and in particular the $E_r = 5.254 MeV$, $J^\pi = 2^+$ level of the ^{18}O was chosen in order to also take into account an interference effect with the $E_r = 8.213 MeV$, $J^\pi = 2^+$ that was noticed during the R-matrix analysis described below.

$^{14}C(\alpha,\alpha)^{14}C$ scattering: a constraint to the Γ_α

Looking over all the available datasets in literature for the $^{14}C(\alpha,\alpha)^{14}C$ scattering reaction, only two of them cover the energy range we are analyzing: the works from Avila et al. [57] and the one from Weinman and Silverstein [58]. The first one is significantly more recent than the latter, thus should have the advantage given by modern technology and techniques. Indeed, the data from Avila et al. are recorded in the EXFOR database, however the values indicated there do not match with the one published in the images of the paper. For this reason we decided to use a image digitization software to extract the data point for both works, thus in fact neutralizing the starting advantage Avila et al. works had. Avila et al. used the thick-target inverse kinematics technique to study the $^{14}C(\alpha,\alpha)^{14}C$ elastic scattering: a ^{14}C beam was accelerated at 42 MeV

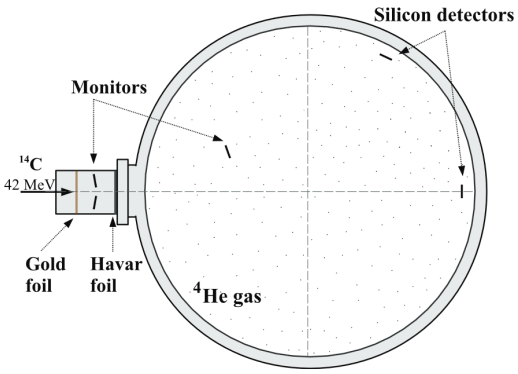

Figure 4.25: Part of the experimental setup used by Avila et al. [57]

by an FN Tandem Van de Graaff accelerator to a pure helium (99.9%) ^4He gas target. A sketch of the experimental setup used is visible in Fig. 4.25. In this technique, the pressure of the gas is tuned to completely stop the beam in the target thus, when a interaction indeed occurs, the ^4He hit by the beam gains kinetic energy and propagates forward where an array of detectors are set up to detect its position and energy, which is less hindered by the loss on the target having a charge and mass significantly lower than the one of the beam. However, this technique inevitably brings a degree of indeterminacy in the measurements, which means that the obtained cross-section is heavily influenced by those experimental effects, especially in the lowest part of the energy range measured which is exactly the range we are interested in. When the beam hits a nuclei of the target the exact point of interaction must be know to precisely reconstruct the energy of beam during the interaction: this is done by measuring with high precision not only the energy of the scattered nuclei but also its angle, however this approach suffers from the quality of the reconstruction. Indeed, as it can be seen in Fig. 4.26, the experimental effects are quite important and they cause a significant broadening of the resonance peaks. For this reason we decided to not use this data set to constrain the alpha partial width of the levels, we will use it after the fit

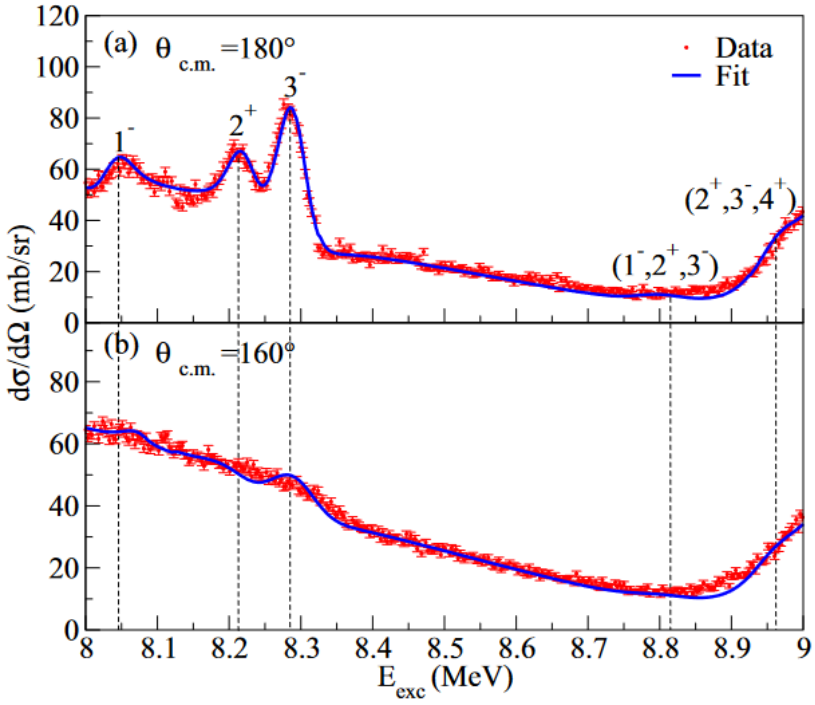

Figure 4.26: Scattering differential cross section (red points) and the relative R-matrix fit (blue curve) as reported by Ref. [57]

has been performed as a test to see if, considering all the experimental effects, we can reproduce their measurements. Weinman and Silverstein did their measurement in 1958 using an alpha beam accelerated from 2 to 4 MeV in the laboratory frame to a carbon target enriched of ^{14}C (38.6%), thus studying the excited states of ^{18}O in the energy range of 7.8 to 9.4 MeV, exactly where the resonances detected by THM data are located. They scattered ^{4}He ions were selected by an electrostatic analyzer to separate the ones scattered by ^{14}C nuclei in the target to those scattered by the ^{12}C ones, which make up the rest of the target (61.4%) and the whole backing. The experimental yield was measured at four fixed angles, $90^\circ, 125.3^\circ, 140.8^\circ$ and 149.5° which corresponds to zeros of Legendre polynomial for $\ell = 1, 2, 3, 4$, and at the back angle (169°).

The resulting differential cross section is reported here in Fig.4.27. As it can be clearly seen, the experimental effects on the cross section in this measurement are much less significant than the ones in the work from Avila et al., therefore we decided to use this data set to perform the R-matrix analysis. First the graphs in Fig. 4.27 were digitized, taking into account a 10% margin of error for the whole digitizing process which should be then combined with the error in the measurement declared by the authors and included in AZURE2 as a normalization error. Subsequently we performed an R-matrix fit of this data, treating each measurement at different angle as a separate *segment* in AZURE2, in order to verify that we are able to precisely reproduce the experimental effects. A segment is a unit of data that contains a series of experimental points referring the same measurement of the same quantity, i.e. integrated cross-section, differential cross-section, angular distribution, etc. . As we can see in Fig. 4.28, we indeed succeed in doing so. Therefore we packed all the data into one single segment in AZURE2 to have the same normalization coefficient, as it should be given that the measurements are coming from the same experiment, and proceed to add the $^{17}O(n,\alpha)^{14}C$ and $^{14}C(\alpha,n)^{17}O$ reactions datasets into the software.

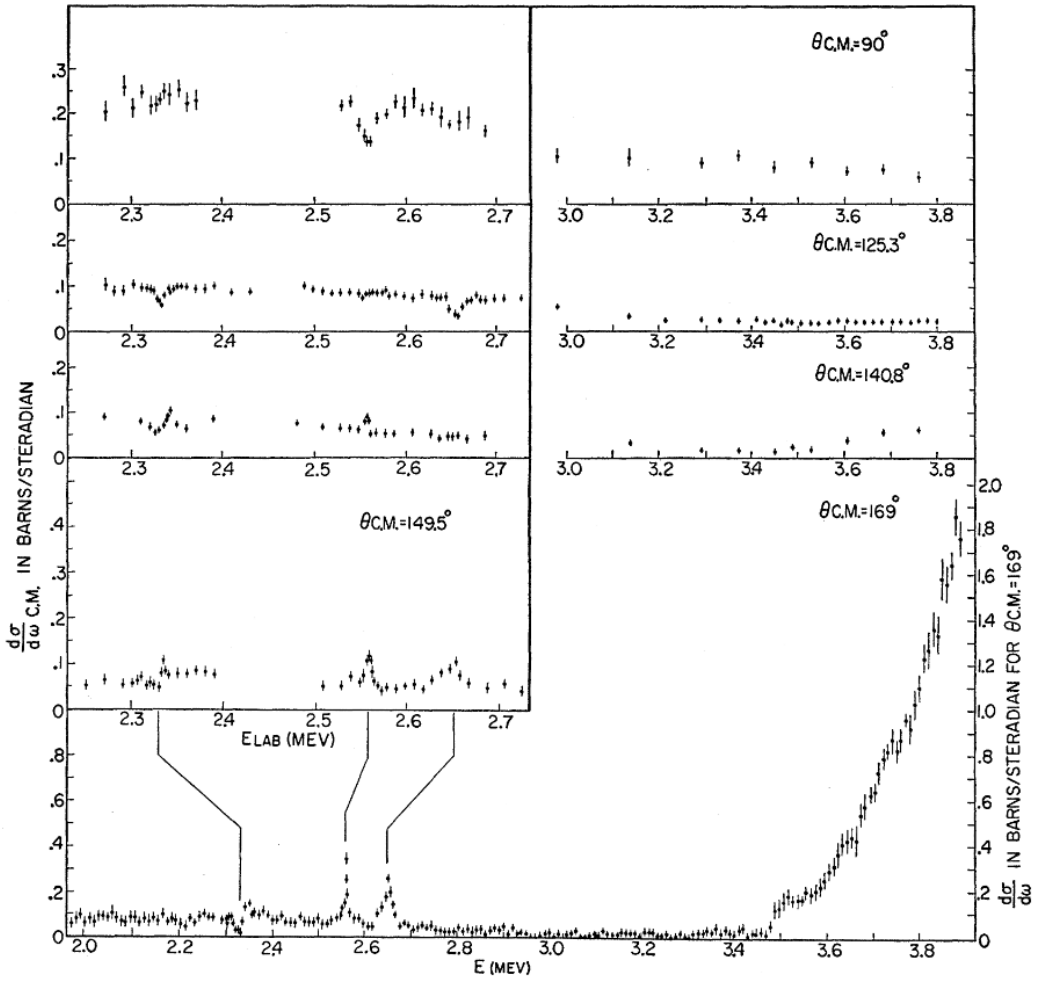

Figure 4.27: Scattering differential cross section as reported by Ref. [58]

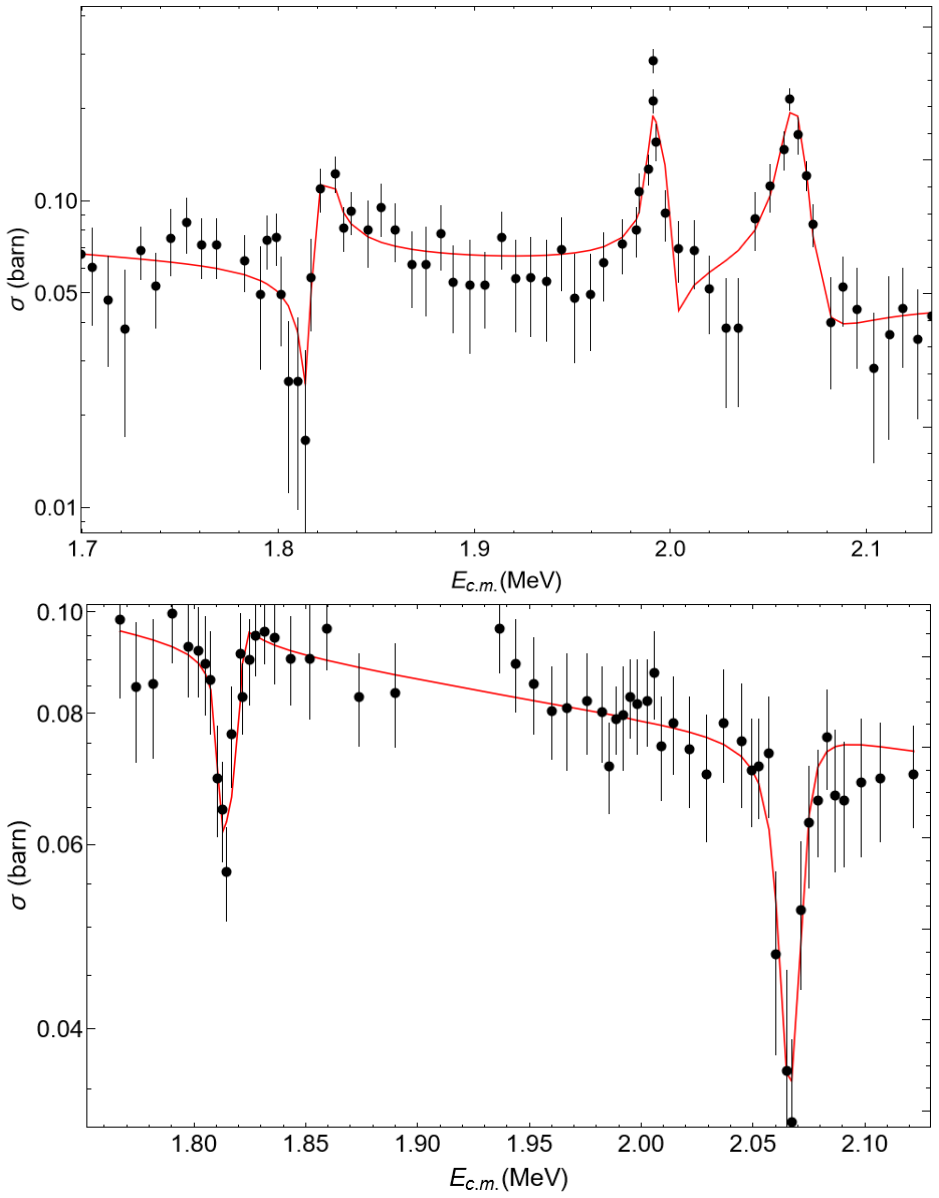

Figure 4.28: R-matrix fit (red curve) of the experimental differential cross section (black dots) from Ref. [58] for the 180° measurements (top) and 125° measurement (bottom)

$^{17}O(n,\alpha)^{14}C$ and $^{14}C(\alpha,n)^{17}O$ datasets

The data available in literature for the $^{17}O(n,\alpha)^{14}C$ reaction were already showed in the dedicated section of this chapter, therefore we will just briefly analyze each work in order to better understand how the experiment was carried out and how the data was acquired so that, in turn, we can better understand their data. For each one of them we would also carry out a standalone fit only considering the scattering data as a secondary source just to still maintain the constraint on the alpha partial width.

Koehler et al. [42] (Fig. 4.29) measured the $^{17}O(n,\alpha)^{14}C$ cross section from 1 MeV down to thermal energy range: this could be advantageous for our analysis since we could normalize this data to the thermal neutron absorption cross-section of 0.236 barn and use it as a reference for the normalization of other segments in AZURE2. The Koehler et al. measurement was carried out using a moderated white neutron source and a Nb_2O_5 target made by anodizing niobium in a ^{17}O enriched (37.5%) water. The energy of the neutrons was measured using the time-of-flight technique while the energy of the emitted alphas was measured by a $10\mu m$ thick silicon surface-barrier detector. As the authors themselves point out, due to the uncertainties in the neutron energy combined with the fact that they did not measured angular distributions and that they covered only a small portion of the solid angle, their data above $100keV$is not adequate enough to extract nuclear structure information. Considering this we decided to include in this analysis only the points below 100 keV. This means that we would not be able to use this data for getting information about the resonant levels above the threshold, however we can still get the significant advantage of precisely study the low energy region and use it as a reference for the normalization, as explained before. Indeed by looking at the value of the cross section measured by Koehler et al. at $0.025eV$ we can see a value very similar to the one mentioned above for thermal neutrons. We then multiply the data for a small correc-

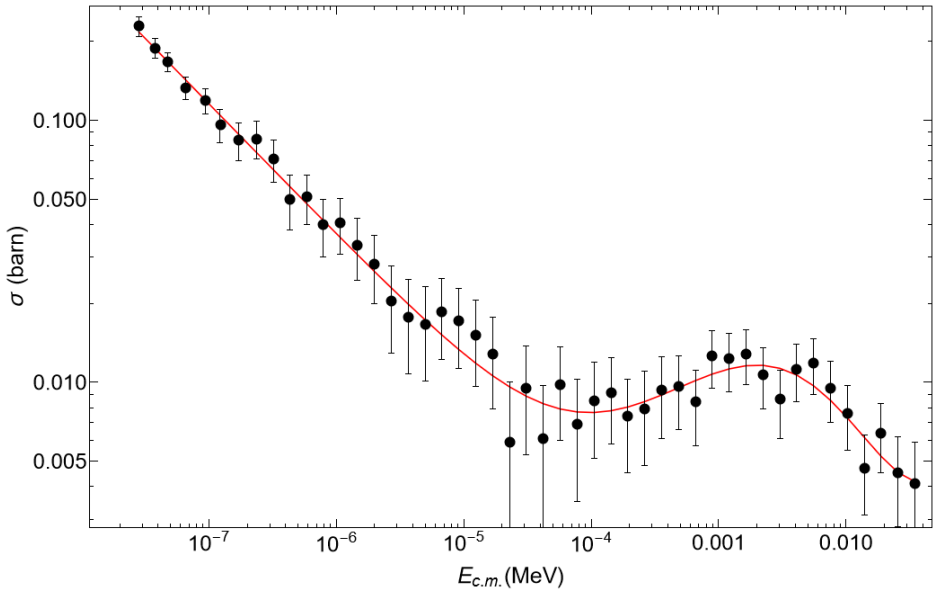

Figure 4.29: R-matrix fit (red curve) of the experimental cross section (black dots) from Ref. [42] taking also into account the scattering data from Ref. [58]

tion factor, of the order of 1%, an fix the normalization in AZURE2: the code will use this data as a reference from now on.

The data from Wagemans et al. [43] (Fig. 4.30) cover significantly better the energy region where the two resonances above threshold lay: we then must assess if we can reliably use it for our analysis. The measurement was carried out using a peculiar target, made by implanting ^{17}O ions in ultra-pure aluminum foils which in turn resulted, as the authors underline, in an higher density of ^{17}O in the final target with respect to the target used by Koehler et al. . The neutron beam was created using a primary proton beam from a Linac, therefore also in this case the time-of-flight technique was used to measure the energy of the neutrons, meanwhile the energy and angle of the alpha particles were measured using a ionization chamber equipped with a Frisch grid. Without going too much into the experimental details of the measurement, we clearly saw

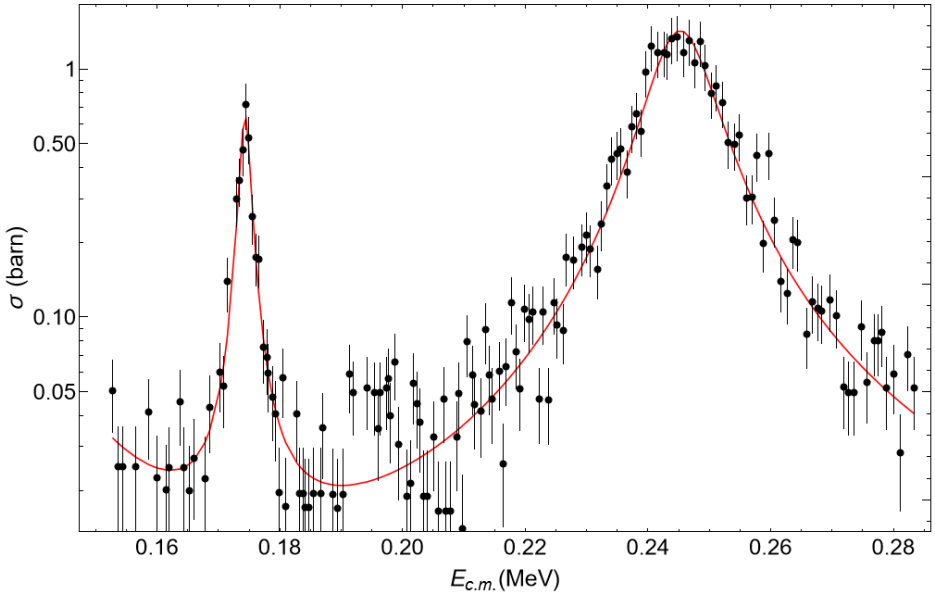

Figure 4.30: R-matrix fit (red curve) of the experimental cross section (black dots) from Ref. [43] taking also into account the scattering data from Ref. [58]

at the beginning of this chapter, in Fig. 4.1, that the energy resolution is good enough to asses the presence of two separate resonant structures in the cross section. Wagemans et al. also carried out the measurement at thermal energies as Koehler et al. did, however the plot in which they show this data suggest a value for the cross-section three orders of magnitude lower than the one from Koehler et al. which we already assessed as reliable, by comparing it to the thermal neutrons value of 0.236 barn. Unfortunately, unlike the data from Koehler et al., the cross section from Wagemans et al. is not available on EXFOR so we have no way to verify the reliability of this low energy part: therefore, we have no choice other than excluding this part of the data from our analysis.

Moreover, both Wagemans et al. and Koehler et al. gave an evaluation of the reaction rate which is quite similar in the overall shape but it is scaled differently by a multiplying factor with a value of ~ 3 [43]. This

could be explained by a difference in the normalization of the data, however, using the neutron thermal energy we already apply a constraint in this sense to the data from Koehler et al., even if it was just only one point at low energy. In any case, for the R-matrix analysis it is beneficial to have as many measurements as possible covering the same energy region. We therefore added to the analysis the data from Bair et al.[59] (Fig. 4.31) of the inverse reaction $^{14}C(\alpha,n)^{17}O$ obtained using an alpha particle beam of energies between 2.5 and $5.1MeV$ in the laboratory frame, which correspond to an excitation energy of the ^{18}O intermediate system between 8 and $10MeV$ thus covering the region where there are the two resonant levels we are interested in. The experiment was carried out using a Van de Graaff accelerator for the alpha beam, impinging on a target produced from ^{14}C-enriched acetylene and with a thickness of $17keV$. The produced neutrons were measured with a spherical graphite detector, more information can be found in Ref. [59] and references therein.

Finally we also took into exam the data from Schatz et al. [8]: even thought there are only five points with a quite large energy resolution they are still useful to link the low energy region covered by Koehler et al. with the region above $100keV$ covered by Wagemans et al. and Bair et al. with their data.

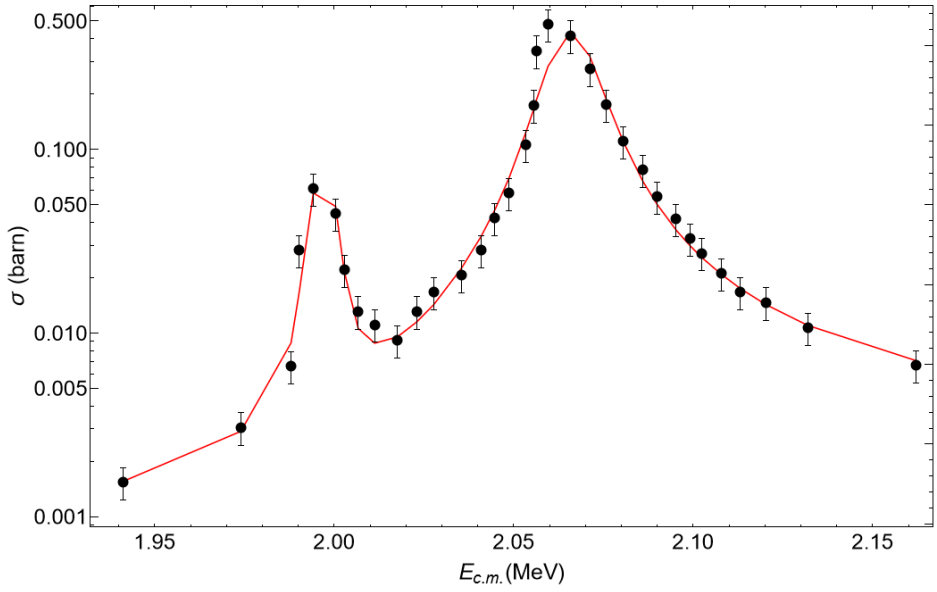

Figure 4.31: R-matrix fit (red curve) of the experimental cross section (black dots) from Ref. [59] taking also into account the scattering data from Ref. [58]

4.3.2 Reproducing experimental effects in the data

Before proceeding with the concurrent fit of all the data we must first evaluate if the fit of each segment needs further tuning by including the experimental effects affecting the data, using the dedicated section in the AZURE2 code, in order to correctly reproduce the shape of the cross section as measured by the various authors. The user can take advantage of target integration and beam resolution convolution techniques implemented in the code.

The beam resolution convolution function is used to better reproduce the effect on the cross section from the finite energy resolution of the detection system and the finite thickness of the target used. Often the distortion of the cross section by these experimental effects can be simulated by convoluting the R-matrix cross section with a Gaussian function which is energy independent, considering that these effects are also usually energy independent. The target integration function is used instead to evaluate the energy loss of the beam as it interacts with the target. Therefore, AZURE2 calculates the final simulated spectrum as [60]:

$$F(E_0) = \int_{E_0-\Delta}^{E_0} \int_{E=-\infty}^{+\infty} \frac{\sigma(E')}{\epsilon(E')} g(E - E_0) dE' dE \tag{4.17}$$

where E_0 is the mean beam energy, $\sigma(E')$ is the cross section devoid of any experimental effect, $\epsilon(E')$ is the stopping cross section, which represents the energy distribution resulting from the scattering process of the beam particles inside the target, $g(E - E_0)$ is the spreading function, which represents the energy distribution of the beam[60]. To correct for these effects the user can perform basic target integration corrections by adding in the code the density of the active target material, i.e. the density of the nuclei in the target actually involved in the reactions of interest, alongside the total *stopping* cross section, considering all the materials in the target. The latter must be declared as a continuous function of energy so that the effected can be determined at any arbitrary energy.

In most of the segments in exam the effect can be actually neglected but in two cases we were forced to include the target thickness effects to perform a valid fit: for the scattering data from Weinman et al. and for the data of Bair et al. . In both cases, the active target value was inferred from the data reported on the paper, meanwhile the stopping cross section was determined by fitting the values obtained by performing a SRIM [61] calculation reproducing the actual experimental conditions for each case. All the fit showed in the previous paragraphs in figures 4.28,4.29,4.30 and 4.31 are already obtained with these experimental effects turned on.

4.3.3 Assessing the normalization factor

With all the data set up inside the AZURE2 code we first initialize the values for the parameters of the ^{18}O resonant levels with the one present in the literature and then perform the first of a series of fits: we are not sure if we are actually near the point of absolute minimum in the parameters space for the χ^2 function, used by the minimization algorithm to perform the fit, therefore there could be some issues with the calculation, such as the algorithm getting stuck on a local minimum or taking too much time due to the experimental effects integration. By repeating the calculation with small changes in the initialization values of the parameters we can test the stability of the fit by looking at how the final values change. First we focus on the normalization parameter, i.e. a multiplying constant for each data set, and we start by giving to all the segments a value of 1, indicating also for each of the the error in the normalization of the data, which in most of the cases was already mentioned in the original paper while in some cases we had to extrapolate it from other values reported by the authors. After repeating the fit for multiple runs, if the results were stable, we took the values obtained in the last 10 runs and calculate the average of the values obtained for each parameter which are reported in Table 4.3.3.

The normalization of Koehler is obviously fixed because, as mentioned

Source Data	Normalization factor
Koehler et al. [42]	1 (fixed)
Weinman et al. [58]	0.927 ± 0.01
Bair et al. [59]	1.411 ± 0.05
Schatz et al. [8]	1.763 ± 0.05
Wagemans et al. [43]	3.266 ± 0.1

Table 4.4: Normalization factor obtained for each of the direct measurement data included in the R-matrix analysis.

before, we already found to be in accordance with the thermal neutrons energy value. All the remaining datasets, except the one for Wagemans et al. data have a normalization factor of about 1. For the scattering data we put the measurements at various angles in a single AZURE2 segment in order to have a common value for the normalization, since all the data comes from the exact same experimental setup, and we indeed get a factor close to one which confirms the goodness of the data. The value for Wagemans et al. of about 3.3, having fixed the data of Koehler et al. to the thermal neutrons value, also confirms the scaling difference we already mentioned. The remaining values for Bair et al. and Schatz et al. are slightly higher than 1 because the code tries to increase them to match the data of Wagemans et al. . The errors for the normalization factors are a first gross estimate obtained by considering the excursion of each value along all the multiple runs of the code used to calculate the mean value. However, this estimation is of course not adequate for our purpose. A more strict error evaluation of all the fit parameters will be given in a dedicated section in the following.

4.3.4 Fitting the partial widths of the levels

Finally, once we have defined a stable set of values for the normalization factors, we use them as an input in the code and we repeat the fit again

R-matrix fit (this work)

E^*_{18O} (MeV)	J^π	Γ_n (eV)	Γ_α (eV)	Γ_{tot} (eV)
8.038	1^-	170 (rw)	1901.5	1950
8.218	2^+	257.7	2003.9	2262
8.289	3^-	9501.6	3492.8	12994

Table 4.5: Partial and total widths for the resonances in the energy region of interest included in the R-matrix analysis. For the 1- resonance the neutron partial width is substituted with the reduced width (rw) due to the sub-threshold nature of the channel.

for multiple runs, still giving the code the possibility to vary them, while performing small adjustment to the initial values of the strength of the resonances or to the ANC, in the case of sub-threshold ones. The details of the fit procedure are described in details in the AZURE2 User manual [60]. In Table 4.3.4 there are reported the values for the partial widths and the total width of each detected resonant levels obtained by calculating the average on multiple runs.

We can then compare the results for the total widths with the ones available in the literature. In particular we took into exam the tabulated values in Wagemans et al., since it is the most recent and the one with the lowest relative error, those from Guardo et al., obtained via the application of the THM, and those given by Avila et al., because it could be an interesting comparison to do as a cross-check since their data was not included in this fit.

As we can see from Table 4.3.4, except for the resonance with the highest energy in the work of Avila et al. , all the values obtained from the R-matrix fit for the total width are in line with the data available in literature, coming both from direct and indirect (THM) measurements. We will not focus on comparing the partial widths for multiple reasons. First the values obtained by the various references come from totally different experimental approaches that are sensible to different channels. Indeed,

		Γ_{tot} (eV)			
E^*_{18O} (MeV)	J^π	R-matrix fit	Wagemans	Avila	Guardo
8.038	1^-	1950	2400	2000 ± 700	2400 ± 300
8.218	2^+	2262	2258 ± 135	1900 ± 200	2260 ± 300
8.289	3^-	12994	14739 ± 590	8500 ± 900	14700 ± 3800

Table 4.6: Comparison the values obtained for the total strength of the resonances of interest by this R-matrix analysis and by Ref. [43, 57, 22]

Avila et al., which obtained significantly different values for the partial widths with respect to the ones obtained by Wagemans et al., verified [57] that when they used the partial widths from Wagemans et al. in their R-matrix analysis the $^{14}C(\alpha, n)$ spectrum was still well reproduced while the $^{14}C(\alpha, \alpha)$ was not. Moreover, Wagemans et al. fitted their data with non-interfering Breit-Wigner shapes using the total level widths, the reduced neutron widths and the statistical spin factor g. The alpha partial widths were then calculated using the tabulated values for the gamma partial widths. Meanwhile Avila et al. obtained the partial widths by the means of an R-matrix fit of their scattering data combined with various other datasets to constrain the other open channels. Therefore the best approach is to just consider the actual experimental data and perform an independent R-matrix fit, as we did.

4.3.5 Error evaluation using *emcee* and BRICK

As we have seen so far, no errors were showed for the output values of the fit parameters obtained from AZURE2. This, as explained in the devoted section of the previous chapter, is the standard behavior of the code that simply uses MINUIT2 to perform the minimization but does not calculate any estimation of the error of the parameters. As said, we have to use *emcee* alongside BRICK to link the MCMC analysis procedure with AZURE2. For the starting values of the Markov chain, BRICK

will automatically read the AZURE2 workspace files and obtain the input values given by the user for the parameters and then use them to generate slightly different starting points for each of the walker, as explained before. Considering that, in the Bayesian formalism, the priors PDFs represent our *a priori beliefs* on the parameters, i.e. what it is known before the experimental data is considered, it is a good practice to start to sample a small region of the parameters space around the most likely value, which we already obtained through the AZURE2 fit, and then expand this region as much as possible giving as little bias as possible to the prior PDFs. In the final iteration of the input model, which we will show here in this paragraph, the prior PDFs of the R-matrix parameters are defined as a flat distribution with a quite large range, calculated as $x \pm x$ where x is the starting value of the parameter, except for the energy of the resonances that are defined in a small region, of about $0.05 MeV$, since these values are already well known.

The final posterior PDFs obtained from the MCMC analysis can be plotted using the *corner* python package, precisely developed to graphically represent this type of data, since it indeed create a corner plot where the diagonal is populated by the one dimension posterior distributions of the parameter. The i, j $(i \neq j)$ non-diagonal slots will be then populated by the 2D plot of the corresponding i, j parameters. However considering the large number of parameters involved in this calculation, the final dimension of the corner plot would be too large for the A4 paper of this work. Instead, we will show here only small section of it that are of particular interest for our analysis.

In Fig. 4.32 it is possible to see the a small section of the corner plot obtained, where n_1, n_3, n_7 , n_9 are respectively the normalization factor for the data of Wagemans et al., Schatz et al., Bair et al. and Weinman et al. . Here it is possible to clearly see that there is a correlation between n_1, n_3 and n_7: this means that the high value we obtain for the normalization of Schatz et al., Bair et al. are influenced by the need of having an high

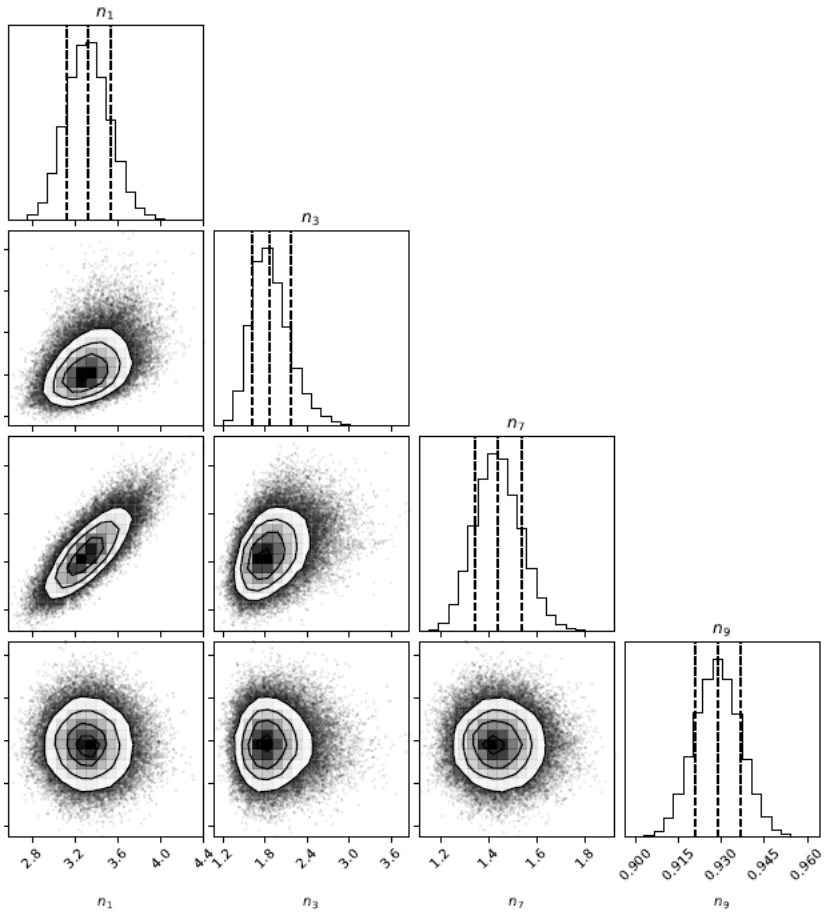

Figure 4.32: Part of the corner plot of the R-matrix parameters calculated in the MCMC analysis, focusing only on the normalization factors of the datasets

Source Data	Var. name	Value (MCMC))
Koehler et al. [42]	n.a.	1 (fixed)
Wagemans et al. [43]	n_1	3.3 ± 0.2
Schatz et al. [8]	n_3	1.9 ± 0.3
Bair et al. [59]	n_7	1.4 ± 0.1
Weinman et al. [58]	n_9	0.928 ± 0.008

Table 4.7: Normalization factors and their confidence interval obtained by the MCMC calculation for each of the direct measurement data included in the analysis.

scaling factor for the data of Wagemans et al. . In Table 4.3.5 it is possible to see the values obtained for these parameters from the MCMC, calculated as the 50th percentile of the posterior distribution, alongside the 1σ confidence interval obtained by evaluating the 16th and 84th percentile.

Moreover by leveraging the functions of BRICK, it is possible to plot the MCMC R-matrix calculation for the cross section, including again the confidence interval. This is done evaluating the R-matrix at multiple energy values and for each one of them repeating the calculation for each of the values of the posterior distribution of the parameters. While it may sound complicated this simply means that instead of having one cross section value for each energy we will now have a cross section distribution, an example of which can be seen in Fig. 4.33. Finally in Fig. 4.34 we can see the $^{17}O(n,\alpha)^{14}C$ cross section and its confidence interval as obtained by the MCMC calculation (orange line) plotted along with the data from Ref. [43] (blue points) and [42] (green points). Here the cross section is unfortunately cut at a lower limit of 10^{-5} MeV since, going to a limit closer to zero would require a significantly smaller sampling step in that range and a much longer computational time. We can however see that the MCMC cross section nicely reproduces the experimental data trend but for the data of Wagemans et al. there is of course a normalization factor of about 3 to take into account.

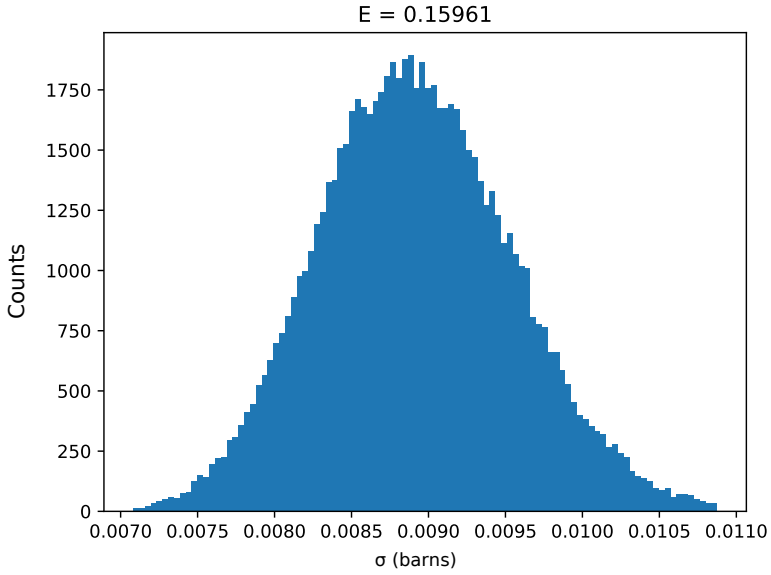

Figure 4.33: MCMC evaluation for the cross-section distribution at the energy value of 159.61 keV

MCMC calculation

$E^*_{^{18}O}$ **(MeV)**	J^π	Γ_n **(eV)**	Γ_α **(eV)**	Γ_{tot} **(eV)**
$8.0380 \pm 4e{-}04$	1^-	200 ± 20 (rw)	1880 ± 210	2080 ± 310
$8.2184 \pm 1e{-}04$	2^+	260 ± 20	2000 ± 100	2260 ± 120
$8.2891 \pm 2e{-}04$	3^-	9570 ± 450	3530 ± 200	13100 ± 650

Table 4.8: Spectroscopic parameters obtained by the means of the MCMC calculation for the resonances included in the analysis.

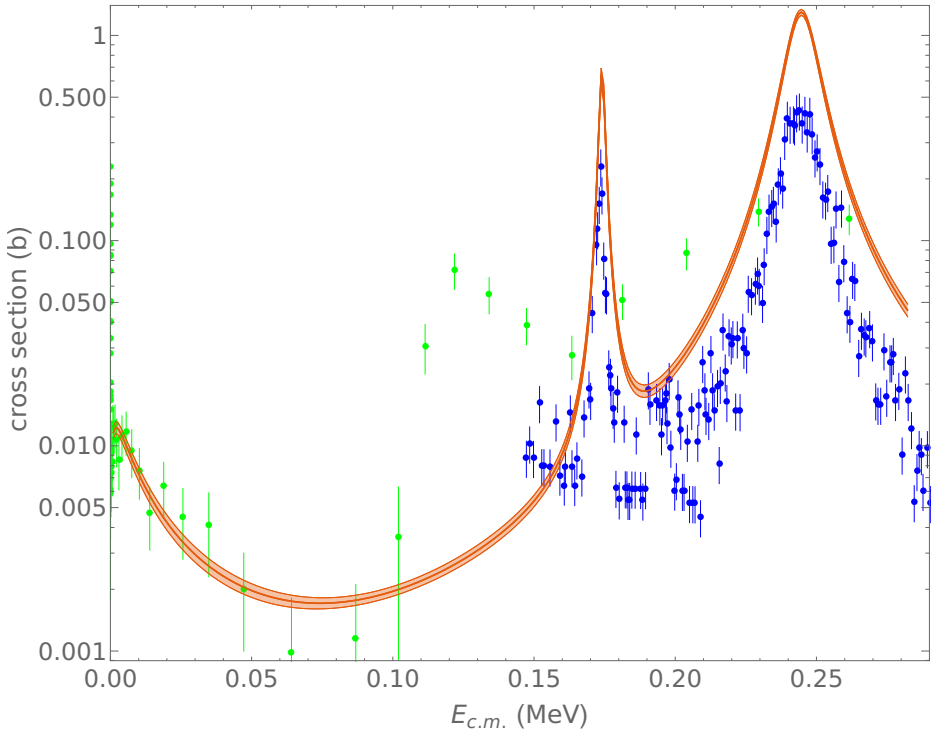

Figure 4.34: Cross section and its confidence interval as obtained by the MCMC calculation (orange line) plotted along the data from Ref. [43] (blue points) and [42] (green points)

Meanwhile in Table 4.3.5 we can see the values obtained by the MCMC R-matrix calculation for the strength of the resonances. The total widths are, considering the experimental errors calculated as explained before, in accordance with the values available in the literature. However, for the neutron partial widths we get values consistently higher than the ones obtained by Wagemans et al. : this could be explained by the aforementioned normalization factor in the data of Wagemans et al. that is also clearly visible in Fig. 4.34. On the other hand, the alpha partial widths are instead lower than to the ones showed by the authors in their work[43] and more in line to what Avila et al. report in their work. This behavior should require further investigation since, as already mentioned, the data set is not present on EXFOR or any other database and there might be only an issue in the plotted data. Another explanation could be that the authors are aware of some experimental effects or correction that we are obviously missing in our analysis. The same relation holds true when comparing the result in Table 4.3.5 to what Guardo et al. reported in their work, this comparison will be however discussed in depth in the following section when taking into account also our THM data.

We can then conclude that the analysis procedure was correctly carried out and we can use the obtained values for the reduced widths, present in the output file created by AZURE2, to perform our modified R-matrix analysis as it will explained in the dedicated section below.

4.4 Modified R-matrix analysis of THM data

With the THM cross-section correctly extracted, as shown before, it is then possible to calculate the reduced widths for each of the detected resonances by the means of the Modified R-matrix approach described in the previous chapter, using Eq. 3.27. Remembering the standard formula for the channel radius, $R = 1.3(A_1^{1/3} + A_2^{1/3})$ where A_1 and A_2 are the mass of the two nucleus involved in the channel, it is possible to define

the values for $R_{n^{17}O} = 4.64$ fm and $R_{\alpha^{14}C} = 5.20$ fm. The HOES cross section was also folded with four Gaussian having a $\sigma = 17$ keV to take into account the finite experimental energy resolution. It is clear that the only free parameter to match the HOES modified R-matrix calculation to the THM experimental data is the normalization factor K, which can be obtained by applying the procedure described in Ref. [41] that we will schematically report here.

First we take the reduced widths, obtained using the R-matrix fit procedure described before, for the resonances detected by direct measurements, namely the 2^+ and 3^- one. We then use these reduced widths as an input for the modified R-matrix calculation and subsequently adjust the scaling factor K in order to reproduce the THM experimental cross section. However, as it can be seen in Fig. 4.35 it was not possible to correctly reproduce at the same time the experimental THM data for both resonance considered. The calculated Modified R-matrix was significantly higher than the experimental data for the 3^- resonance. For this reason we decided to take as reference only the 2^+ resonance at ~ 170 keV and its γ_n and γ_α reduced widths to tune the scaling factor K. In this way we normalized the Modified R-matrix calculation to the experimental data for the 2^+ resonance. We therefore evaluated an error on the estimation of this normalization factor K of about 10%. Once the normalization procedure is complete, K is fixed as a constant alongside γ_n and γ_α of the 2^- resonance used as reference. Then the Modified R-matrix will be fitted, leaving the γ_n and γ_α of the remaining three resonances as free parameters, to the whole THM experimental differential cross section.

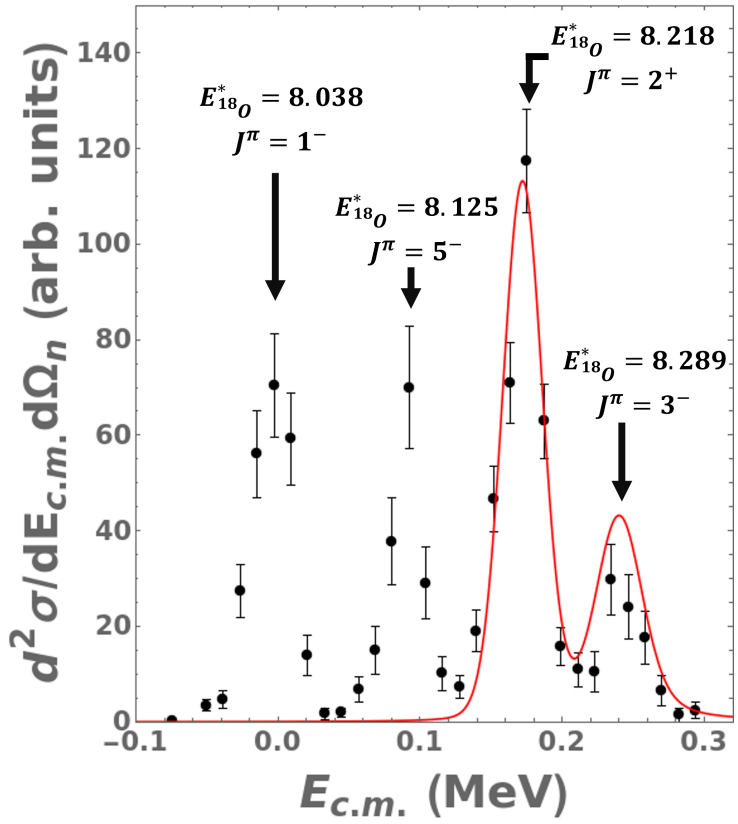

Figure 4.35: Intermediate result of the Modified R-matrix (red curve) normalization procedure to the experimental HOES differential cross section (black points). Labels attached to the black arrows pointed at the four detected resonances indicate the corresponding excited level of the intermediate ^{18}O system (in MeV) and the relative J^π. Details are reported in the text.

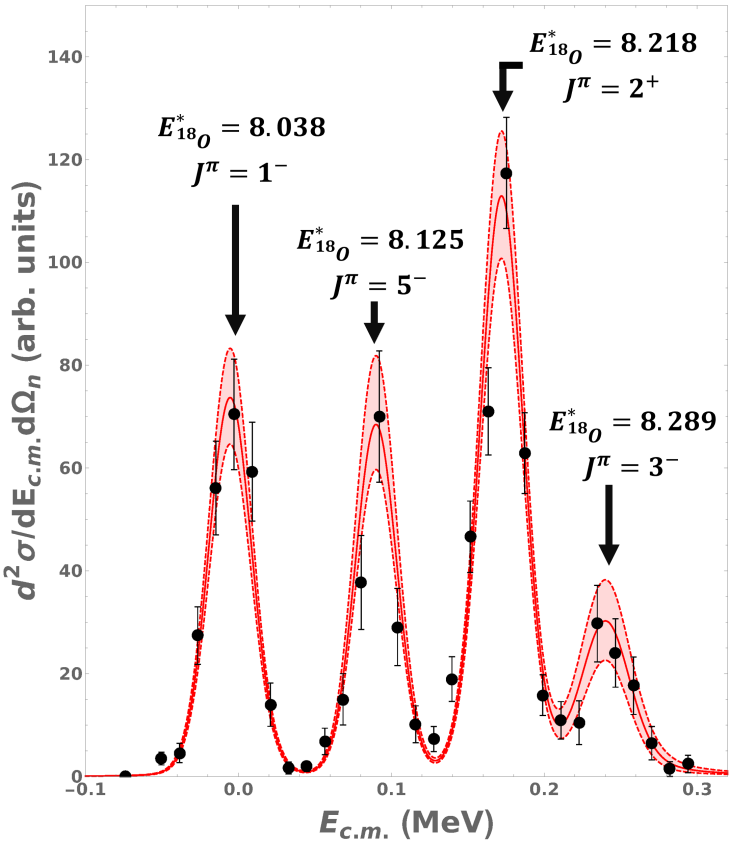

Figure 4.36: HOES differential cross section as obtained by the Modified R-matrix calculation (red line) alongside its confidence interval (light red band) and the THM data (black points). Labels attached to the black arrows pointed at the four detected resonances indicate the corresponding excited level of the intermediate ^{18}O system (in MeV) and the relative J^π.

In Fig. 4.36 we can see the result of the Modified R-matrix fit procedure for the HOES cross section (red curve) alongside its confidence interval (light red band) and the THM data (black points). By looking at the figure we can say that the fit was indeed successful and we were able to reproduce our experimental data. By comparing this result with the ones obtained in past THM measurements [44, 22] we can see that we have indeed achieved a better energy resolution, a slightly better statistical error but unfortunately the hindered population of the 3^- resonance still remains. A deeper analysis on this should be carried out to understand what is the real cause of the issue, even thought we can assume that it could be related to the energy selection of the events. Therefore a solution could be performing the experiment a higher energies which in turn could be also beneficial for the normalization procedure of the THM data, having now more resonances to use that also are at higher energies and, as we saw in the dedicated section, better studied by scattering and other direct measurements.

The values for Γ_n, Γ_α and Γ_{tot} for each detected resonance are finally e reported and compared to the ones obtained in the work of Guardo et al. [22] and Wagemans et al. [43] Tab. 4.9 . It must be stressed once again that the HOES reduced widths are exactly the same that appear in the OES R-matrix, therefore the values obtained via the modified R-matrix fit can be rightly compared to the ones obtained by direct measurements. For simplicity, however, usually the comparison is done by looking at the partial widths, as we did here, that can be easily calculated from reduced widths as we already mentioned.

By looking at Tab. 4.9 it is possible to notice some interesting aspects when comparing our data to the one of Guardo et al. . First it must be stressed that, as the authors wrote in their work, they used the data of Wagemans et al. to perform the normalization of THM data. As we saw in the dedicated section, the values of Wagemans et al. are very similar to the ones we obtained through the MCMC analysis despite the

$E_{c.m.}$ (keV)	J^π	Γ_n (eV)	Γ_α (eV)	Γ_{tot} (eV)
Modified R-matrix fit				
-5.4 ± 0.4	1^-	200 ± 10 (rw)	1884 ± 100	1884 ± 100
90 ± 0.1	5^-	0.16 ± 0.8	26 ± 10	27 ± 12
172 ± 0.5	2^+	250 ± 10	2000 ± 80	2250 ± 100
240 ± 0.2	3^-	2100 ± 400	9100 ± 2000	11200 ± 2400
Guardo et al. [22]				
-6	1^-	0.01 ± 0.001	2400 ± 300	2400 ± 300
75	5^-	0.05 ± 0.006	36 ± 5	36 ± 5
178	2^+	86 ± 11	2200 ± 300	2260 ± 300
244	3^-	1700 ± 450	13000 ± 3400	14700 ± 3800
Wagemans et al. [43]				
-6	1^-	27 (rw)	2399	2400
n.a.	5^-	n.a.	n.a.	n.a.
178.3 ± 0.8	2^+	76 ± 4	2182 ± 132	2258 ± 135
253.0 ± 1.2	3^-	1078 ± 22	13661 ± 416	14739 ± 590

Table 4.9: Partial and total widths for each of the detected resonance as obtained by the Modified R-Matrix calculation, alongside the ones obtained by Ref. [22, 43]. $E_{c.m.}$, as obtained by the the current fit and by Ref. [22, 43], is also reported (first column) with the J^π value of the corresponding level.

normalization factor needed to fit their data. This then clearly explain the similarities for the alpha partial strength, expect for the $3-$ resonance where we were forced to constrain only the total width to the MCMC result. Shifting our focus to the the neutron partial width, we can see that for the sub-threshold level the authors gave an estimation of the partial width, meanwhile we here report just the reduced width as in Ref.[43]. For the other resonances we get consistently higher values of the neutron partial widths which, as already said before in this chapter, can be also

explained by the normalization used. In a sense, when comparing our THM data to the one of Guardo et al. we are getting the same relation to when comparing the MCMC/R-matrix calculation to the data of Wagemans et al. . This is a clear evidence of how the normalization of THM data is a fundamental step for the good outcome of the analysis.

Another interesting aspect to notice is that Guardo et al. have smaller relative errors for the 5^- and 3^- resonances: this is linked to the different error evaluation between our work and theirs. As the authors wrote, they attributed to the normalization factor K a relative error of about 15% which is then responsible of most of the error in the Modified R-matrix calculation of the HOES cross section. We however put a lower value of about 10% to the normalization factor and in turn we increased the relative error in the reduced widths used as input when needed. Indeed, when performing the fit one can notice that the $5-$ resonance is not much sensitive to variations of the relative neutron and alpha reduced widths, which makes sense since it is populated at an high angular momentum $\ell = 3$ which also effects the HOES cross section via the TH amplitude reported in Eq. 3.28. Something similar holds true for the 3^- resonance: in this case, having experimental point with lower statistical count and higher relative statistical error, the fit is less constrained by the parameters of the resonance, thus explaining the higher overall error in the partial widths obtained with respect to the ones of Guardo et al. .

Comparing now our results with the one reported by Wagemans et al. we can notice once more the effect of the different normalization of the two datasets. However even taking into account this, we can still notice that the neutron reduced width for the $1-$ resonance is much higher in our data, ten times more than what Wagemans et al. reported. This significant difference can be due to the different experimental approaches used to obtain the measurements in the first place. Another explanation can come from the analysis procedure, considering Wagemans et al. used a different approach to fit their data. It would be interesting to see how

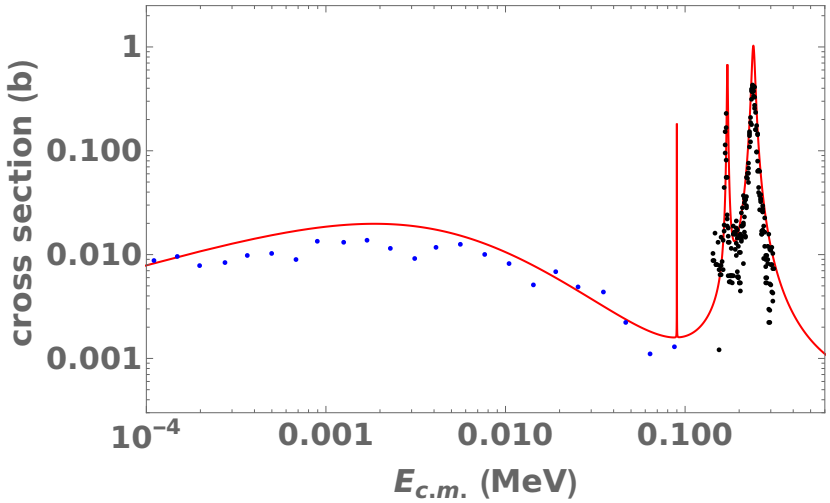

Figure 4.37: R-matrix calculation (red line) for the cross section using the partial widths as obtained by the Modified R-matrix fit of THM data. Data from Ref. [42] (blue points) and [43] (black points) are reported for reference

this affect the reaction rate, as it will be discussed in the following section.

Finally, in Fig. 4.37 we used the partial widths obtained by the THM analysis to calculate the R-matrix cross section and compare it to the direct measurement of Wagemans et al. and Koehler et al.

As we can see, the parameters obtained by the Modified R-matrix fit well reproduce both the low energy trend of the data of Koehler et al. and the shape of the high energy points of Wagemans et al. with a difference in the scaling of about 3, in accordance to what we obtained before by the means of the R-matrix analysis.

4.5 Reaction Rate evaluation

Once the cross section has been evaluated, it is possible to calculate the reaction rate for the $^{17}O(n,\alpha)^{14}C$ using the standard formula [3]:

$$N_A \langle \sigma v \rangle = \frac{3.7318 \cdot 10^{10}}{T_9^{3/2}} \sqrt{\frac{A_1 + A_2}{A_1 A_2}} \int_0^\infty E\sigma(E) \exp\left(\frac{-11.605E}{T_9}\right) dE \tag{4.18}$$

where N_A is the Avogadro number and $\langle \sigma v \rangle$ is the convolution of the cross section with the Maxwell distribution, E is the energy expressed in MeV, A_i is the atomic mass of the i-th nuclei in a.m.u., σ is the cross section in barn, and T_9 is the temperature in expressed in GK. Having performed both a R-matrix analysis of direct data and a new indirect measurement using the THM, we will therefore calculate the reaction rate using the results obtained by these two approaches.

4.5.1 Direct data

AZURE2 already gives the user the possibility to calculate the reaction rate by inputting a list of temperatures at which perform the calculation, the code will then interpolate between these points and plot the resulting graph. However during this work a peculiar bug of the code was encountered, which resulted in an underestimation of the reaction rate at the boundaries of the energy range of interest. The issue was simply overcome by setting up a Mathematica notebook which will take as input the cross section as obtained from the MCMC calculation and calculate the integral for both the most probable value and for the error bands. We verified that in our case there is no difference in the relative error obtained between this approach and obtaining the 16th,50th and 84th percentile of the rate directly from the MCMC calculation. In Figure we can see the final result: the rate obtained is identical, at low temperatures, to the one of Koehler et al., which is expected since in the thermal energy region our fit is strongly constrained by their data, but then it evolves in with

a trend very similar to the one of Wagemans et al., only with a scaling factor. This is also expected, as we explained before.

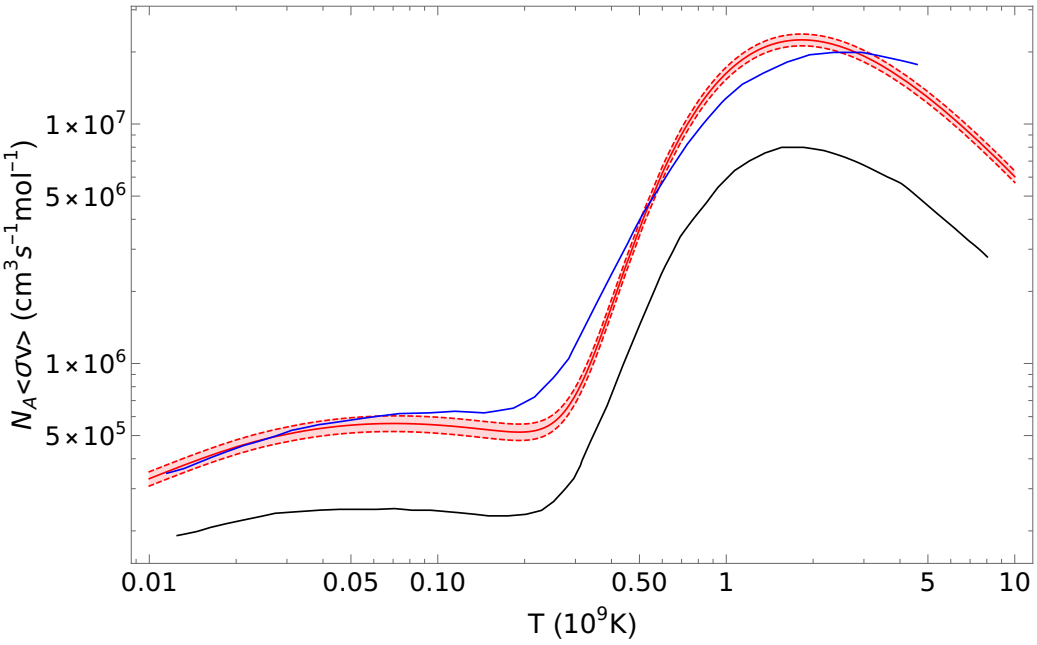

Figure 4.38: Reaction rate and its confidence interval as calculated by the combined MCMC and R-matrix analysis (red) alongside those obtained in Ref. [43] (black) and [42] (blue)

4.5.2 THM data

With the cross section calculated by using the partial widths obtained from the THM data fit as input for the R-matrix, it is possible to also evaluate the reaction rate using Eq. 4.18, the result of which is shown (green line) with its confidence interval in Fig. 4.39 alongside the reaction rate as calculated by Ref. [42, 43] (again blue and black lines, respectively) and to what we obtained by the means of the MCMC analysis and already reported in Fig. 4.38 (again in red). Here we can see that for high temperatures we get something very similar to what Koehler et al. and our MCMC analysis already obtained. However, the more interesting aspect is that we get a sensible higher reaction rate at lower temperature, also when compared to the MCMC result which, in a sense, represent the summary of the direct data available in the literature. This increase is linked to the higher value for the neutron reduced width we obtained for the sub-threshold 1^- resonance, as already explained above. It should be definitely studied in the context of the astrophysical environment to verify if this variation indeed affects weak component of the s-process.

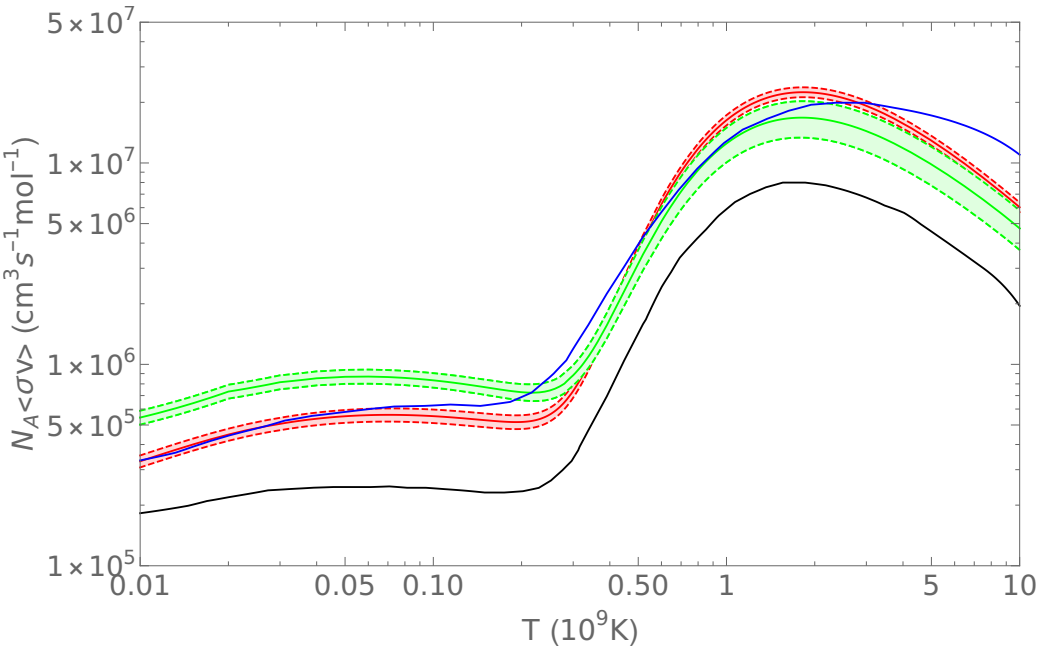

Figure 4.39: Reaction rate and its confidence interval as calculated by using the values of the resonance strengths obtained through the THM analysis (green) alongside the rate obtained in [42, 43] (blue and black lines, respectively) and to what we obtained by the means of the MCMC analysis (red)

4.6 Conclusions and future perspectives

We can conclude this chapter by affirming that we were able to analyze in details the $^{17}O(n,\alpha)^{14}C$ reaction by both reviewing the direct data available in literature, by the means of a R-matrix analysis, and analyzing the data obtained by a new devoted THM measurement. The inconsistencies between direct measurements were mostly resolved thus obtaining a common result for the R-matrix fit that, in turn, we used as a reference for the THM data analysis. Finally, by the means of a Modified R-matrix fit, we were able to extract the partial widths for the detected resonances in the THM data obtaining a significantly higher result for the sub-threshold resonance with respect to the value estimated by direct measurements. This difference was also visible in the reaction rate calculation, where we found a significantly higher value at lower temperatures than the one obtained from the R-matrix analysis of the direct data in the literature. The natural development for this work would be then to evaluate the impact of such difference to the weak component of the s-process.

Chapter 5

Study of the $^{12}C + ^{16}O$ fusion process via the THM

5.1 Status of Art

As we already discussed in the first chapter of this thesis, the temperature range of interest for $^{12}C + ^{16}O$ fusion lies between 1 (for hydrostatic carbon burning) and 3.6 GK (for explosive carbon and oxygen burning), which corresponds to a center of mass energy range between 3 and 7.2 MeV. This fusion process proceeds mainly through three reaction channels: the $^{12}C(^{16}O,\alpha)^{24}Mg$ (Q = 6.77 MeV), $^{12}C(^{16}O,p)^{27}Al$ (Q = 5.17 MeV) and partially the $^{12}C(^{16}O,n)^{27}Si$ (Q= - 0.424 MeV). The latter is less favored due to its negative Q-value, in a similar fashion to what has been observed for the $^{12}C + ^{12}C$ fusion and other medium-mass systems [62]. Other reaction channels such as $^{12}C(^{16}O,2\alpha)^{20}Ne$ are hindered by the presence of the Coulomb barrier in the exit channel [63].

In the literature it is possible to find numerous measurements , involving both charged particle and gamma ray spectroscopy [65, 66, 67, 63], of these main reaction channels for the $^{12}C + ^{16}O$ fusion. A comprehensive summary of such measurements can be found in Ref. [63], which

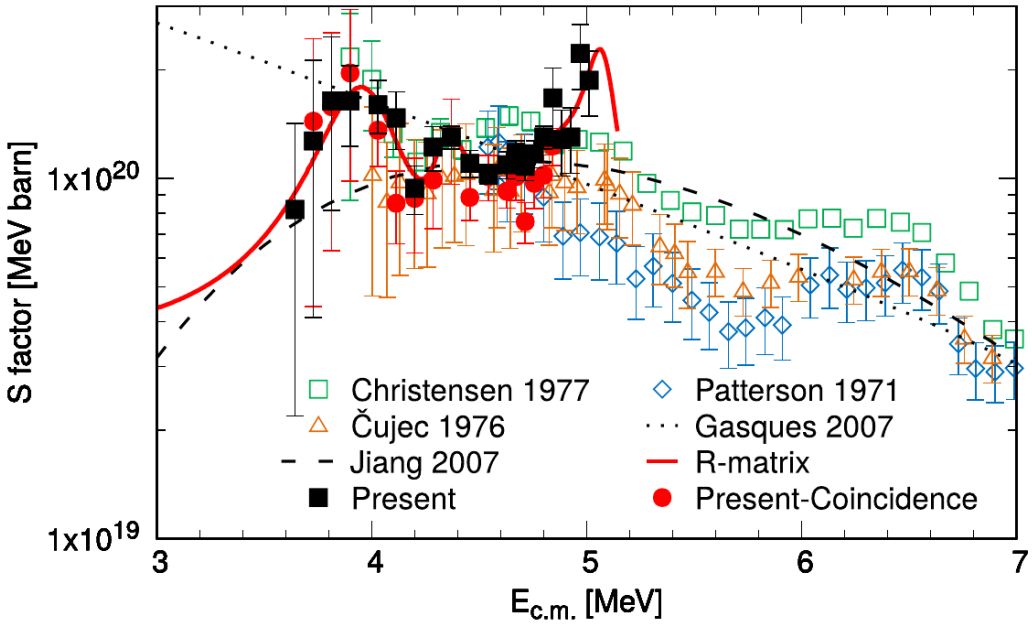

Figure 5.1: Compilation of measured S-factor for the $^{12}C + ^{16}O$ fusion, as shown in Ref. [63]. In addition to the direct measurements, indicated by the various symbols visible in the legend, the dotted line denotes the calculations performed using the Sao Paulo potential [64], the dashed lines represents the fit of all the direct data using the hindrance model in Ref. [62], meanwhile the red line refers to an R-matrix calculation performed also by Ref. [63]

we show here in Fig. 5.1. As it can be seen from the figure, multiple measurements of the S-factor for these reactions show a pronounced resonance structure just below the Coulomb barrier ($B_C = 8$ MeV) at about 6.4 MeV in the center of mass frame. Below this energy region the datasets show different behaviors: while all seem to suggest an increase of the S-factor around 4.6 MeV, some of the data [65, 66] clearly show a smooth behavior while others show the presence of two more resonance structures around 4.6 and just below 4 MeV. The data of Fang et al. goes even beyond showing three different resonances in the energy region from 5 down to around 4 MeV.

From Fig. 5.1 it is also possible to notice that up to now the S-factor has been measured only down to around $E_{c.m.} = 4MeV$. Only the data of Fang et al. [63] goes lower, pushing down to around $E_{c.m.} = 3.6MeV$, but with an error bar larger than the experimental points at higher energies. This means that even with the data of Fang et al. it is not possible to enforce a significant constraint on the S-factor fit calculation. Therefore the use of extrapolation is still required for the remaining part of the energy range of interest, namely from 4 down to 3 MeV. The result of the extrapolation procedure is, however, heavily influenced by a series of factors both nuclear, such as the chosen model for the interaction potential or the presence of unforeseen nuclear effects (i.e. clustering, molecular-like behavior, etc.), and astrophysical such as the stellar environment [62]. Extrapolations from current data based on different models differ by two orders of magnitude around 3 MeV and in particular, the proposed [62] sub-barrier fusion hindrance effect would drastically reduce the reaction rate at astrophysical energies. It is worth noticing that even small variations of the strength of the reaction channels mentioned above would imply large variations in the α or p production for further nucleosynthesis processes.

For all the reasons mentioned in this paragraph, it is clear that further measurements extending down to at least 3 MeV would be extremely im-

portant. In the aforementioned astrophysical scenario this will translate to a better evaluation of the influence of the $^{12}C + ^{16}O$ fusion in hydrostatic carbon burning. We therefore decided to perform a new measurements using the THM to better explore this energy region, leveraging the strengths of the method in studying the S-factor below the Coulomb barrier.

5.2 Applying the THM to the $^{12}C + ^{16}O$ fusion

As stated in the previous chapter, the first step for applying the THM to a two-body reaction is to choose a proper TH nucleus and therefore a proper three-body reaction. In this case we need to either transfer a ^{12}C or a ^{16}O nucleus in the entrance channel. Since making both a carbon or oxygen target is relatively easy, the choice depends only on the kinematics of the three-body reactions, considering the energy we want to reach in the two-body one, and on the TH nucleus itself that needs to have a well known cluster structure hosting either a ^{12}C or a ^{16}O nucleus and and a binding energy that is adequate for the energy range we want to study in the corresponding two-body reaction. In this regard there is already in literature the evidence [68] of a $^{12}C + d$ clustered state for the ^{14}N nuclei that has been already successfully used in a THM experiment [13]. Therefore we decided to study the $^{12}C(^{16}O, \alpha)^{24}Mg$ and $^{12}C(^{16}O, p)^{27}Al$ reactions by applying the THM to the $^{16}O(^{14}N, \alpha^{24}Mg)^{2}H$ and $^{16}O(^{14}N, p^{27}Al)^{2}H$ three-body reactions.

Once again, by using Eq. 4.2 and 4.3 it is possible to evaluate the necessary beam energy to explore the energy range of interest, namely between 2 and 5 MeV in the center of mass frame. Since the $^{12}C + d$ cluster system inside the ^{14}N nuclei has a binding energy of 10.27 MeV, if we choose a value of $E_{c.m.} = 6$ MeV we can calculate the beam energy to be:

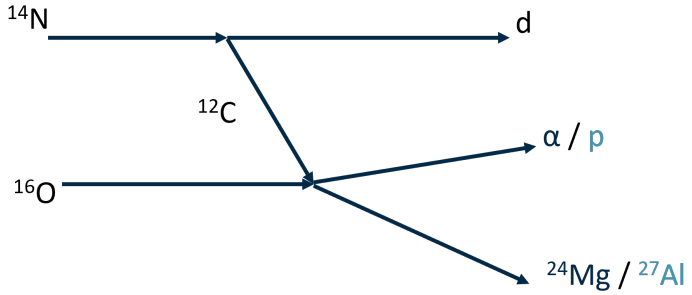

Figure 5.2: Pole diagram of the three body TH reactions of interest.

$$E_{beam} = (E_{xA}^{c.m.} + \epsilon_{sx}^{a})28 * 187 \frac{m_{^{12}C} + m_{^{16}O}}{m_{^{16}O}} \frac{m_{^{14}N}}{m_{^{12}C}} \sim 33.2 MeV \tag{5.1}$$

We choose to focus our energy range on 6 MeV in the center of mass frame to have as much direct measurements data as possible in order to have the best chance to properly perform the normalization of THM data which, as we saw in the previous chapter, is a fundamental part of the analysis. We can then use the Fermi motion between the clusters inside the TH nucleus to compensate for the momentum transferred to the two body reaction, thus expanding the energy range that we can study. It's possible to verify this assumption before running the experiment by using the Monte Carlo simulation mentioned in the previous chapter: indeed, by looking at Fig. 5.3 where $E_{xA}^{c.m.}$ as obtained by the simulation is plotted against the momentum of the spectator, we can clearly see that by putting a cut of $p_s < 80 MeV/C$ it is possible to actually span an energy region of $E_{xA}^{c.m.}$ between 1 and 8 MeV. Of course it should be remembered that using events from the tail of the momentum distribution of the spectator, while still below the Shapiro limit, can result in some distortion effects that we should be able to identify and remove during the analysis.

Once the beam energy was correctly selected and the entrance channel of the three-body reaction is defined, it is possible to use the Monte

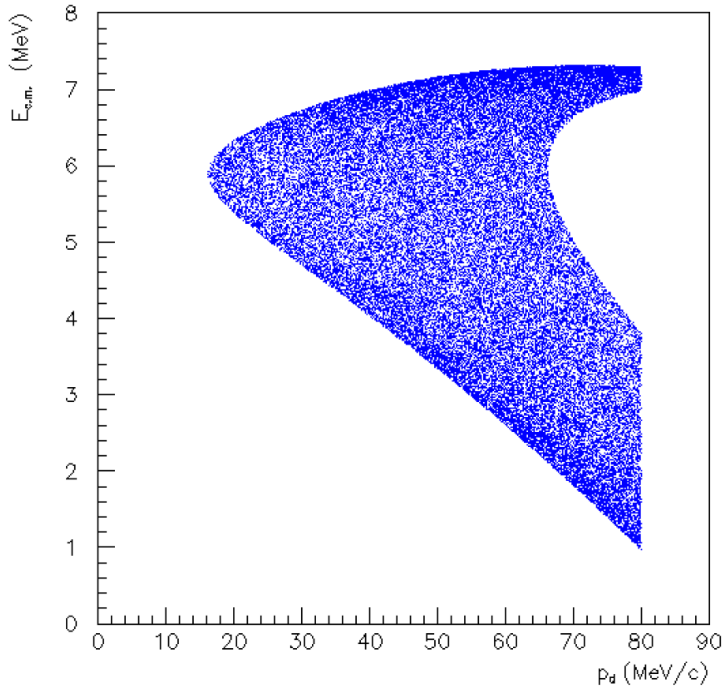

Figure 5.3: Two-dimensional plot of the energy in the center of mass frame $E_{xA}^{c.m.}$ versus the momentum of the spectator as obtained from Monte Carlo simulation with the condition $|p_s| < 80\,MeV/c$.

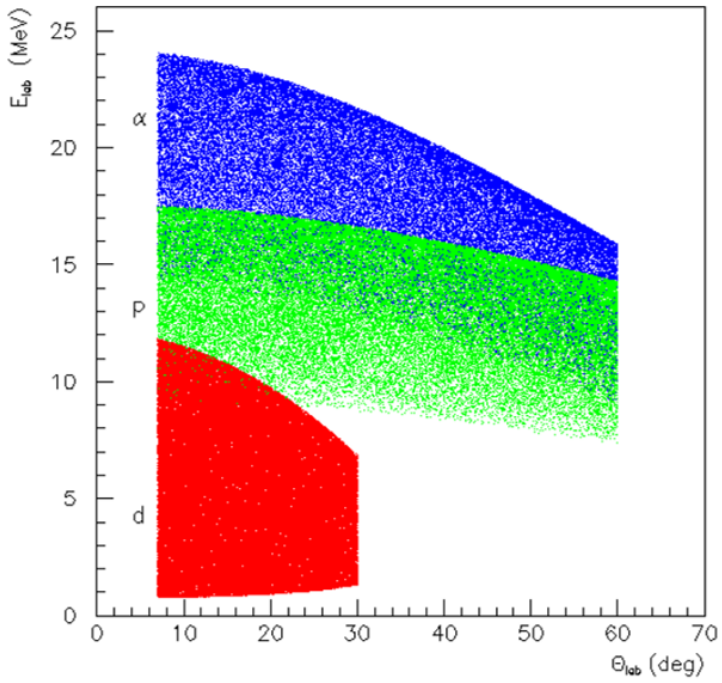

Figure 5.4: Two-dimensional plot of the energy versus the angle of emission of the α particles (blue locus), protons (green locus) and deuterons (red locus) as obtained from Monte Carlo simulation with the condition $|p_s| < 80\,MeV/c$.

Carlo simulation to evaluate the behavior of the particles in the exit channel. It was immediately clear that detecting the intermediate mass nuclei, either a ^{24}Mg or a ^{27}Al, was not feasible since they would exit the reaction with a kinetic energy too low to produce a proper signal in our detectors. Therefore we turned our attention to the light particle of the two-body reaction, either an α or a proton, and the deuteron spectator. In Fig. 5.4 it is possible to see the energy versus the angle of emission of each of the three particles we want to detect, as calculated by the simulation with once again a cut on the momentum of the proton spectator of $p_s < 80 MeV/C$. One can immediately notice that the deuteron spectator (red points in the plot) has, as expected for the QF breakup of the TH nu-

cleus in the beam, a narrow angular range of emission of 30° around the beam axis, while the α and the proton (respectively blue and green points) span a wider range between 0° and 60°. This means that in the range between 0° and 30° we should be able to perform a particle identification not only in charge but also in mass, having to distinguish protons from deuterons. However, we should also take into account that the emission energy for the deuterons could go from 12 MeV down to 1 MeV, therefore the energy threshold of the detectors should be lower than such values. Moreover, we should also consider the possibility that a lower threshold might cause the protons, that have a slightly lower mass but a significant higher energy than the deuterons, to "punch through" the detector.

5.3 Experimental setup

Considering what was discussed in the previous section we decided once again to perform the particle identification by applying the $\Delta E - E$ technique using an array of detector telescopes, arranged as showed in Fig. 5.5. In this case each telescope is composed by three different stages to correctly identify all the products of interest in the exit channel, as already discussed. The first stage consisted of a 35 μm Position Sensitive Detector (PSD), the second one of a 100 μm PSD, and the third one of a 1500 μm silicon pad detector. The thickness of the first stage was chosen in order to balance the detection threshold with the necessity to discern protons from deuterons, meanwhile the third stage was added in order to collect high energy protons that might not stop in the first two stages. A total of four telescopes were used, symmetrically placed with respect to the beam axis, covering the angular range from 7° to 30° and from 45° to 68° in order to fulfill the QF kinematic conditions as showed by the MC simulation. In Table 5.1 a summary of the setup is reported.

For a series of experimental runs for the first stage of T2 and T3 telescopes a 65 μm thick PSD was used instead of the 35 μm one to better

Telescope	Angular range (deg)
T1	$45 \div 68$
T2	$7 \div 30$
T3	$7 \div 30$
T4	$45 \div 68$

Table 5.1: Angular range covered by the four telescopes in the experimental setup.

resolve deuterons from protons though with a larger detection threshold,but still not affecting the relevant phase space region of interest for the experiment.

The ^{14}N beam was accelerated by the Van de Graaff tandem of the Laboratori Nazionali del Sud (LNS-INFN) to an energy of 33.7 MeV. A 458 μg/cm^2 thick WO_3 target was used. All the detection setup was placed inside the CT2000 scattering chamber, as it can be seen in Fig. 5.6 where a picture of the experimental setup is showed.

5.4 Calibration of the detectors

The first stage of the telescopes needs to be used just for the particle identifications, in conjunction with the second one, therefore no calibration is necessary to its purpose, however we should still evaluate the energy lost in the detector by each of the detected particle in order to correctly define their energies. To this aim the thickness of the detector, being quite small, was treated as a dead layer of silicon and the energy reconstructed using three different dE/dx energy loss curves obtained by fitting a SRIM calculation with a polynomial. Meanwhile, since the third stage is included in the setup with the only purpose of stopping high energy protons, we just need to calibrate its energy signal with protons. The second stage is then the main detector of the telescope and therefore it must be pre-

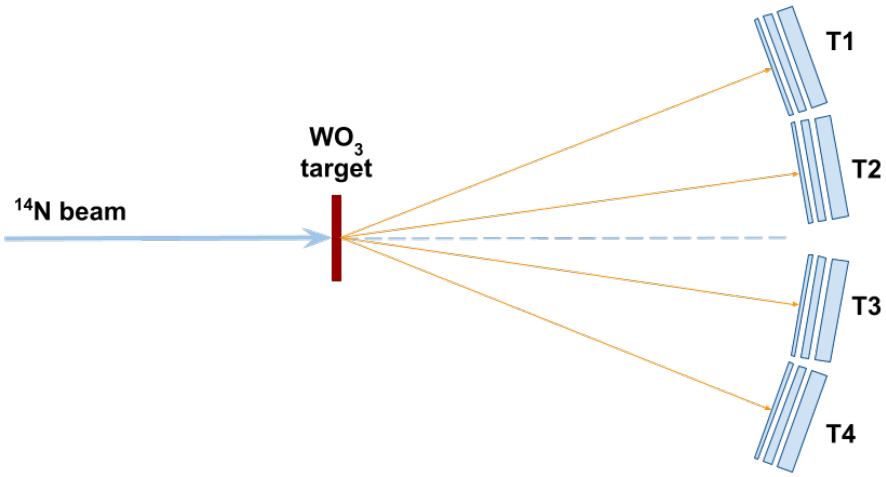

Figure 5.5: Sketch (not in scale) of the experimental setup used.

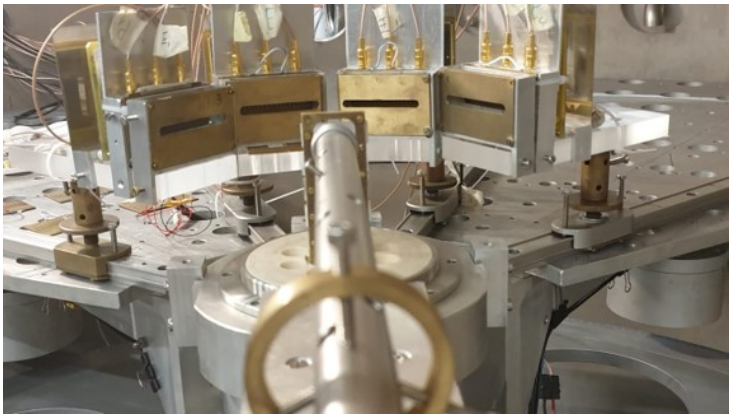

Figure 5.6: Picture of the experimental setup taken from the point of view of the beam injection hole inside the scattering chamber.

cisely calibrated both in energy and position, since it will be the main source of information for the energy and angle of emission of the detected particles. Having to detect three different particles with the same apparatus, three different energy calibrations of the detectors needs to be performed with devoted experimental runs: an eight-peak α source and the $^{2}H(^{14}N,\alpha)^{12}C)$ reaction were used for α particles calibration, meanwhile the elastic scattering of ^{14}N on $^{1,2}H$ was used for both protons and deuterons calibrations. Angle calibration of the second stage detector was also performed, during the same runs, by once again covering it, as we did in the previous chapter, with a grid with equally spaced slits placed at known angles. For what discussed so far, only the calibration of the second stage detectors will be shown, moreover for this thesis work we will focus only on the central telescopes, T2 and T3.

5.4.1 Second stage detector calibration for energy and position

The calibration procedure of the PSDs is virtually identical to what shown in the previous chapter: we need to fit Eq. 4.4 and 4.6 on a series of experimental points of known energy and position. In Fig. 5.7 it is possible to see the position versus the energy signal, as acquired by the ADC, from the second stage detector of the T2 telescope. The data was acquired during a calibration run using the ^{14}N beam impinging on a CD_2 target. As in the previous chapter, it is again possible to see various experimental loci coming from two-body reactions populating the plot with a background coming from three-body reactions. In this case we are interested only in those events coming either from a proton, a deuteron or an α particle. For this run we identified three different kinematics, highlighted in Fig. 5.7 by ellipses of different colors: in particular the red one indicates the events coming from the scattering of the deuteron in the CD_2 target after the collision with the ^{14}N beam, the green one refers to events coming

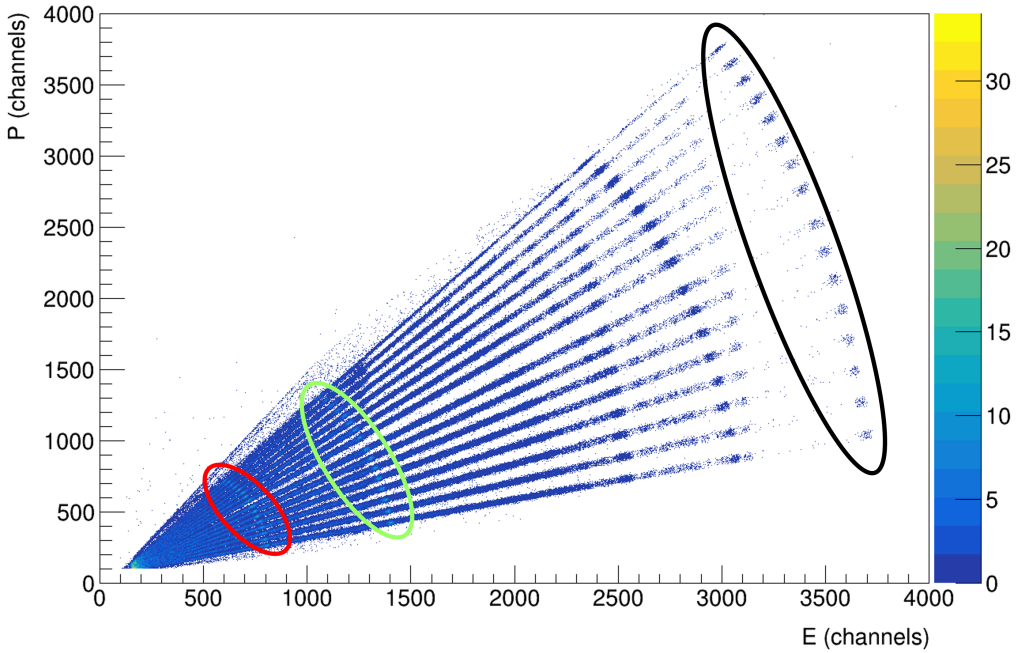

Figure 5.7: Two dimensional plot of the uncalibrated position signal versus the energy signal as measured by the ADC for the second stage detector of the T2 telescope. The data was acquired during a calibration run using the ^{14}N beam impinging on a CD_2 target.

from the scattering of protons in the target while the black one refers to α particles coming from the $^{2}H(^{14}N, \alpha)^{12}C$ reaction.

We then fitted this data, alongside the points coming from other similar runs carried out at different energies of the beam, against Eq. 4.4 and 4.6 to obtain three sets of calibration parameters for each of the detected particles. Then, the successful outcome of the calibrations was evaluated by plotting the same data in Fig. 5.7 but with the calibrated variables this time, namely the angle values and the energy released in the detector. For the plot in Fig. 5.8 we used the fit parameters obtained for the deuterons, that should represent a mean value between protons and α. The known

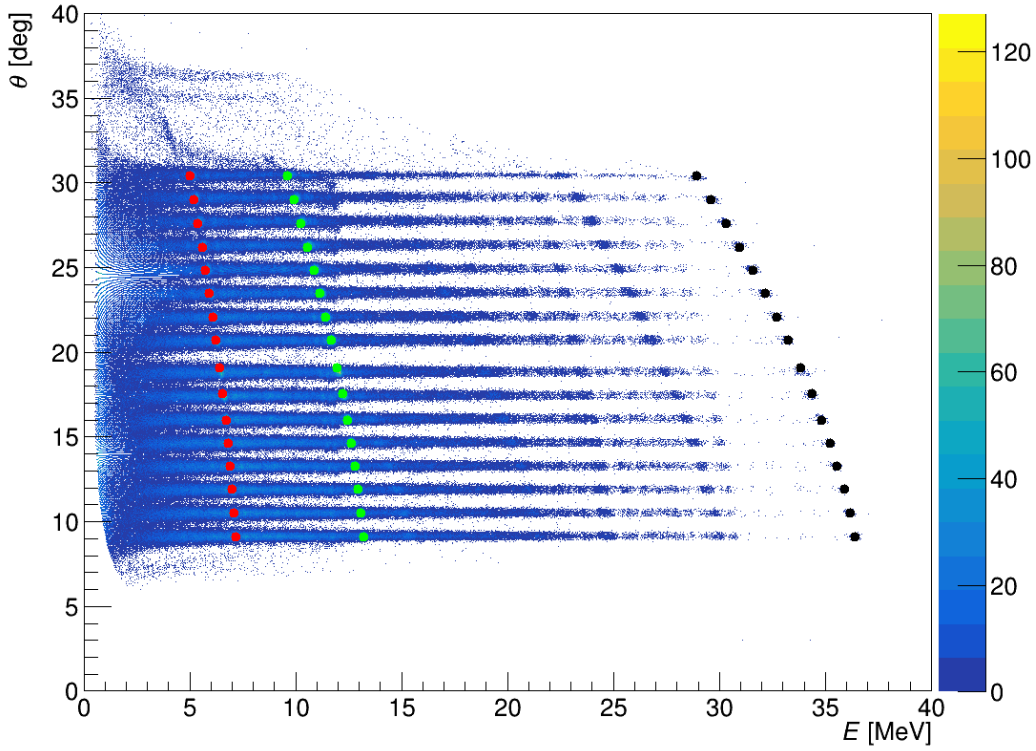

Figure 5.8: Two dimensional plot of the calibrated variables θ versus E for the same events shown in Fig. 5.7

energy and position values, used for the calibration procedure, are represented by filled circles. Once again red circles refers to events coming from the scattering of deuterons, the green ones to events coming from the scattering of protons and the black ones refer to α particles from the $^{2}\mathrm{H}(^{14}\mathrm{N},\alpha)^{12}\mathrm{C}$) reaction. From the figure a good agreement shows up within the experimental limits, between all the theoretical points and the corresponding accumulation regions of the measured events, which indicates both the correct calibration procedure for this detector and that the correction factor in the calibration parameters, for the three detected particles, is negligible.

5.5 Selection of the $^{16}O(^{14}N, \alpha^{24}Mg)^{2}H$ reaction channel

For the first step of the THM analysis we need once again to perform the particle identification procedure described in the previous chapter, using the $\Delta E - E$ technique on the energy data collected from the first and second stages of our telescopes. Once the particles are correctly identified we can then select the $^{16}O(^{14}N, \alpha^{24}Mg)^{2}H$ reaction channel of interest. First we must select the deuterons in either T2 or T3 telescope and, subsequently, the α particle in the other. However, as it can be seen in Fig. 5.9 the ΔE energy signal from the first stage detector underwent a drift during the various runs due to instabilities in the electronics.

Likely, the drift was slow enough that it is possible to divide the data in bunches composed of 10^4 events, where the signal was stable and perform the particle identification for each bunch separately. In Fig. 5.10 the same $\Delta E - E$ plot for one of these data subset is showed and indeed it is possible to see three different loci where we can easily identify the protons, due to their punch-through effect, and subsequently identify the deuterons and the α particles. However here another issue appeared: in Fig. 5.10, highlighted by a red ellipse it is possible to see the presence of a strange accumulation of points in what should be the deuterons locus. The accumulations is strange because it suddenly stops at a certain E_{T3} value in a similar fashion to what happens to protons punching through the detector. This however should not happen for the deuterons since the thickness of the second stage detector was chosen in order to stop all the deuterons, considering what has been shown in Fig. 5.4. We then turn over the experimental runs obtained using a first stage detector 65 μm thick, to verify if this behavior is also present in those data. Once again the drift of the ΔE signal is present, since only the detectors were changed but not the electronics, confirming that the issue is indeed not caused by the detectors. Therefore, we sliced also this data, taking again only 10^4

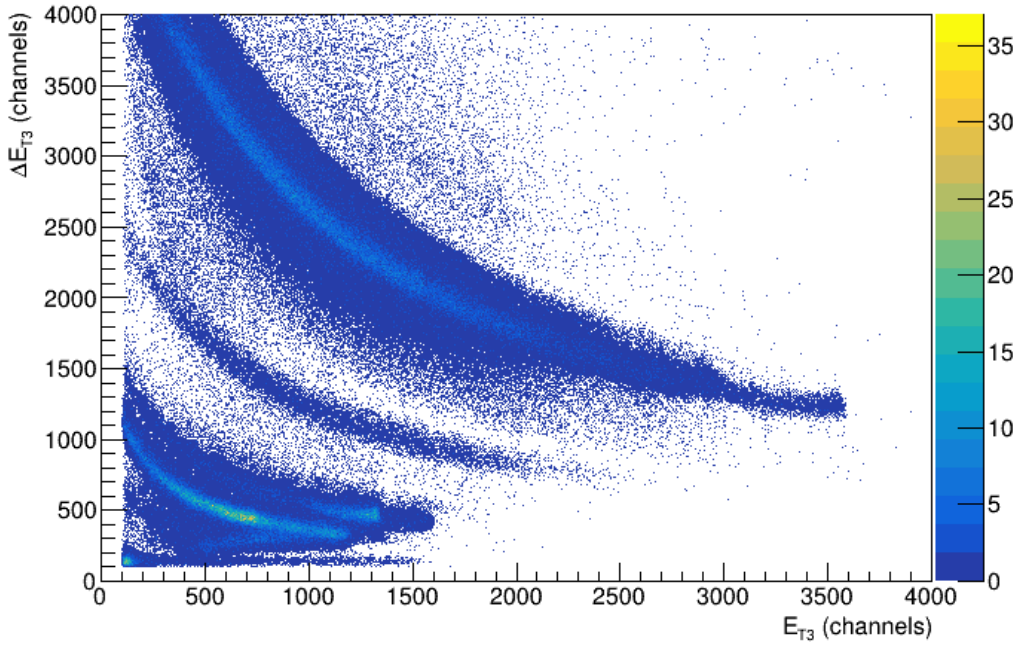

Figure 5.9: Scatter plot of the energy loss (in ADC channels) as a function of the total energy of the particle (in ADC channels) as obtained by the first two stages of the T3 telescope. The broadening of the loci is due to a drift in amplifications, as discussed in the text.

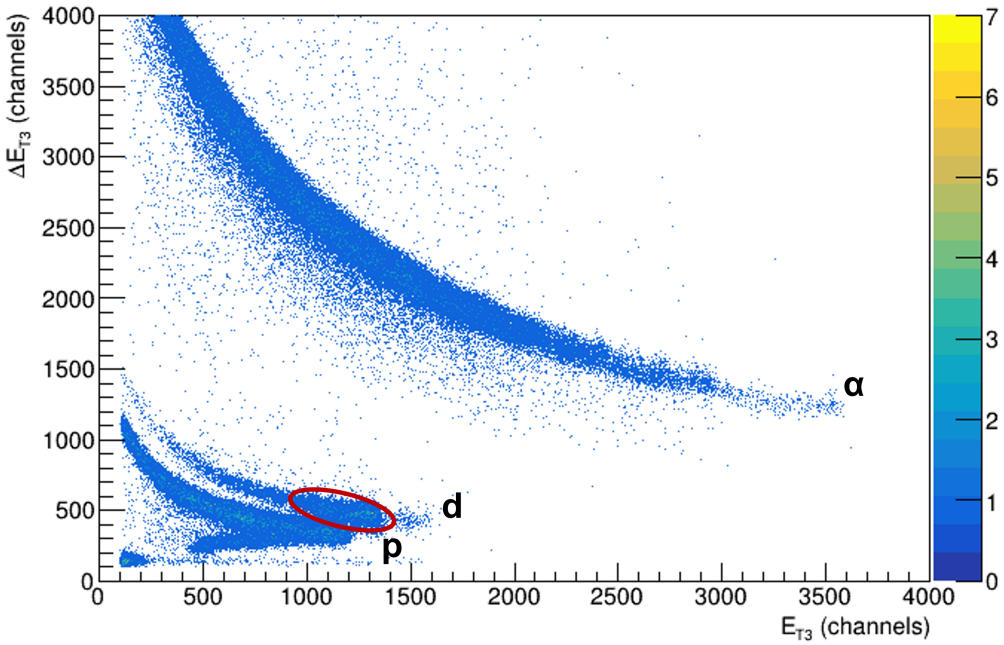

Figure 5.10: Scatter plot of ΔE versus E as shown in Fig. 5.9 but with a cut on the total number of events displayed to 10^4.

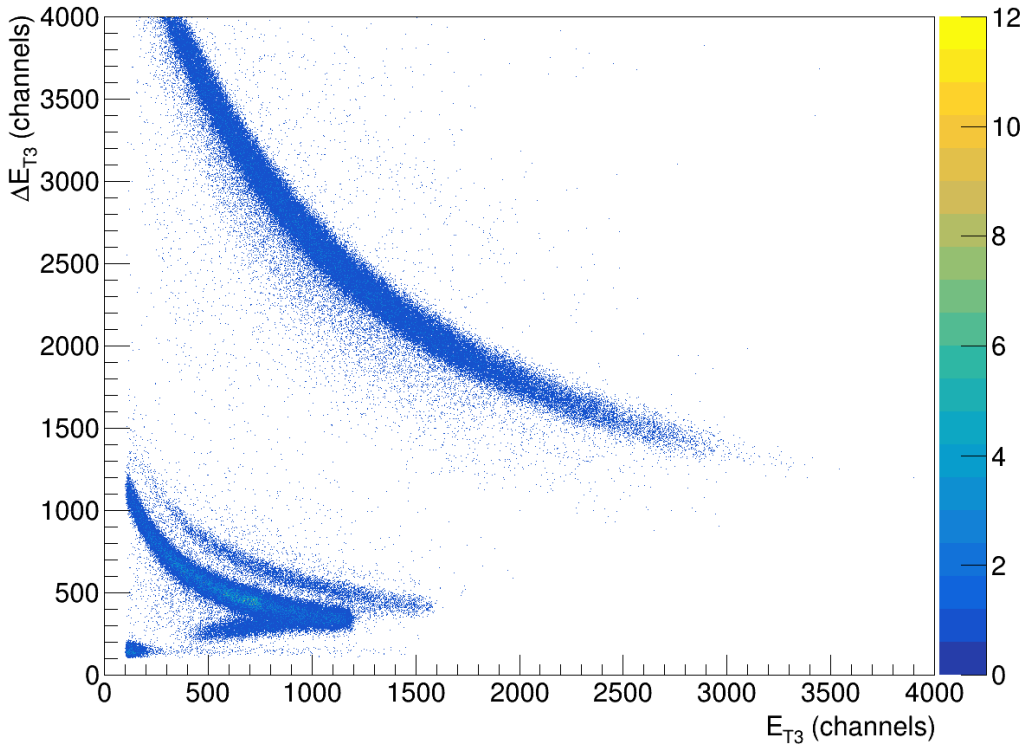

Figure 5.11: Scatter plot of ΔE versus E variables as obtained for the runs with the 65 μm PSD detector as first stage of the telescope. Also in this case the total number of events shown is limited to 10^4.

events to populate the $\Delta E - E$ plot in Fig. 5.11 Here we can immediately see that such accumulation of events is not present in the deuterons locus, confirming our suspects. What it has been shown so far refers to the first stage of the T3 telescope, however an identical situation is present in the symmetrical T2 telescope that we need to also use for our analysis.

Since completely removing the problematic region of the $\Delta E - E$ plot is not feasible without also loosing most of our data, we then decided to proceed with the selection of the particles also including these events as if they are actually coming from deuterons. Then, in order to isolate this

odd behavior in the 35 μm data, we also proceed in parallel with the analysis of the 65 μm data. Once two of the three particles in the exit channel are selected we assume also the presence of an undetected ^{24}Mg nucleus and then reconstruct its kinematical quantities, the energy and the angle of emission, as we did in the previous chapter for the spectator. In this case however we cannot to verify this assumption using the procedure described in Ref. [53], since the selection of the deuterons is not precise enough to exclude events relative to protons. We then proceed to reconstruct the experimental Q-value for the three-body reaction and compare it with the expected values for the ^{16}O(^{14}N, α^{24}Mg)^{2}H reaction, to check if we can clearly see the events of interest and subsequently asses the extent of the background events. In Fig. 5.12 it is possible to see such plot for the 35 μm data (black histogram) against the theoretical values for the ground state and the first three excited state ($Q_{value} = -3.5, -4.87, -7.62, MeV$) of the $^{24}\mathrm{Mg} + \alpha$ intermediate system, indicated by the red vertical lines and the α_i labels.

It is immediately clear that our data is indeed contaminated by events corresponding to completely different reactions which cause a significant background in the Q-value histogram, where it is not possible to easily discern the events we are interested in. As said, we ran the same procedure on the 65 μm data and obtained the plot in Fig. 5.13 where we can see instead the absence of such significant background and indeed the experimental data agree quite well with expected value for the ground state α_0 and the first excited state α_1. Some unexpected peaks are still present, however they do not interfere with the Q-value region of interest. This data set however has quite a low statistic, as it can be seen from the plot, therefore it is not possible to proceed the analysis only with it totally discarding the runs with the 35 μm PSD as first stage.

Still, this comparison confirms that this cluster of events that we saw in the 35 μm ΔE-E plot is clearly not coming from the ^{16}O(^{14}N, α^{24}Mg)^{2}H reaction channel we are interested in. We stated that running the proce-

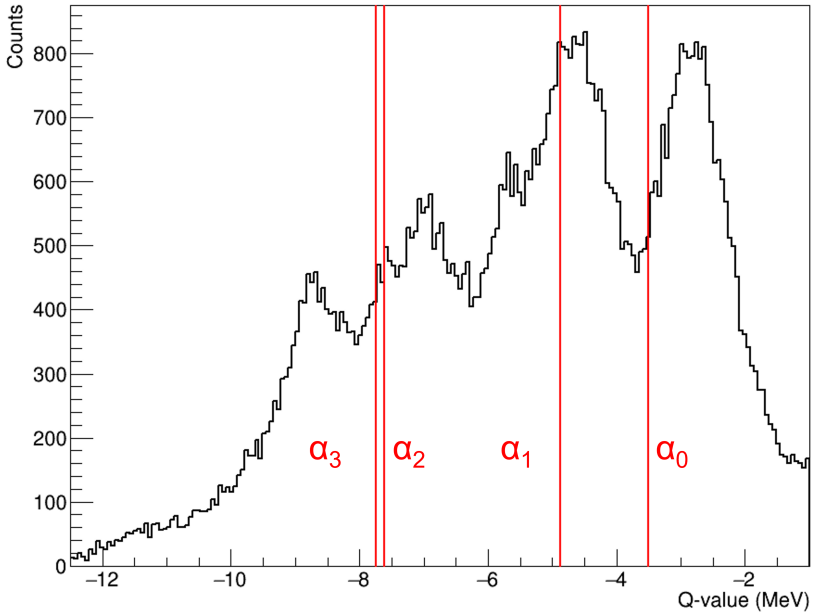

Figure 5.12: Reconstructed Q-value for the selected events in the 35 μm data. The red vertical lines indicate the theoretical values for the ground state and the first three excited state of the $^{24}\mathrm{Mg} + \alpha$ intermediate system, as indicated by the red labels.

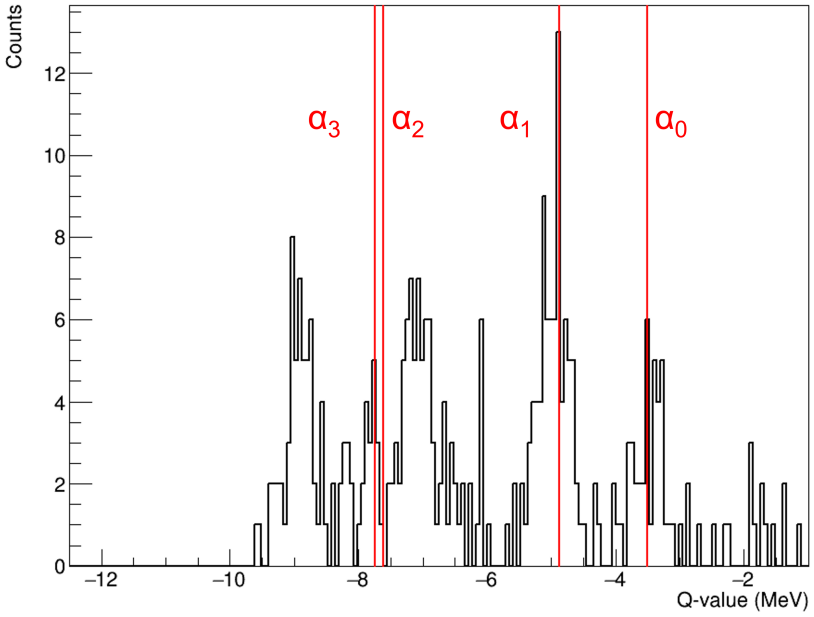

Figure 5.13: Reconstructed Q-value for the selected events in the 65 μm data. The red vertical lines indicate the theoretical values for the ground state and the first three excited state of the $^{24}Mg + \alpha$ intermediate system, as indicated by the red labels.

dure described in Ref. [53] would not make much sense in this particular case, however, considering the issue we are facing, we can exploit the procedure to better select the deuterons spectator. We already defined Eq. 4.10:

$$Y = \frac{1}{A_s} X - Q_{value}$$

but in this case we consider

$$\begin{cases} Y = E_{beam} - E_{^{24}Mg} - E_\alpha \\ X = \frac{p_s^2}{2m} \end{cases}$$

Normally the procedure should be applied to the particle not detected in the exit channel, however here we took into account the kinematical variables for the ^{24}Mg nuclei as reconstructed starting from the variables of the detected α particles and the deuterons themselves. This means that we are making an error in evaluating $E_{^{24}Mg}$ for those events that are not related to deuterons. Nonetheless, since in the worst case scenario they could come from protons, the correction factor we would need to apply to the reconstructed kinematical values for the undetected ^{24}Mg nuclei should be relatively small. In this case we should also consider that the variable X is not reconstructed but actually directly calculated from the energy measured of the detected spectator. In Fig. 5.14 we can see the plot of the Y versus the X variables where also the theoretical values for the ground state and the first three excited states of the $^{24}\text{Mg} + \alpha$ intermediate system are reported for deuterons (red lines) where $A_s = 2$.

By looking at the figure we can finally confirm that in our data are indeed present the events for the $^{16}\text{O}(^{14}\text{N}, \alpha^{24}\text{Mg})^2\text{H}$ reaction channel but they are covered by a significant number of background events. The cluster of events that we saw in Fig. 5.10 here is represented by a series of clusters aligned on the left side of the plot with a steeper angular coefficient that can only arise if the mass of the particle is lower than $A_s = 2$. This also confirms our suspect that those events are indeed

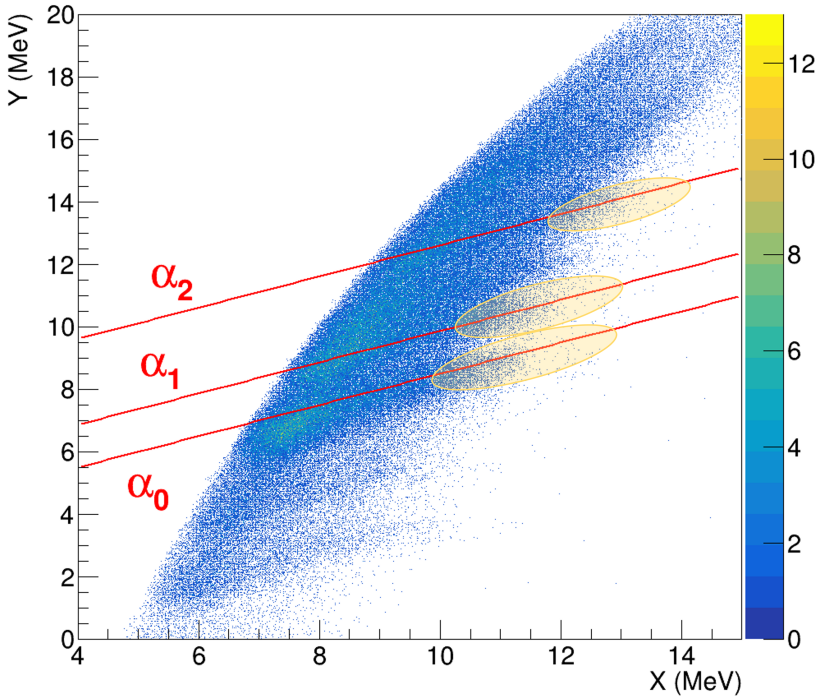

Figure 5.14: Scatter plot of the variables Y and X as defined in Ref. [53]. The red lines are calculated for the values $A_s = 2$ and $Q_{value} = -3.5, -4.87, -7.62, MeV$. Yellow ellipses are an visual hint to highlight the events selected for filter out the deuterons from the protons.

coming from protons punching through the detector: the explanation of such behavior of the detection system, however, is yet to be determined. We can now proceed with the analysis taking into account all the data by carefully selecting, as showed by the yellow ellipses, the events that are located on the right side of the plot near the theoretical values represented by the red lines.

After selecting in such way the events relative to the ground state α_0, we can verify our selection by comparing, as visible in Fig. 5.15, the experimental (red points) kinematical loci $E_{^{24}\mathrm{Mg}}$ versus E_α and E_α versus

E_d with those obtained from the Monte Carlo simulation (black points). As it can be easily seen, the experimental data agrees with the simulation except few events that are outside the expected boundaries and that will be therefore excluded from the following analysis.

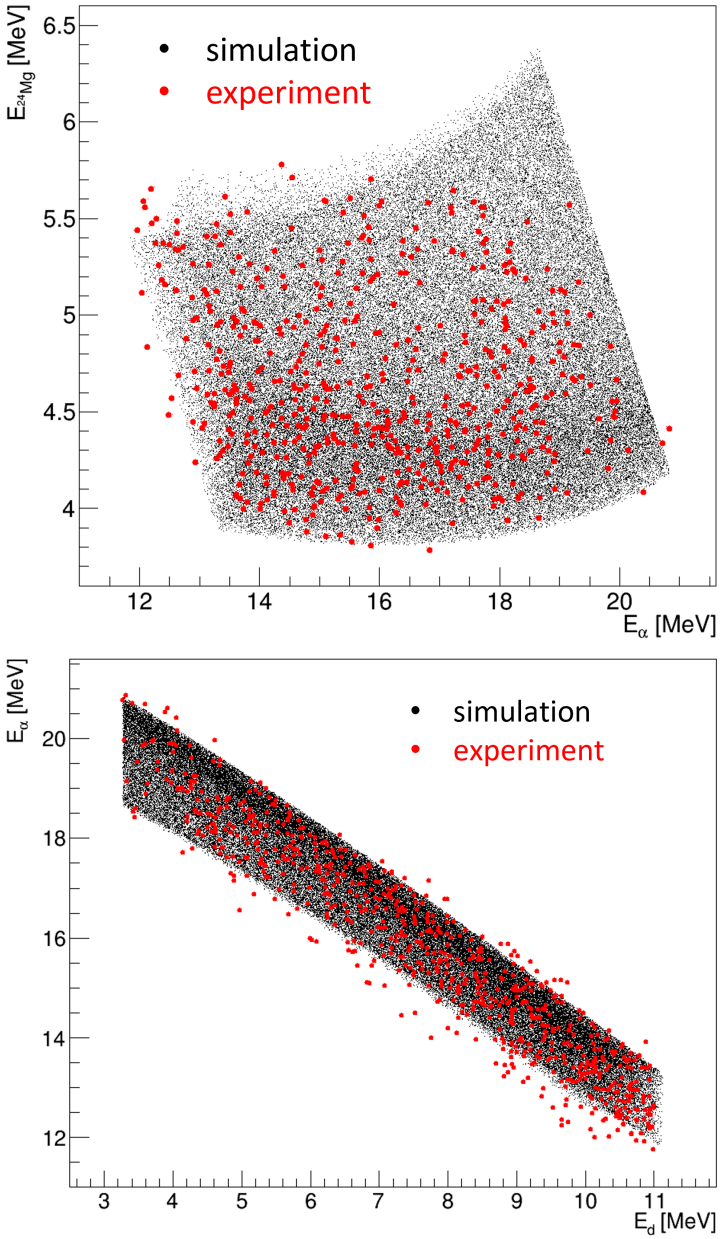

Figure 5.15: Upper panel: experimental (red points) kinematical loci $E_{^{24}Mg}$ versus E_α (). Lower panel: E_α versus E_d plotted against those obtained from the Monte Carlo simulation (black points)

5.6 Selection of QF mechanism

We can now select the QF break-up events of interest by analyzing the momentum distribution of the spectator that we directly measured and by comparing it with the expected value it had inside the TH nucleus. In this case we can calculate the momentum distribution directly from the energy measured by the detectors for deuterons spectator, meanwhile the theoretical distribution is obtained from the Wood-Saxon $^{12}C - d$ bound state potential, considering the standard [13] parameters $r_0 = 1.25$ fm, $a = 0.65$ fm and $V_0 = 54.428$ MeV tuned to obtain the experimental ground state $^{12}C - d$ binding energy inside the ^{14}N TH nucleus. By looking at Fig. 5.16, where the $E_{c.m.}$ is plotted against the momentum of the spectator p_s, it is possible to notice two important facts. First of all, in this case there are no isolated resonances as it instead happened in the previous chapter: this was expected considering what we saw in Fig. 5.1. Therefore in this case we can take most of the energy range covered by the data and evaluate the momentum distribution of the spectator, since the HOES cross-section does not vary significantly in this range. The second fact that must be noted is that in Fig. 5.16 it is possible to see once again an unexpected bulge of events, highlighted by a red circle, that should not be present: we therefore also removed from the analysis the events contained inside this region.

Finally in Fig. 5.17 it is possible to see the experimental momentum distribution of the spectator evaluated for $2.5 < E_{c.m.} < 6MeV$ (blue crosses) and compared with the theoretical distribution (red curve). This analysis shows a good agreement between the experimental data and the theoretical curve, which is therefore a clear sign of the presence of the desired QF break-up events. However if we look closely we can see the presence of a distortion in the distribution slightly above 70 MeV/c: for this reason we decide to continue the analysis only with events for $p_s < 70MeV/c$. Considering what it is shown in Fig. 5.16 this cut should not affect the $E_{c.m}$ energy range we want to study.

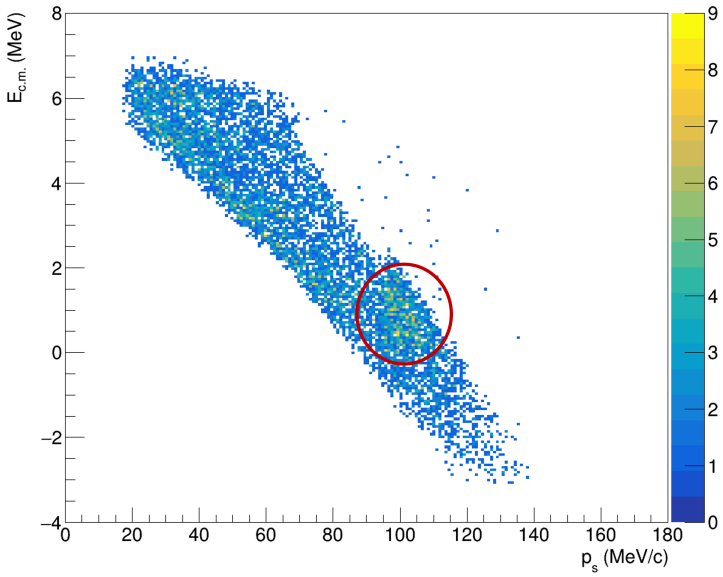

Figure 5.16: Scatter plot of the $E_{c.m.}$ versus the momentum of the spectator p_s .

5.7 Extraction of the two-body cross section

Remembering that under the PWIA assumptions, it is possible to rearrange the formula in Eq. 3.6 as it follows:

$$\left(\frac{d^2\sigma^N_{xA}}{d\Omega dE_{c.m.}}\right)_{HOES} \propto \frac{1}{K.F.}\,\frac{1}{|\Phi(p_s)|^2}\,\frac{d^3\sigma_{TH}}{d\Omega_b d\Omega_B dE_b} \tag{5.2}$$

we can extract the bare nuclei cross-section $\left(d^2\sigma^N_{xA}/d\Omega dE_{c.m.}\right)_{HOES}$ for the 2-body $^{12}C(^{16}O,\alpha)^{24}Mg$ reaction by dividing the triple differential cross section $d^3\sigma_{TH}/d\Omega_b d\Omega_B dE_b$ of the three-body $^{16}O(^{14}N,\alpha^{24}Mg)^2H$ reaction for the product of the kinematical factor and the square of the momentum distribution $K.F.\cdot|\Phi(p_s)|^2$, obtained by the means of the devoted MC simulation. Remembering also that $d^3\sigma_{TH}/d\Omega_b d\Omega_B dE_b$ is proportional to the experimental yield and that we are still working in absolute units, we can finally obtain the result showed in Fig. 5.18.

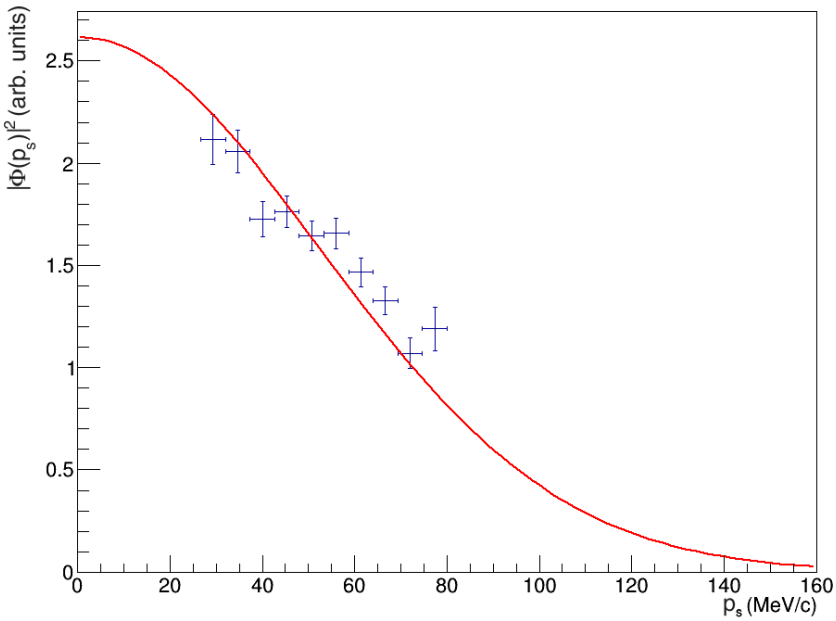

Figure 5.17: Momentum distribution of the deuteron spectator (blue crosses) compared with the theoretical distribution (red curve)

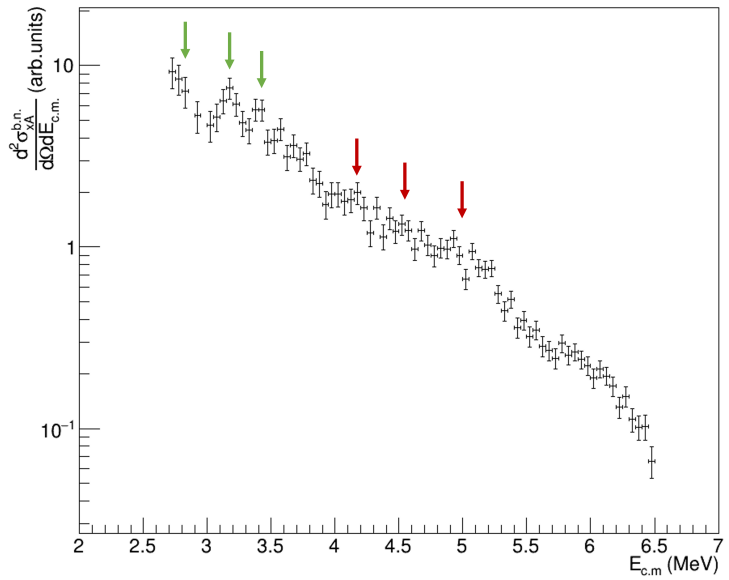

Figure 5.18: HOES cross-section for the 2-body reaction $^{12}C(^{16}O, \alpha)^{24}Mg$ as a function of $E_{c.m.}$. The red arrows indicate the energy position of the resonant structures seen in the S-factor by Fang et al., while green arrows indicate new candidate resonances in the cross section detected in the present work.

While this result certainly requires further analysis and improvements, we can still see some interesting evidence in it. At the same energy values where the three bumps in the S-factor obtained by Fang et al. are present, indicated by red arrows in the figure, we can also see in our data small bumps in the two-body differential cross section which should be clearly better characterized in order to confirm their nature. But probably the most exciting evidence in the figure is the presence of similar bumps in the cross-section at energies below the current lower limit at 4 MeV, down to 3 MeV. If confirmed those bumps could also arise from the same physical phenomena suggested by Fang et al., such as the presence of molecular resonances in the intermediate ^{28}Si system.

5.8 Conclusions and future perspectives

In this chapter of this thesis we have show that the data available in the literature about the $^{12}\mathrm{C} + ^{16}\mathrm{O}$ fusion gives important insights on the total cross-section of the fusion process but do not cover the lower energy part of the Gamow region, forcing to extrapolate below 4 MeV in the center of mass. A new measurement, using the THM, that covers the whole energy region of astrophysical interest is shown and the preliminary results of the analysis procedure are presented. While we still need to analyze the data from the two peripheral telescopes (T1 and T4) for the $^{24}\mathrm{Mg} + \alpha$ channel, we already saw encouraging results regarding the cross-section of the α_0 channel, with the presence of new candidate resonances. The analysis will be further improved, considering the other channels mentioned and, finally, the cross-section and the corresponding reaction rate for both reaction channels will be evaluated. Once the reaction rate will be defined it will be also used to evaluate the impact of the $^{12}\mathrm{C} + ^{16}\mathrm{O}$ fusion process in both the carbon and oxygen burning.

Bibliography

[1] C.E. Rolfs and W.S. Rodney, *Cauldrons in the Cosmos: Nuclear Astrophysics*, *Theoretical Astrophysics* (University of Chicago Press, ADDRESS, 1988).

[2] E. Margaret Burbidge, G. R. Burbidge, William A. Fowler, and F. Hoyle, Reviews of Modern Physics **29**, 547 (1957).

[3] C. Iliadis, *Nuclear Physics of Stars*, *Physics Textbook* (Wiley, ADDRESS, 2015).

[4] D. Habs, P. G. Thirolf, M. Gross, K. Allinger, J. Bin, A. Henig, D. Kiefer, W. Ma, and J. Schreiber, Applied Physics B **103**, 471 (2011).

[5] C. Travaglio, R. Gallino, E. Arnone, J. Cowan, F. Jordan, and C. Sneden, The Astrophysical Journal **601**, 864 (2004).

[6] C. M. Raiteri, M. Busso, R. Gallino, G. Picchio, and L. Pulone, The Astrophysical Journal **367**, 228 (1991).

[7] M. Pignatari, R. Gallino, M. Heil, M. Wiescher, F. Käppeler, F. Herwig, and S. Bisterzo, The Astrophysical Journal **710**, 1557 (2010).

[8] H. Schatz, F. Kaeppeler, P. E. Koehler, M. Wiescher, and H.-P. Trautvetter, The Astrophysical Journal **413**, 750 (1993).

[9] C.A. Bertulani and P. Danielewicz, *Introduction to Nuclear Reactions*, *Graduate Student Series in Physics* (CRC Press, ADDRESS, 2019).

[10] A. Azhari, V. Burjan, F. Carstoiu, C. A. Gagliardi, V. Kroha, A. M. Mukhamedzhanov, F. M. Nunes, X. Tang, L. Trache, and R. E. Tribble, Physical Review C **63**, 055803 (2001).

[11] C. A. Bertulani, Physical Review C **49**, 2688 (1994).

[12] G. Baur, Physics Letters B **178**, 135 (1986).

[13] A. Tumino, C. Spitaleri, M. La Cognata, S. Cherubini, G. L. Guardo, M. Gulino, S. Hayakawa, I. Indelicato, L. Lamia, H. Petrascu, R. G. Pizzone, S. M. R. Puglia, G. G. Rapisarda, S. Romano, M. L. Sergi, R. Spartá, and L. Trache, Nature **557**, 687 (2018).

[14] R E Tribble, C A Bertulani, M La Cognata, A M Mukhamedzhanov, and C Spitaleri, Reports on Progress in Physics **77**, 106901 (2014).

[15] Geoffrey F. Chew and Gian Carlo Wick, Physical Review **85**, 636 (1952).

[16] Ivo Šlaus, R.G. Allas, L.A. Beach, R.O. Bondelid, E.L. Petersen, J.M. Lambert, P.A. Treado, and R.A. Moyle, Nuclear Physics A **286**, 67 (1977).

[17] C. Spitaleri, M. Lattuada, P. Riggi, N. Arena, and D. Vinciguerra, Lettere al Nuovo Cimento (1971-1985) **21**, 345 (1978).

[18] Mahavir Jain, P.G. Roos, H.G. Pugh, and H.D. Holmgren, Nuclear Physics A **153**, 49 (1970).

[19] A. Tumino, C. Spitaleri, M. La Cognata, S. Cherubini, G. L. Guardo, M. Gulino, I. Indelicato, L. Lamia, A. Oliva, R. G. Pizzone, P. Prajapati, G. G. Rapisarda, S. Romano, M. L. Sergi, and R. Spartà, Journal of Physics: Conference Series **1668**, 012045 (2020).

[20] Aurora Tumino, Carlos A. Bertulani, Marco La Cognata, Livio Lamia, Rosario Gianluca Pizzone, Stefano Romano, and Stefan Typel, Annual Review of Nuclear and Particle Science **71**, 345 (2021).

[21] M Gulino, C Spitaleri, S Cherubini, V Crucillà, M La Cognata, L Lamia, R G Pizzone, S Romano, M L Sergi, A Tumino, Li Chengbo, Z Elekes, E Somorjai, V Burjan, V Kroha, and A Mukhamedzhanov, Journal of Physics G: Nuclear and Particle Physics **37**, 125105 (2010).

[22] G. L. Guardo, C. Spitaleri, L. Lamia, M. Gulino, M. La Cognata, X. Tang, R. deBoer, X. Fang, V. Goldberg, J. Mrazek, A. Mukhamedzhanov, M. Notani, R. G. Pizzone, G. G. Rapisarda, M. L. Sergi, and M. Wiescher, Physical Review C **95**, 025807 (2017).

[23] A. M. Lane and R. G. Thomas, Reviews of Modern Physics **30**, 257 (1958).

[24] Erich Vogt, Reviews of Modern Physics **34**, 723 (1962).

[25] F. O. Barker, Australian Journal of Physics **25**, 341 (1972).

[26] Home | JINA-CEE, Joint Institute for Nuclear Astrophysics - Center for the Evolution of the Elements, https://www.jinaweb.org/.

[27] IRENA - Home, https://www.irenaweb.org/.

[28] C. R. Brune, Physical Review C **66**, 044611 (2002).

[29] Daniel Odell, Carl R. Brune, Daniel R. Phillips, Richard James deBoer, and Som Nath Paneru, Frontiers in Physics **10**, (2022).

[30] Joxemai4, English: Graph of a Markov Chain.

[31] Nicholas Metropolis, Arianna W. Rosenbluth, Marshall N. Rosenbluth, Augusta H. Teller, and Edward Teller, The Journal of Chemical Physics **21**, 1087 (1953).

[32] W. K. Hastings, Biometrika **57**, 97 (1970).

[33] Jonathan Goodman and Jonathan Weare, Communications in Applied Mathematics and Computational Science **5**, 65 (2010).

[34] Daniel Foreman-Mackey, David W. Hogg, Dustin Lang, and Jonathan Goodman, Publications of the Astronomical Society of the Pacific **125**, 306 (2013).

[35] The HDF Group - Ensuring Long-Term Access and Usability of HDF Data and Supporting Users of HDF Technologies, https://www.hdfgroup.org/.

[36] A. M. Mukhamedzhanov, L. D. Blokhintsev, B. F. Irgaziev, A. S. Kadyrov, M. La Cognata, C. Spitaleri, and R. E. Tribble, Journal of Physics G: Nuclear and Particle Physics **35**, 014016 (2007).

[37] A. M. Mukhamedzhanov, Physical Review C **84**, 044616 (2011).

[38] M. La Cognata, C. Spitaleri, A. Mukhamedzhanov, A. Banu, S. Cherubini, A. Coc, V. Crucillà, V. Goldberg, M. Gulino, B. Irgaziev, G. G. Kiss, L. Lamia, J. Mrazek, R. G. Pizzone, S. M. R. Puglia, G. G. Rapisarda, S. Romano, M. L. Sergi, G. Tabacaru, L. Trache, R. E. Tribble, W. Trzaska, and A. Tumino, The Astrophysical Journal **708**, 796 (2009).

[39] M. La Cognata, C. Spitaleri, and A. M. Mukhamedzhanov, The Astrophysical Journal **723**, 1512 (2010).

[40] Claude Mahaux and Hans A. Weidenmüller, *Shell-Model Approach to Nuclear Reactions.* (PUBLISHER, ADDRESS, 1969).

[41] M. La Cognata, C. Spitaleri, O. Trippella, G. G. Kiss, G. V. Rogachev, A. M. Mukhamedzhanov, M. Avila, G. L. Guardo, E. Koshchiy, A. Kuchera, L. Lamia, S. M. R. Puglia, S. Romano, D. Santiago, and R. Spartà, The Astrophysical Journal **777**, 143 (2013).

[42] P. E. Koehler and S. M. Graff, Phys. Rev. C **44**, 2788 (1991).

[43] J. Wagemans, C. Wagemans, G. Goeminne, O. Serot, M. Loiselet, and M. Gaelens, Phys. Rev. C **65**, 034614 (2002).

[44] M. Gulino, C. Spitaleri, X. D. Tang, G. L. Guardo, L. Lamia, S. Cherubini, B. Bucher, V. Burjan, M. Couder, P. Davies, R. deBoer, X. Fang, V. Z. Goldberg, Z. Hons, V. Kroha, L. Lamm, M. La Cognata, C. Li, C. Ma, J. Mrazek, A. M. Mukhamedzhanov, M. Notani, S. O'Brien, R. G. Pizzone, G. G. Rapisarda, D. Roberson, M. L. Sergi, W. Tan, I. J. Thompson, and M. Wiescher, Physical Review C **87**, 012801 (2013).

[45] Richard M. Sanders, Phys. Rev. **104**, 1434 (1956).

[46] D. R. Tilley, H. R. Weller, C. M. Cheves, and R. M. Chasteler, Nuclear Physics A **595**, 1 (1995).

[47] C. Spitaleri, A. M. Mukhamedzhanov, L. D. Blokhintsev, M. La Cognata, R. G. Pizzone, and A. Tumino, Physics of Atomic Nuclei **74**, 1725 (2011).

[48] L. Lamia, M. La Cognata, C. Spitaleri, B. Irgaziev, and R. G. Pizzone, Physical Review C **85**, 025805 (2012).

[49] M. Zadro, D. Miljani ć, C. Spitaleri, G. Calvi, M. Lattuada, and F. Riggi, Phys. Rev. C **40**, 181 (1989).

[50] A. Badalà, M. La Cognata, R. Nania, M. Osipenko, S. Piantelli, R. Turrisi, L. Barion, S. Capra, D. Carbone, F. Carnesecchi, E. A. R. Casula, C. Chatterjee, G. F. Ciani, R. Depalo, A. Di Nitto, A. Fantini, A. Goasduff, G. L. Guardo, A. C. Kraan, A. Manna, L. Marsicano, N. S. Martorana, L. Morales-Gallegos, E. Naselli, A. Scordo, S. Valdré, and G. Volpe, La Rivista del Nuovo Cimento **45**, 189 (2022).

[51] O.B. Tarasov and D. Bazin, Nuclear Instruments and Methods in Physics Research Section B: Beam Interactions with Materials and Atoms **266**, 4657 (2008).

[52] W.R. Leo, *Techniques for Nuclear and Particle Physics Experiments: A How-to Approach* (Springer Berlin Heidelberg, ADDRESS, 2012).

[53] E. Costanzo, M. Lattuada, S. Romano, D. Vinciguerra, and M. Zadro, Nuclear Instruments and Methods in Physics Research Section A: Accelerators, Spectrometers, Detectors and Associated Equipment **295**, 373 (1990).

[54] R. G. Pizzone, C. Spitaleri, A. M. Mukhamedzhanov, L. D. Blokhintsev, C. A. Bertulani, B. F. Irgaziev, M. La Cognata, L. Lamia, and S. Romano, Phys. Rev. C **80**, 025807 (2009).

[55] G.G. Ohlsen, Nuclear Instruments and Methods **37**, 240 (1965).

[56] Varley F. Sears, Neutron News **3**, 26 (1992).

[57] M. L. Avila, G. V. Rogachev, V. Z. Goldberg, E. D. Johnson, K. W. Kemper, Yu. M. Tchuvil'sky, and A. S. Volya, Physical Review C **90**, 024327 (2014).

[58] James A. Weinman and Edward A. Silverstein, Physical Review **111**, 277 (1958).

[59] J. K. Bair, J. L. C. Ford, and C. M. Jones, Physical Review **144**, 799 (1966).

[60] Ethan Uberseder and Richard James deBoer, AZURE2 User Manual - Version 1.0, 2015.

[61] James F. Ziegler, M. D. Ziegler, and J. P. Biersack, Nuclear Instruments and Methods in Physics Research Section B: Beam Interactions with Materials and Atoms **268**, 1818 (2010).

[62] C. L. Jiang, K. E. Rehm, B. B. Back, and R. V. F. Janssens, Physical Review C **75**, 015803 (2007).

[63] X. Fang, W. P. Tan, M. Beard, R. J. deBoer, G. Gilardy, H. Jung, Q. Liu, S. Lyons, D. Robertson, K. Setoodehnia, C. Seymour, E. Stech, B. Vande Kolk, M. Wiescher, R. T. deSouza, S. Hudan, V. Singh, X. D. Tang, and E. Uberseder, Physical Review C **96**, 045804 (2017).

[64] L. R. Gasques, E. F. Brown, A. Chieffi, C. L. Jiang, M. Limongi, C. Rolfs, M. Wiescher, and D. G. Yakovlev, Physical Review C **76**, 035802 (2007).

[65] J. R. Patterson, H. Winkler, and C. S. Zaidins, The Astrophysical Journal **157**, 367 (1969).

[66] B. Čujec and C. A. Barnes, Nuclear Physics A **266**, 461 (1976).

[67] P. R. Christensen, Z. E. Switkowskiw, and R. A. Dayras, Nuclear Physics A **280**, 189 (1977).

[68] R. W. Zurmühle, Z. Liu, D. R. Benton, S. Barrow, N. Wimer, Y. Miao, C. Lee, J. T. Murgatroyd, X. Li, V. Z. Goldberg, and M. S. Golovkov, Physical Review C **49**, 2549 (1994).

Acknowledgements

If this thesis even exist, it is thanks to many people which supported me, each in a different and peculiar way, throughout this journey.

First I want to thank my wife for always giving me the clarity and peace of mind I so hardly struggle to find. She is my compass that keeps me going forward instead of losing my way. Without her I would be just energy in potential without control or purpose. I want to also thank my family for supporting my decision to keep following my drive towards science and knowledge, instead of settling for any other job.

There is also another kind of family I want to thank: the AsFiN group. During these years, since my work for the MSc Thesis, they all helped me in my scientific and personal development. My PhD tutors, Prof. Livio Lamia and Dr. Marco La Cognata, have been the guides for this journey, helping me learn most of the things I know now. But most importantly they also endured my energetic but chaotic personality, trying to focus and better aim my efforts. I know it was not always easy to deal with me and for that I would like to express my deepest gratitude to them. I would like to also express my gratitude to Prof. Aurora Tumino for being, even if not formally, by all means another tutor of this PhD Thesis. Especially in these last years she also has been a fundamental part of my scientific and personal development and for that I thank her. At the same way I want to thank Prof. R.J. deBoer for being another important tutor of this

thesis and for helping me understand the fundamental parts of nuclear physics experiments and their data analysis. Without him I would not have been able to solve all the issues I was facing and complete this thesis work. For this I also need to thank to the generous support of the IReNA network which made the meetings with Prof. deBoer possible. I would like to extend my sincere thanks to Prof. Stefano Romano for being a fundamental point of reference during all these years, even after his role as the Tutor of my MSc Thesis. I am also grateful to Dr. Gianluca Pizzone for always been there in the times of need and for always offering me new opportunities and ideas.

I also want to thank Dr. Luca Guardo for helping me during all these years, like a bigger brother, in trying to understand the world of Academia and Research, which unfortunately is still in many ways odd to me. If my tutors were the guide in this journey he was the light that helped me to where I was heading to. I would like to thank also Dr. Dario Lattuada for all the precious insights, both regarding science and most importantly the researcher life, he always offered me. I sincerely hope the "GOL" room, with Luca and Dario, can be preserved for many more years. Special thanks also to Dr. Giuseppe D'Agata for all the important moments of confrontation we had in these years, especially since his comeback to Catania. I am also grateful to Dr. Giuseppe Rapisarda for all the interesting discussions we shared in these years, both scientific and not. I would like also to express my deepest gratitude to Dr. Pierpaolo Figuera for patiently having taught me most of the things I know about detectors and, in general, about the more experimental side of the research activity. Finally I would like to thank all the other members of the AsFiN group which, as said, all helped me in these years in many different ways even if not directly for this work of thesis.

I need to expressing my deepest gratitude also to the coordinator of the PhD in Physics, Prof. S. Albergo, for having done everything and more in his power to help us students in every occasion and guide us all

during these three years. With him as coordinator, our PhD drastically improved reaching the top in this University and for that I thank him.

I could not have undertaken this journey without a few of my PhD colleagues: first Irene and Peppe, with which I shared most of the lectures and exams but most importantly shared all the stress and anxiety in these three long years, starting from the admission exam itself. Then, in the last two year, Claudio joined Irene and me in another important endeavor: being the representatives for the PhD in Physics in the three Department councils where PhD students are represented in. With them I shared uncountable struggles and hopes to improve not only the quality of the PhD in Physics but most importantly the life of all the colleagues, both present and future. I would like to especially thank Irene for the enormous number of times I annoyed here with my thought and discussions and for all the times we confronted and comforted each other. I know for sure that this journey would not have been the same without them and for that I sincerely thank them: they are not only colleagues but dear friends of mine and I hope our friendship will endure even beyond the PhD journey.

I would also like to thanks the members of the "Collegio Docenti" with which I had the pleasure to study and take exams, the referent of my PhD curriculum Prof. Tuvè, the Director of the Department Prof. Grimaldi and the Director of INFN-LNS Dr. Gammino. Lastly I would like to mention all the staff of the DFA and INFN-LNS that helped me in these years in so many different ways, especially Dr. Raffaele Barbato, secretary of the PhD, for always helping me in numerous occasion both as a "normal" student and as a representative.

This journey is now over, even if there are still a lot of thing I wanted to do and learn which were not possible during the pandemic, but I will always dearly keep the memory of these years and all the friends I made along the way.